5-1-2020

Electrolyte interactions with ligand functionalized gold nanoparticles

Sumudu Athukorale

Electrolyte interactions with ligand functionalized gold nanoparticles

By

Sumudu Athukorale

Approved by:

Dongmao Zhang (Major Professor)
David O.Wipf
Todd E. Mlsna
Colleen N. Scott
Joseph P. Emerson (Graduate Coordinator/Committee Member)
Rick Travis (Dean, College of Arts & Sciences)

A Dissertation
Submitted to the Faculty of
Mississippi State University
in Partial Fulfillment of the Requirements
for the Degree of Doctor of Philosophy
in Chemistry
in the Department of Chemistry

Mississippi State, Mississippi

May 2020

Name: Sumudu Athukorale

Date of Degree: May 1, 2020

Institution: Mississippi State University

Major Field: Chemistry

Major Professor: Dongmao Zhang

Title of Study: Electrolyte interactions with ligand functionalized gold nanoparticles

Pages in Study: 104

Candidate for Degree of Doctor of Philosophy

Electrolyte interactions with ligand functionalized gold nanoparticles (AuNPs) have broad implication to a wide range of applications in nanoparticle research field. Among a wide range of electrolytes, halides, nitrates, borohydrides, and sulfides are used to study the AuNP interfacial interactions. Although there are many studies on AuNP interactions with anionic species (halides, nitrates, borohydrides, and sulphides), there is limited information on AuNP interactions with metallic cations. Therefore, studying the nanoparticle interfacial interactions with both anionic and metallic cation species is highly important. The research reported here is focused on deepening the understanding of electrolyte interactions with ligand functionalized AuNPs in aqueous solutions.

The stability of citrate-residues on AuNPs against ligand displacement has been controversial. In the first study, we demonstrated the direct experimental evidence for the simultaneous adsorption of both citrate-residues and solution impurities onto citrate-reduced AuNPs by using AuNPs synthesized with deuterated citrate in combination with the surface-enhanced Raman spectroscopic (SERS) analysis. The citrate-residues can be readily displaced from AuNPs by a wide range of specific and non-specific ligands including organosulfur and electrolytes.

In the second study, we investigated the charge state and the mechanism of silver ion binding onto organothiol functionalized AuNPs. Mechanistic study reveals that silver binding onto AuNPs proceeds predominantly through reactive pathways with proton generations providing the first direct experimental evidence that Ag^+ can disrupt the Au-S binding and enhance the mobility of the organothiols on AuNPs.

Ligand displacement from AuNPs is important in a wide range of applications. Complete and non-destructive removal of ligands from AuNPs is important and challenging due to the strong Au-S binding and the steric hindrance imposed by ligand overlayer on AuNPs. In the final study, we investigated hydrogen sulphide (HS^-), an anionic thiol as an effective ligand to induce complete and non-destructive removal of ligands from aggregated AuNPs.

The new insights and methodologies presented in this dissertation are important for studying the electrolyte interfacial interactions with ligand functionalized AuNPs which have a broad impact on nanoparticle surface chemistry.

DEDICATION

I would like to dedicate this Doctoral dissertation to my loving parents Kusuma Athukorale and Dharmasena Athukorale for their dedication, guidance, unconditional love and tremendous support given to me in this life. I also dedicate this to my brothers and all my teachers for their guidance and enormous support. Finally, I would like to dedicate this to my loving husband, Ayantha Senanayaka and my loving daughter Thevni Senanayaka, for their commitment, support and patience even in times no light could be seen.

ACKNOWLEDGEMENTS

This dissertation would not be possible without the help and support of many wonderful people.

First and foremost, I would like to express my deepest gratitude to my advisor Dr. Dongmao Zhang, for his valuable advice, guidance, encouragement, and support throughout my Ph.D. studies. Also, I eternally grateful his immense support, advice and patience for me during extremely hard times in my life.

I gratefully acknowledge to my committee members Dr. Joseph Emerson, Dr. David O. Wipf, Dr. Todd Mlsna, and Dr. Colleen Scott for their helpful suggestions and discussions. I sincerely thank former and current graduate coordinators, Dr. Stephen C. Foster and Dr. Joseph P. Emerson, for their guidance throughout my graduate career.

I want to thank all our collaborators: Dr. Shengli Zou (University of Central Florida), Dr. Felio Perez (University of Memphis), Dr. Charles U. Pittman, Jr. (Mississippi State University), Dr. Nicholas Fitzkee (Mississippi State University), and Dr. Xin Cui (Mississippi State University). I thank them all for their insightful input and valuable discussions.

My special thanks to Dr. Laura Smith, Mrs. Laura Lewis, and Mrs. Dongping Zhang for their advices, help and support in numerous ways in my graduate career.

I would like to take this opportunity to thank my current and past lab members including, Dr. Fathima Ameer, Dr. Manuel Gadogbe, Dr. Charles Nettles, Dr. Ganganath Perera, Dr. Kumudu

Siriwardana, Dr. Wenkai Zhang, Xue Leng, Joana Xu, Weiyo Peng, Bayan Alharbi and all my friends.

I am greatly indebted to the Department of Chemistry, Mississippi State University for giving me the opportunity to be a graduate assistant here at the MSU.

Finally, my heartfelt acknowledgement goes to my parents, brothers, husband and daughter for their devotion, love, and support which helped me complete this research study successfully.

TABLE OF CONTENTS

LIST OF TABLES

LIST OF FIGURES

LIST OF ABBREVIATIONS

NPs	Nanoparticles
AuNPs	Gold nanoparticles
SAM	Self-assembled monolayer
LSPR	Localized surface plasmon resonance
CE	Chemical enhancement
EM	Electromagnetic enhancement
SERS	Surface enhanced Raman spectroscopy
XPS	X-ray photoelectron spectroscopy
ICP-MS	Inductively coupled plasma-mass spectroscopy
TEM	Transmission electron microscopy
FTIR	Fourier transform infrared spectroscopy
UV-vis	Ultraviolet-visible
2-MBI	2-Mercaptobenzimidazole
ET	Ethanethiol
BuT	Butanethiol
HT	Hexanethiol
DDT	Dodecanethiol
NT	Naphthalenethiol

MBT	Methylebenzenethiol
EDT	Ethanedithiol
BDT	Benzenedithiol
DBDS	Dibutyldisulfide
ME	Mercaptoethanol
TG	Thioguanine
Cit(H)	Undeuterated trisodiumcitrate
Cit(d_4)	Deuterated trisodiumcitrate

CHAPTER I

INTRODUCTION

Gold has been widely used in a wide range of applications with different forms of gold especially due to its inert nature. As an example, evaporated gold films and high purity gold foils have been extensively used in electrochemical applications,[1-3] while gold nanoparticles (AuNPs) have been studied extensively and became a very important class of nanomaterial owing to their unique chemical, optical, and electronic properties and wide range of applications in biosensing, catalysis, biomedicine, electronics, and surface-enhanced Raman spectroscopy (SERS).[4-11] This is because, at the nanoscale regime, metal nanoparticles (NPs) exhibit fascinating physical and chemical properties which are different from their bulk counter-parts. For instance, AuNPs have a color of red or purple while bulk gold has a yellowish color and also, AuNPs are much more catalytically active than the bulk gold.[12]

There are well-established methods reported to synthesize highly monodispersed AuNPs with controlled size and shape. The citrate-reduction method, which was introduced by Turkevich et al in 1951, the common method used to synthesize AuNPs.[13] In this synthesis, $AuCl_4^-$ is reduced by sodium citrate to produce spherical AuNPs in aqueous solution with diameters less than 100 nm. Citrate plays two key roles in this synthesis: as a reducing agent as well as a stabilizing reagent for the AuNPs. As a stabilizing reagent, adsorbed citrate molecules provide a negatively charged surface to AuNPs to enhance the electrostatic repulsions among AuNPs to disperse the AuNPs in aqueous solution.[14] Later in 1973, Frens *et al.* modified the Turkevich method to synthesis AuNPs

with a size range of 15-150 nm by varying the ratio of $AuCl_4^-$ to citrate concentration.[15] Another common method used to synthesize AuNPs is Brust-Schiffrin method.[16] In this method, $AuCl_4^-$ is reduced by sodium borohydride and the AuNPs are stabilized by a thiol capping layer. The size of AuNPs can be controlled by varying the ratio of $AuCl_4^-$ to thiol concentration and only AuNPs with smaller sizes (1-3 nm) can be synthesized by using the Brust-Schiffrin method. Besides synthetically controlling AuNP sizes, shapes, and chemical compositions, another strategy for expanding AuNP functionality and applicability is through post-synthesis of AuNP surface modifications.[17-19] Indeed, AuNP surface chemistry including ligand interfacial interactions of plasmonic AuNPs have evolved as one of the most active research areas due to its importance in essentially every aspect of AuNP applications.

1.1 Ligand interfacial interactions with AuNPs

Surface functionalization is a common strategy to enhance AuNP dispersion stability, target specificity, and biocompatibility.[17-19] There are extensive studies on AuNP interfacial interactions with organosulfur, organic molecules, anionic species and metal ions.[20-23] The spontaneous adsorption of ligands onto AuNPs lead to the formation of self-assembled monolayers (SAM), which is an important phenomenon in expanding the applicability of AuNPs.[24-25] SAM of thiols on AuNPs has extensively been studied owing to the strong covalent nature of Au-S bond[22, 26-27] which is useful in a wide range of applications including bio sensing, spectroscopy, catalysis, and solar-energy harvesting etc.[17, 28-29] The surface functionalization of AuNPs is performed by two main approaches. The first approach is one-step synthesis of ligand functionalized AuNPs. For example, the synthesis of thiol functionalized AuNPs in Brust-Schiffrin method in which Au^{3+} is reduced by $NaBH_4$.[16] The second approach is the functionality through post modification of the colloidal AuNPs with various ligands. In this approach, the incoming ligand should have a high

binding affinity than the ligands that are already bound to the AuNP surface. There is a wide range of molecules including organothiols, proteins, and amines that have been used to modify the AuNPs through either covalent or non-covalent interactions.[30-31] As an example, bound citrate on citrate capped AuNPs can be easily displaced by thiols to modify the surface functionalization on AuNPs.[24, 32]

Even though there are a wide range of ligands used to functionalize the AuNPs to study their interactions, this dissertation focuses on studying electrolyte interactions with organothiol and amine functionalized AuNPs in aqueous solutions.

1.2 Electrolyte interactions with AuNPs

Among wide range of electrolytes, alkali metal halides have been commonly used to study the interfacial interactions with AuNPs. NaCl and KCl are commonly used alkali metal halides to induce NP aggregation, especially for SERS spectral acquisitions.[33] Not only for the SERS acquisitions, halide ions are also considered as shape-directing agents to synthesize gold nanostructures such as nanorods, nanoprisms, nanostars, and nanotriangles. [34-36] In fact, it is a well-known phenomenon that the iodide and bromide ions induce AuNP fusion.[37] We have demonstrated in our previous studies the rapid reduction of SERS intensity of organothiols adsorbed onto AuNPs through both iodide-induced organothiol desorption and AuNP fusion.

In addition to halides, nitrates, borohydrides, and sulfides are also used as electrolytes to study the AuNP interfacial interactions. For example, AuNP-based colorimetric determination of nitrate has reported by Mirkin *et al.*[38] Sodium borohydride is also important in AuNP synthesis[16] and Zhang *et al.* reported the assembly of AuNPs into chainlike structures on a chemically modified glass surface based on $NaBH_4$ treatment.[39]Also our previous work has successfully demonstrated sodium borohydride-induced ligand displacement (organothiols, halides, dyes, and

polymers) from AuNP surfaces[40] and desulfurization of thioamides on AuNPs.[41] Zhang *et al.* reported that sulfide ions can be used as an anti-aggregating agent of AuNPs.[42] While there is extensive work on gold interaction with anionic species - halides[20-21, 43] , nitrates,[38] borohydrides,[39-40] and sulfides[42] in particular - the information on the metallic cation interaction with gold has been relatively limited.[23] Many studies has devoted to develop colorimetric determination of heavy metal ions by using AuNPs functionalized with thiols, DNA, and proteins, owing to the AuNP aggregation induced by these metal ions.[44-48] As an example, Chen *et al.* reported that citrate-reduced AuNPs functionalized with ssDNA selectively bind with Hg^{2+} ions[49] while Huang and co-workers studied the binding of Hg^{2+}, Pb^{2+}, and Ag^{+} onto alkanethiol functionalized AuNPs.[50] Chai *et al.* have shown that Pb^{2+} ions can selectively bind to glutathione functionalized AuNPs via chelating of Pb^{2+} ions with glutathione. Pyrophosphate functionalized AuNPs for Fe^{3+} detection,[51] and iminodiacetic acid functionalized AuNPs for Cu^{2+} detection[52] are among some of the other studies which used functionalized AuNPs in heavy metal detection via colorimetric methods. Also, several recent studies show that Ag^{+} can spontaneously deposit onto AuNPs,[53] and monolayer-protected gold cluster.[54]

Along with electrolytes, organothiols, organic molecules with thiol functional groups (such as thioamides), and amines have used to functionalize AuNPs through covalent bonding or non-covalent interactions. [55] Therefore, it is important to study the electrolyte interfacial interactions with ligand functionalized AuNPs has a broad impact on nanoparticle research.

The next section discusses different analytical techniques used to characterize the surface chemistry of the ligand functionalized AuNPs.

1.3 Analytical techniques for studying AuNP interactions with ligands

Surface analytical techniques are vital for comprehensive understanding of nanoparticle surface chemistry. Therefore, it is important to choose the correct analytical tool to study ligand interactions with AuNPs. However, characterization and quantification of ligand adsorption onto AuNPs is very challenging, mainly due to the extremely low number of ligands adsorbed onto the AuNPs. The analytical technique should be sensitive enough to detect the adsorbed ligands and be selective to the matrix interferences in order to draw meaningful conclusions.

AuNPs exhibit a strong UV-vis extinction spectrum which is not present in the bulk gold. This extinction occurs when the incident light frequency is resonating with the collective oscillations of the conduction band electrons of AuNPs. This phenomenon is called localized surface plasmon resonance (LSPR).[56] Schematic representation of the LSPR of spherical NPs is shown in Figure 1.1. The LSPR position and broadness of NP depends on factors such as size, shape, dielectric environment, and the aggregation state of NPs.[56-58] Therefore, UV-vis spectroscopy is the main spectroscopic technique used to demonstrate the plasmonic properties of metal nanoparticles. For example, characterization of electrolyte-induced AuNP aggregation using UV-vis spectroscopy.[59] There is a significant red shift and broadening in the LSPR peak of the AuNPs in the UV-vis spectrum to indicate electrolyte-induced AuNP aggregation.[59] UV-vis spectra demonstrate the sample total photon extinction, which is the sum of the photon absorption extinction and scattering extinction. Recently we have demonstrated the de-convolution of AuNP UV-vis extinction cross-section spectra into their absorption and scattering component spectra, and quantified the AuNP light scattering depolarization spectrum as well as the scattering to extinction ratio spectrum using combining UV-vis extinction spectra and polarized resonance synchronous spectroscopy (PRS_2) spectra.[60-61]

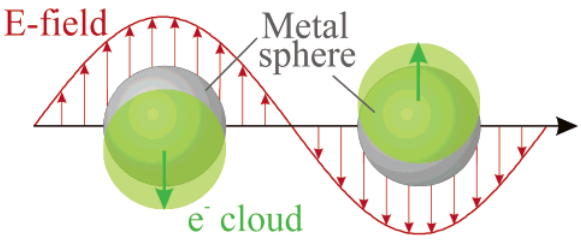

Figure 1.1 Schematic representation of plasmon oscillation for spherical NPs.

Note: Reproduced with permission from ref 46. Copyright 2003 J. Phys. Chem. B.

The morphological changes induced by the ligands, electrolytes on AuNPs are mainly characterized by using scanning electron microscopy (SEM) and transmission electron microscopy (TEM).[37, 62-63] Dynamic light scattering (DLS)[64] and zeta-potential[65] measurements can be used to determine hydrodynamic diameter and surface charge, respectively. The surface charge of the AuNPs after interacting with electrolytes is a key parameter when studying AuNP stability in a solution.[65] X-ray photoelectron spectroscopy (XPS) is also an important technique to characterize the elemental composition and the charge state of electrolytes on AuNPs.[34] Organothiol structure and conformation on AuNPs have been studied using a wide range of analytical methods such as Fourier transform infrared spectroscopy (FTIR),[66-67] nuclear magnetic resonance spectroscopy (NMR),[68-69] and surface enhanced Raman spectroscopy (SERS).[70-71]

The main analytical techniques used in this dissertation are SERS and XPS. The following section provides information about the fundamental principles of the SERS and XPS.

1.4 Surface enhanced Raman spectroscopy (SERS)

Due to the low inelastic scattering efficiency of photons, the direct sensitive detection of analytes in Raman spectroscopy is difficult. In contrast, when the same analyte is attached to a rough metal surface or to nanometre sized metallic colloidal particles, produces a strong Raman signal with signal enhancements by many orders of magnitudes (~ 10^8) and this spectroscopic method is called surface enhanced Raman spectroscopy (SERS). SERS has become popular and highly useful analytical tool to study ligand adsorption onto NPs since its discovery in the 1970s. It is mainly due to the ability to acquire SERS spectra in aqueous environment, fingerprint spectra of the molecules, and overcome the low detection sensitivity issues in Raman spectroscopy. [72-74]

It has been proposed that there are two multiplicative contributions to the total SERS enhancement. They are electromagnetic enhancement (EM) and chemical enhancement (CE). CE is considered as the short-range effect and mainly occurs due to charge transfer interactions between the molecule and the metal nanoparticle. The contribution of CE to the SERS signal is smaller than the EM and typical magnitude is ~10^2.[2,75] In contrast, EM is considered as a long-range effect and originates due to the resonance effect of incident electromagnetic field from the localization of light at the surface with the surface plasmons of metal NPs. When compared to CE, EM contributes more than a 10^4 x enhancement of the Raman signal intensity.[75] The relationship between the applied electric field (E_{laser}) and the electromagnetic field induced ($E_{induced}$) on the surface of a spherical NP is given by Eq.1.1.[76]

$$E_{induced} = \left[\frac{\varepsilon_1(\omega) - \varepsilon_2}{\varepsilon_1(\omega) + 2\varepsilon_2}\right] E_{laser} \qquad (1.1)$$

Where;

ε_1 (ω) - frequency dependent dielectric function of the metal

ε_2 - relative permittivity of ambient phase

It is well-established that the SERS signal can be further enhanced by reducing the distance (gap) between the NPs. As the gap between NPs is reduced, the EM enhancement is integrated over the entire NP surface and the molecules located at these gaps experience an enhanced electric field leading to an enhanced signal. The reduction of the gap between NPs are commonly achieved by NP aggregation which occurs by either spontaneous self-assembly of ligands on NPs or by the addition of aggregating electrolytes such as KCl and KNO_3.[76]

1.5 X-ray photoelectron spectroscopy (XPS)

XPS is considered as one an indispensable technique use to assess the chemical bonding state of elements at the surfaces and interfaces since its development in 1980s.[77-78] In XPS, a beam of X-ray having a constant energy (*hv*) is irradiating onto the surface of specimen in a vacuum (Figure 1.2). The binding energy of ejected photoelectrons are determined by measuring the kinetic energy as shown in the Eq.1.2.

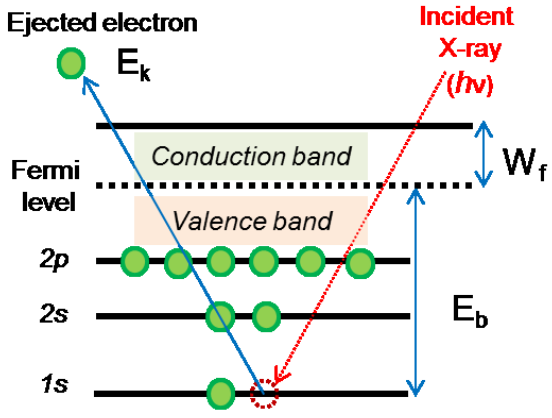

Figure 1.2 Schematic representation of the photoemission process involved in XPS

$$h\nu = E_k + E_b + W_f \quad (1.2)$$

Where;

hν - energy of the X-ray photons being used

E_k - kinetic energy of photoelectron

E_b - binding energy of electron to nucleus relative to the Fermi level

W_f - work function of specimen

XPS detects the electrons which are truly escaped from the sample into the vacuum, and then to the detector. In order for the electron to escape from the sample into the vacuum, a photoelectron must travel through the sample. The emitted electrons can undergo inelastic collisions, recombination, recapture, or trapping in various excited states within the material and these processes reduce the number of photoelectrons that escape from the sample to the vacuum. Therefore, signals detected from the surface of a sample are much stronger than the signals detected below the sample surface. Most of the commercial instruments use the incident X-ray of $h\nu < 1.5$ keV, which would be resulting the E_K is not larger than 1.5 keV, leading to a very shallow escape depth (λ) of photoelectrons. In this energy range approximately the λ is range from 0.3-4 nm.[79]

1.6 Dissertation objectives

Electrolyte interactions with ligand functionalized AuNPs have broad implications for a wide range of applications in nanoparticle research field. Our research group is interested in studying the nanoparticle interfacial interactions of proteins, electrolytes, and organic molecules with noble metal nanoparticles and their SERS applications. As part of an extension to the current fundamental understanding of the ligand interfacial interactions and SERS applications, reported herein is our recent study of electrolyte interactions with ligand functionalized AuNPs in water. The key objectives of this dissertation are (1) to offer direct experimental evidence to demonstrate the facile displacement of citrate-residues on AuNP surface using wide range of specific and non-specific ligands including organosulfur and electrolytes. (2) elucidation of the charge state and the mechanism of silver ion binding onto organothiol functionalized AuNPs, and (3) investigation of the NaHS as an effective ligand for complete nondestructive ligand displacement from AuNPs.

This dissertation is composed of four related chapters. Chapter I includes an overview of the current state-of-knowledge of the subject related to the dissertation. Chapter II demonstrates the presence of both citrate-residues and solvent-born impurities on citrate-reduced AuNPs, (not citrate-residues alone, as assumed in literature) and their displacement using wide range of specific and non-specific ligands including organosulfur and electrolytes mainly using SERS and XPS measurements. The main focus of Chapter III is the spontaneous and reactive adsorption of Ag^+ onto gold substrates that include both as-syntheized and butanethiol-functionalized citrate- and $NaBH_4$-reduced gold nanoparticles (AuNPs), commercial high-purity gold foil, and gold film sputter-coated onto silicon, which provides the first direct evidence that Ag^+ can disrupt the Au-S binding and enhance the mobility of the organothiols on AuNPs. The final chapter, chapter IV, provides experimental evidences of using NaHS as an effective ligand for complete nondestructive

displacement of wide variety of ligands including aliphatic and aromatic thiols (ethanethiol, methylebenzenethiol), organothiol (benzene dithiol), thioamides (mercaptobenzenethiol and thioguanine), and nonspecific ligand adenine from AuNPs, which open the doors for developing AuNP-based capture-and-release biomolecule enrichment methods.

CHAPTER II

FACILE DISPLACEMENT OF CITRATE RESIDUES FROM GOLD NANOPARTICLE SURFACES

(Published in *J. Colloid Interface Sci.* **2018**, *511*, 335-343)

2.1 Abstract

The stability of citrate-residues on gold nanoparticles (AuNPs) against ligand displacement has been controversial. Using AuNPs synthesized with deuterated citrate in combination with in-situ surface-enhanced Raman spectroscopic (SERS) analysis, we report that both citrate residues and solution impurities can be simultaneously adsorbed onto citrate-reduced AuNPs in solution. The citrate-residues can be readily displaced from AuNPs by organosulfur such as organothiols (RS-H), organodisuflide (R-S-S-R), and non-specific ligands including halides and adenine. Control experiments conducted on high-purity gold films sputter-coated onto silicon substrates indicate that air-borne and solvent-borne impurities rapidly contaminate the gold surfaces. Head-to-head comparison of ligand-functionalized AuNPs by in-situ SERS measurements verses those from the ex-situ X-ray photoelectron spectroscopic (XPS) measurements reveal that the impurity deposition can compromise the reliability of ex-situ XPS identification of surface adsorbates on AuNPs in solution. These insights are of general significance to nanoscience research given the broad interest in nanoparticle surface chemistry and popularity of XPS for nanomaterial characterizations.

2.2 Introduction

Surface chemistry is an essential part of nanoscience research because the nanoparticle (NP) stability, physiochemical properties, and biological functionality depend critically on the ligand structure and composition on NP surfaces. [55, 80-81] Reliable characterization of molecular adsorbates on NPs is however, a challenging task. Sensitive methods must be used to detect the minuscule amount of chemicals on NP surfaces with, ideally, no possibility to introduce even trace-amounts of chemical contamination. This is why earlier works on molecular self-assembly on gold were performed mostly with carefully cleaned planar gold substrates, highly purified reagents, and under tightly controlled experimental conditions such as high vacuum [82-84].

Surface contamination on NPs can be of special concern compared to that for planar gold. First, NPs are rich in defects and vertices [85-87]. The surface atoms at those locations, due to their low coordination numbers, are much more reactive than locations on a bulk planar surface. Recent research demonstrated that AuNP surface curvatures have significant impacts on the ligand binding affinity and kinetics on the AuNP surfaces[88]. Therefore, ligand adsorption is generally more prominent on NP surfaces than that on the bulk material. Second, NPs are usually prepared in solutions [89-91]. Solvent impurities, excess reactants, and reaction by-products can be adsorbed onto NPs during NP synthesis and characterization.

One of the most popular surface characterization techniques is X-ray photoelectron spectroscopy (XPS) [92-94]. Shumaker-Parry *et al.* has recently published two highly-cited studies on surface adsorbates on citrate-reduced gold nanoparticles (AuNPs) [95-96]. On the basis of their XPS analysis, ATR-FTIR measurements, and computational modeling, the authors proposed the structure of the citrate-residues on AuNP surfaces [95], and concluded that citrate displacement is highly resistant to organothiols [96]. One apparent limitation in those studies that was not considered

is the possibility that impurity adsorption and deposition from solvent might have occurred during AuNP synthesis and characterization. This is especially of a concern given that their XPS and ATR-FTIR measurements were all obtained with the samples dried from solvents.

The current study has two key objectives. The first is to re-examine the fate of citrate-residues on AuNP surfaces, and the second is to critically evaluate the reliability of XPS for determination of AuNP surface adsorbates. We choose citrate-reduced AuNPs as the model NPs for the following reasons. First, AuNPs are probably the most-studied of all nanomaterials and they continue drawing intense research interest for their applications in biosensing, catalysis, spectroscopy, and solar-energy harvesting [17, 28]. Many of these applications depend critically on AuNP surface chemistry. As an example, only the molecules directly adsorbed or within extremely close (a few nanometer) vincity to the AuNP surface can experience significant signal enhancement provided by the AuNP surface plasmon in applications where AuNPs are used as surface enhanced Raman spectroscopic (SERS) substrates. Understanding of ligand structure and composition on AuNPs is therefore important for studying the selectivity of the SERS method and reliable spectral interpretations. Second, there are significant controversies on the citrate structure on AuNPs and their fates upon ligand displacement [95-108]. As examples, Parry *et al.* have proposed that citrate residues are highly resistant to displace upon organothiol binding onto AuNPs [96]. He and co-workers shown that the presence of both citrate and dodecanethiol (DDT) on AuNPs at oil/water interface using SERS measurements after addition of DDT onto AuNPs [99]. We also speculated that citrate residues may remain on the organothiol-functionalized AuNPs as one of the posssible receptors of proton produced when organothiol binds to AuNP surfaces [109]. In those studies, however, the possibility of the adsorption of solvent impurities during AuNP preparation, ligand binding, and characterization processes has not been considered.

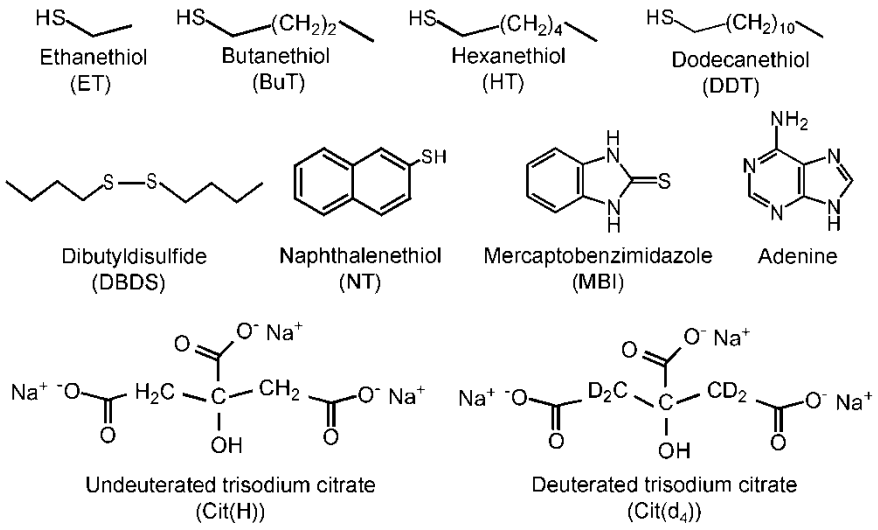

Figure 2.1 Structure and abbreviation of the used model ligands.

On the other hand, there are many other researchers believe that citrate can be displaced easily with organothiols [97, 100, 105-106, 108]. Third and most important, is that AuNPs are among a handful of NPs that have SERS activities [110-114]. One can readily obtain SERS spectra for molecular adsorbates on AuNPs in solutions. This provides a unique opportunity for us to conduct a head-to-head comparison of results from the *in-situ* SERS measurements conducted in solution with *ex-situ* XPS measurements conducted with dried samples. Such a comparison is impossible with NPs that are not SERS active, but is value for probing the reliability of *ex-situ* XPS for general NP surface characterization.

We now report that the surfaces of citrate-reduced AuNPs in solution contain both citrate residues and water-impurity adsorbates. The origin of these surface adsorbates was probed with *in-situ* SERS measurements conducted on AuNPs synthesized with the perdeuterated citrate, containing only C-D bonds but no C-H bonds (Figure 2.1). The stability of the citrate and solvent-impurity adsorbates against ligand displacement was studied by exposing the AuNPs to a series of

organosulfur ligands and adenine (Fig. 1) and halides (Cl^-, Br^-, and I^-) that can only bind nonspecifically to AuNPs. For the sake of convenience, we refer hereafter to the AuNPs synthesized with undeuterated- and deuterated-citrate as Cit(H)- and Cit(d_4)-AuNPs, respectively. The deuterium atoms in the deuterated citrate were exclusively connected to sp^3-hybridized carbon through stable C-D bonds, but not to the oxygen atoms in the carboxyl groups. This ensured no hydrogen/deuterium exchange occurred on AuNPs during their synthesis with the deuterated citrate.

One must be careful in the interpretation of the experimental data obtained with ligand displacement on AuNPs. Complete displacement of the initial ligand is a reliable indicator that the incoming ligand has higher binding affinity to AuNPs than the initial ligand. The concurrent adsorption of the initial and incoming ligand doesn't, however, imply that the two ligands have similar binding affinity. We have recently demonstrated that the multicomponent ligand adsorption depends not only on the relative AuNP binding affinity of competing ligands, but also their sequence of the ligand mixing with AuNPs [115]. As an example, there is no detectable adenine adsorption onto AuNPs if glutathione is first mixed with either as-synthesized or pegylated AuNPs before the adenine addition, but substantial adenine retain on the AuNP surface if adenine is mixed first with AuNPs [115]. The conformation of the initial ligands on AuNPs also has significant effect on the adsorption of the incoming ligand. While the small molecule such as glutathione completely passivates AuNPs preventing further adenine adsorption, substantial adenine can be coadsorbed with thiolated poly(ethylene glycol) (PEG) onto AuNP surface. This is in spite of the fact that adenine likely has significantly lower binding affinity to the AuNPs than that the terminal thiol group in the thiolated PEG [116]. Earlier research has shown that thiolated PEG adopts mushroom-like conformation on the AuNPs and it passivates only a small fraction of AuNP surface against

the co-adsorption of any molecules that can penetrate through the PEG mushroom cap [116]. The fact that the peyglation only passivate a small fraction of the gold surface may also explain the experimental observation by Hore *et al.* that substantial cetyltrimethylammonium bromide (CTAB) remain adsorbed in the pegylated gold nanorods (AuNRs) prepared using CTAB as the stabilizer [117]. In other words, the presence of CTAB on the pegylated AuNRs doesn't necessarily imply that CTAB have comparable binding affinity to AuNP with the terminal thiol group in thiolated PEG.

2.3 Experimental section

2.3.1 Materials and equipment

All chemicals were purchased from Sigma-Aldrich and used as received. Perdeuterated trisodium citrate was purchased from CDN Isotopes Inc. and used as received. The purities of ET, BuT, HT, DDT, NT, DBDS, MBI, adenine, KCl, KBr, KI, Cit(H), Cit(d_4), $NaBH_4$, and $HAuCl_4.3H_2O$ are 97.0, 99.0, 97.0, 99.0, 98.0, 97.0, 98.0, 98.0, 97.0, 98.0, 98.0, 99.0, 98.0, 98.0, and 99.9%, respectively. A LabRam HR800 confocal Raman microscope was used for Raman and SERS acquisitions with 633 nm laser excitation. PC 2000 Oxygen-Argon Plasma Cleaner (South Bay Technology) was used to clean the gold films by oxygen and argon plasmas. An Olis HP 8452 diode array spectrophotometer was used to acquire UV-vis measurements. Nanopure water (18 MΩ-cm) was prepared with a Thermo Scientific Barnstead Nanopure water purification system. Double-distilled Nanopure water was prepared in-house with carefully cleaned glassware including the solvent container. The glassware was first incubated in freshly prepared aqua regia for 1 h and washed sequentially with regular Nanopure water and double-distilled Nanopure water.

2.3.2 Synthesis of citrate-reduced AuNPs

Citrate-reduced AuNPs were synthesized according to a literature procedure [89]. In brief, 0.415 g of $HAuCl_4.3H_2O$ was dissolved in 1000 mL of either as-acquired or double-distilled Nanopure water. These solutions were brought to boil, and then 100 mL of 1% trisodium Cit(H) or trisodium Cit(d_4) was added to the boiling solutions. Finally, the reaction solutions were further boiled for ~20 min while stirring. The average diameters of the as-synthesized Cit(H)- and Cit(d_4)-AuNPs were both 13 nm, respectively, which was estimated on the basis of their UV-vis spectra (Figure 2.2).

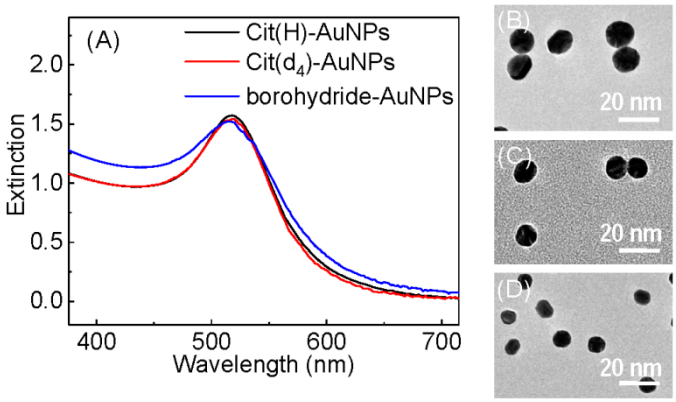

Figure 2.2 (A) UV-vis spectra of two-times diluted as-synthesized (black) Cit(H)- and (red) Cit(d4)-AuNPs, and (blue) undiluted borohydride-AuNPs. TEM images of (B) as-synthesized Cit(H)-AuNPs, (C) as-synthesized Cit(d4)-AuNPs, and (D) as-synthesized borohydride-AuNPs.

Note: The localized surface plasmon resonance peaks for Cit(H)-, Cit(d4)-, and borohydride-AuNPs are at 518, 518, and 516 nm, respectively. The average diameters for Cit(H)-, Cit(d4)-, and borohydride-reduced AuNPs are ~13, ~13, and ~10 nm, respectively. [118-119]

2.3.3 Synthesis of borohydride-reduced AuNPs

$NaBH_4$-reduced AuNPs were synthesized by a modification of a previous report [120]. In brief, 30 mL of 0.1 M $NaBH_4$ was added to 1000 mL of 0.25 mM $HAuCl_4.3H_2O$, and the mixture was stirred for 3 h. The average diameter of the as-synthesized borohydride-AuNPs was ~10 nm, which was estimated on the basis of the UV-vis spectrum (Figure 2.2).

2.3.4 Sputter-coating preparation of gold films

As-received 0.5 cm × 0.5 cm silicon wafers were sputter-coated with gold under vacuum with an Electron Microscopy Sciences 150T ES sputter coater. The purity of the gold target is 99.99% and the thickness of the gold coating was ~100 nm.

2.3.5 Cleaning gold films with argon and oxygen plasmas and high energy X-ray.

Four freshly prepared gold films on silicon was exposed to ambient air for 2 days before studying the effect of argon and oxygen plasma and X-ray cleaning. One gold film was used as a control for the XPS measurement. Two gold films were used for evaluating the effectiveness of both argon and oxygen plasma cleaning, respectively. The operating power, pressure, dc bias voltage, and the time for plasma cleaning were 10 W, 150 mTorr, -25 V, and 30 min, respectively. The fourth gold film was exposed to 1000 eV high energy X-rays for 15 min for *in-situ* X-ray cleaning inside the XPS chamber under vacuum before XPS spectral acquisition. X-ray-cleaned gold film was then sequentially exposed to ambient air for 1 h and immersion in water for 10 min for use in studying the air- and solvent-borne impurity adsorption onto the gold film.

2.3.6 Ligand displacement

As-synthesized Cit(d_4)-AuNPs (50 mL) were mixed with an equal volume of ligands. The concentrations of organosulfur, adenine, and KX are 100 µM, 50 µM, and 100 mM, respectively. The resulting mixtures were vortex mixed briefly and left to sit overnight. All ligand adsorption induced spontaneous AuNP aggregation and complete AuNP precipitation. This is evident from the photograph and UV-vis spectrum obtained with an example AuNP sample before and after the ligand displacement (Figure 2.3). The SERS acquisitions were performed *in-situ* with the AuNP precipitates immersed in the ligand binding solutions. The possibility of normal Raman contributions from the excess ligands in the solutions was excluded based on the fact that there was no detectable ligand Raman signal observed in the supernatant of the ligand binding solutions. The precipitated AuNPs were washed thoroughly with the specified solvent prior to the XPS analysis.

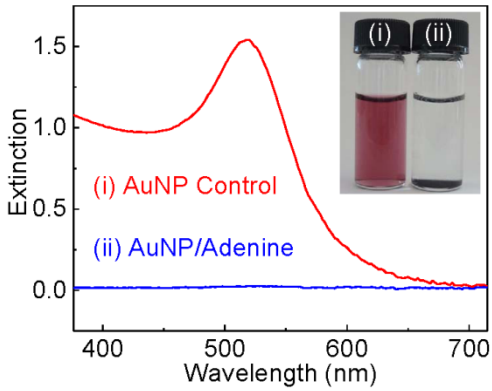

Figure 2.3 UV-vis spectra of two-times diluted as-synthesized Cit(d_4)-AuNPs (red) before and (blue) after adding Adenine. Inset is the optical image of AuNP (i) before and (ii) after the addition of Adenine.

Note: The nominal concentration of Adenine is 50 µM.

2.3.7 Raman and SERS acquisitions

Normal Raman spectra of undeuterated and deuterated citrates (Cit(H) and Cit(d_4)) were acquired with the as-received citrates. The laser power impinged on the objective in the Raman measurement was 13 mW. The SERS spectra of both the as-synthesized AuNPs and the ligand-treated AuNPs were obtained with aggregated AuNPs in solutions. While the AuNP aggregation occurred spontaneously in the organothiol-, disulfide-, adenine- and halide-treated AuNPs, the aggregation of the as-synthesized AuNPs was triggered by $NaNO_3$ addition or by water-washing itself. All the SERS spectra were acquired with a laser power before the microscope objective of 1.3 mW. The acquisition times for normal Raman and SERS spectra were varied between 20-200 s to ensure the SERS spectra have adequate signal-to-noise ratios for ligand identification.

2.3.8 XPS analysis

Unless specified otherwise, all AuNP-containing samples were extensively washed with Nanopure and double-distilled Nanopure water prior to their XPS analysis. Care was taken to minimize the solvent transferred together with the aggregated AuNPs to the silicon substrate for the XPS measurements.

A Thermo Scientific K-Alpha XPS system equipped with a monochromatic X-ray source at 1486.6 eV corresponding to the Al Kα line was used in the XPS acquisitions. The spot size was 400 μm^2 and the takeoff angle of the collected photoelectrons was 90˚ relative to the sample surface. The survey spectra and high-resolution core level spectra were acquired with pass energies of 200 eV and 50 eV, respectively. The average number of scans obtained for each sample was 20 with a step size of 0.1 eV. A Constant Analyzer Energy mode was used for all the XPS measurements and "Avantage v5.932" software was used in XPS data analysis.

2.4 Results and discussion

2.4.1 SERS and XPS analysis of surface adsorbates on AuNPs

Concurrent citrate-residue and water-impurity adsorption occurs on the citrate-reduced AuNPs. This was concluded from the SERS spectra acquired with the as-synthesized Cit(d_4)-AuNPs (2.4A). The normal Raman spectrum of the deuterated sodium citrate shows only the C-D stretching feature at 2100 cm^{-1} with no C-H stretching peak ((b) in Figure. 2.4A). However, there are both C-D and C-H stretching features in the SERS spectrum obtained with the as-synthesized Cit(d_4)-AuNPs ((d) in Figure 2.4A). The presence of a C-D stretching feature in the ~2100 cm^{-1} region confirms the citrate adsorption on the AuNPs, while the presence of the C-H stretching feature in the ~2800 cm^{-1} region indicates the impurity adsorption. This is because neither AuNP synthesis reactants, deuterated citrate, $HAuCl_4$, nor solvent water contains C-H bonds.

The possibility of hydrogen/deuterium exchange between deuterated citrates with chemicals in the Cit(d_4)-AuNP synthesis solution was rigorously excluded by a series of control experiments (Figure 2.5). Raman spectra obtained with excess deuterated citrate found in the drop-dried centrifugation supernatant of Cit(d_4)-AuNPs contains exclusive C-D stretching features, but no C-H stretching features. Furthermore, the solution Raman spectra obtained with deuterated citrate dissolved in H_2O contains only C-D, but not C-H stretching features. This is in spite of the fact this solution had been stored under ambient conditions for more than 6 months. These results indicate there is no significant hydrogen exchange between the deuterium in the deuterated citrate and hydrogen in water, both with and without the presence of AuNPs.

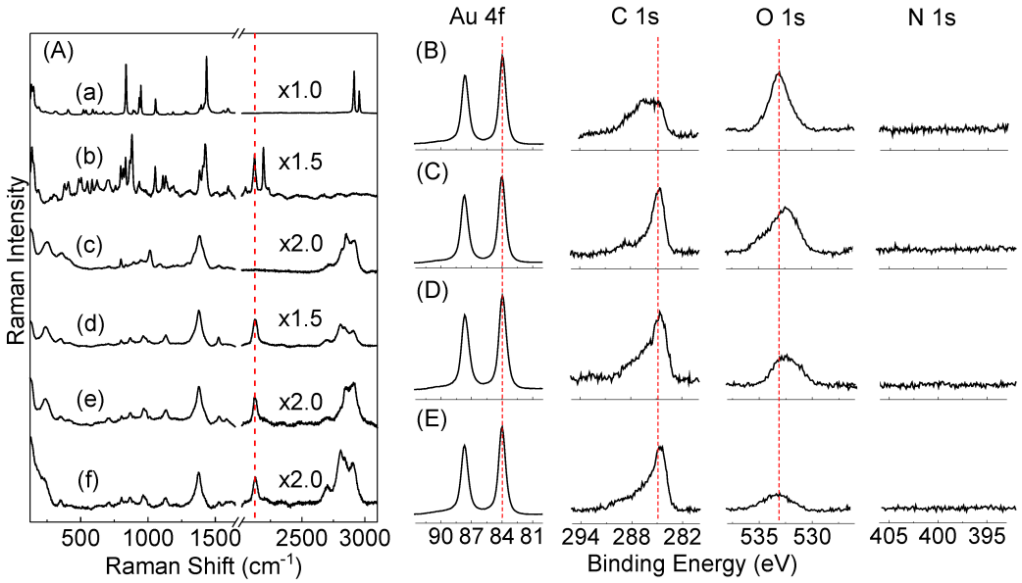

Figure 2.4 (A) Comparison of normal Raman and SERS spectra of as-synthesized Cit(H)- and Cit(d_4)-AuNPs. Normal Raman spectra of neat (a) undeuterated, and (b) deuterated sodium citrate. SERS spectra of (c) as-synthesized Cit(H)-AuNPs in Nanopure water without double distillation, (d) as-synthesized Cit(d_4)-AuNPs in Nanopure water without double distillation, (e) as-synthesized Cit(d_4)-AuNPs in double-distilled Nanopure water, and (f) solvent-dried Cit(d_4)-AuNPs after washing with 99.5% high-purity ethanol. XPS spectra of (B) Cit(d_4)-AuNPs synthesized in Nanopure water without double distillation, (C) Cit(d_4)-AuNPs synthesized in double-distilled Nanopure water, (D) borohydride-reduced AuNPs synthesized in Nanopure water without double distillation, and (E) borohydride-reduced AuNPs synthesized in double-distilled Nanopure water.

Note: The multiplier shown in each Raman and SERS spectrum is the scaling factor for the spectral features in the ~2050-3100 cm^{-1} region in comparison to its spectral features below ~1600 cm^{-1}. The XPS peaks for C1s, O1s, and N1s in all spectra are normalized so that the Au4f intensities are identical for the compared samples.

This impurity adsorption hypothesis is also supported by other evidence. For example, the C-H peak in the Cit(d_4)-AuNP synthesized with Nanopure water (18.2 MΩ-cm) with ((e) in Figure. 2.4A) and without ((d) in Figure. 2.4A) further double distillation is markedly different. The most intense peak in the C-H stretching region is at 2806 cm^{-1} in the Cit(d_4)-AuNPs prepared with Nanopure water, but it is at 2909 cm^{-1} for the ones prepared with double-distilled Nanopure water.

This is likely due to double-distillation changing the solvent impurity compositions. Further strong evidence of impurity adsorption is that the XPS spectra obtained with the AuNPs synthesized with sodium borohydride all contain a relatively intense carbon feature (Figure 2.4D and 2.4E). The possible carbon source in the borohydride-reduced AuNPs is the impurity adsorbates. This is because none of the reactants used to synthesize borohydride-reduced AuNPs contain carbon.

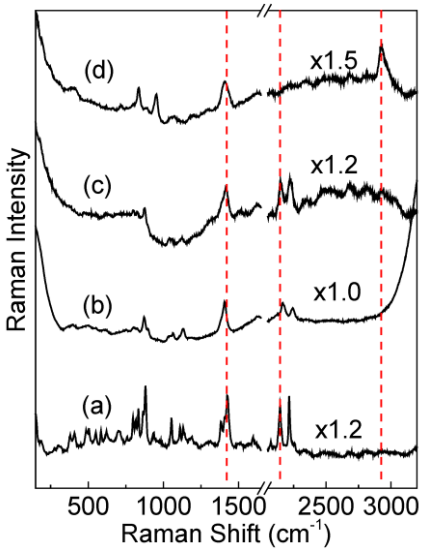

Figure 2.5 Normal Raman spectra of (a) neat deuterated citrate and (b) deuterated citrate in regular water for more than 6 months. The spectra from (c) and (d) are the DCDR spectra obtained for the supernatants of (c) Cit(d_4)-AuNPs synthesized in regular Nanopure water, and (d) Cit(H)-AuNPs synthesized in D_2O.

Note: The multiplier shown with each spectrum in the plot is the scaling factor for the spectral feature in the ~2050-3100 cm^{-1} region in comparison to its spectral features below ~1600 cm^{-1}.

Comparison of the C-H and C-D stretching features in the SERS spectra obtained with the Cit(d_4)-AuNP is revealing (spectra (d) to (f) in Figure. 2.4A). The full width at the half the peak's maximum (FWHM) in the C-H stretching region is 145.4 ± 12.3 cm^{-1} in the SERS spectra obtained with the as-synthesized Cit(d_4)-AuNPs. This is ~6 times larger than the C-D stretching peak width

(26.2 ± 4.1 cm^{-1}) in the same spectrum. This observation has two critical implications. First, the C-H stretching SERS features must have originated from solvent impurities, and cannot be due to the possible hydrogen/deuterium exchanged deuterated citrate. Otherwise, the C-D and C-H stretching peak widths would have to be more similar. Second, the impurity adsorbates are most likely a complex mixture of multiple molecular species. Single component small molecules including citrate and organothiols used in this work all have significantly narrower C-H stretching peak widths.

The impurities can originate from many different sources. The first is that the amount of dissolved organic carbon in water can be as much as ~0.05 ppm in 18 MΩ-cm Nanopure water according to ASTM standards. This corresponds a concentration of ~4 μM in terms of carbon. The second source is the reactants and reaction vessels used in the AuNP preparation. The labeled purity of citrate we used is 99%. If we assume the impurity content is 0.5% and 50% of these impurities are organic species, the citrate would introduce an additional of 2.5 ppm organic species into the reaction solution. This is because the citrate concentration used in the AuNP synthesis is 0.1%. Presumably, $HAuCl_4$ can contain similar level of organic impurity, further increasing impurities in the synthesis solution. The third source is the air-borne species brought into the AuNP solutions either during the solvent and reactant solution preparation process and/or during the AuNP synthesis.

The concurrent observation of the citrate and impurity SERS features in the Cit(d_4)-AuNPs doesn't necessarily mean that the citrate-residues and solvent-impurities have comparable binding affinities to AuNPs or similar solution concentrations. This is because the ligand SERS intensity depends not only on the ligand quantity on AuNPs, but also its SERS activity. Earlier research has shown that the SERS activity of different organothiols can readily differ by five orders of

magnitudes [121]. Such SERS activity differences make it difficult to use SERS for a comprehensive understanding of the ligand composition on the AuNP surfaces. However, the concurrent appearance of the C-D and C-H stretching features in the Cit(d_4)-AuNPs provided unequivocal evidence for citrate-residue and solvent-impurity adsorptions.

2.4.2 XPS study of air- and solvent-borne chemical adsorption onto gold

The direct evidence showing both air- and solvent-borne impurities can rapidly adsorb onto gold surface come from XPS data obtained with gold film sputter-coated onto silicon (Figure 2.6). Opening to ambient air introduces significant carbon-containing contaminants onto the gold film surfaces of both the as-prepared gold film and the one freshly cleaned with X-ray etching (Figure. 2.6A and 2.6E). Dipping into double-distilled Nanopure water for as short as 10 min significantly increases the carbon and oxygen-containing contaminants (Figure 2.6F). The only sample that contain no significant carbon and oxygen species is the gold film that is cleaned *in-situ* by X-ray etching inside the XPS chamber followed with XPS characterization (Figure. 2.6D). This sample of cleaned gold film has never left the high-vacuum before the XPS characterization.

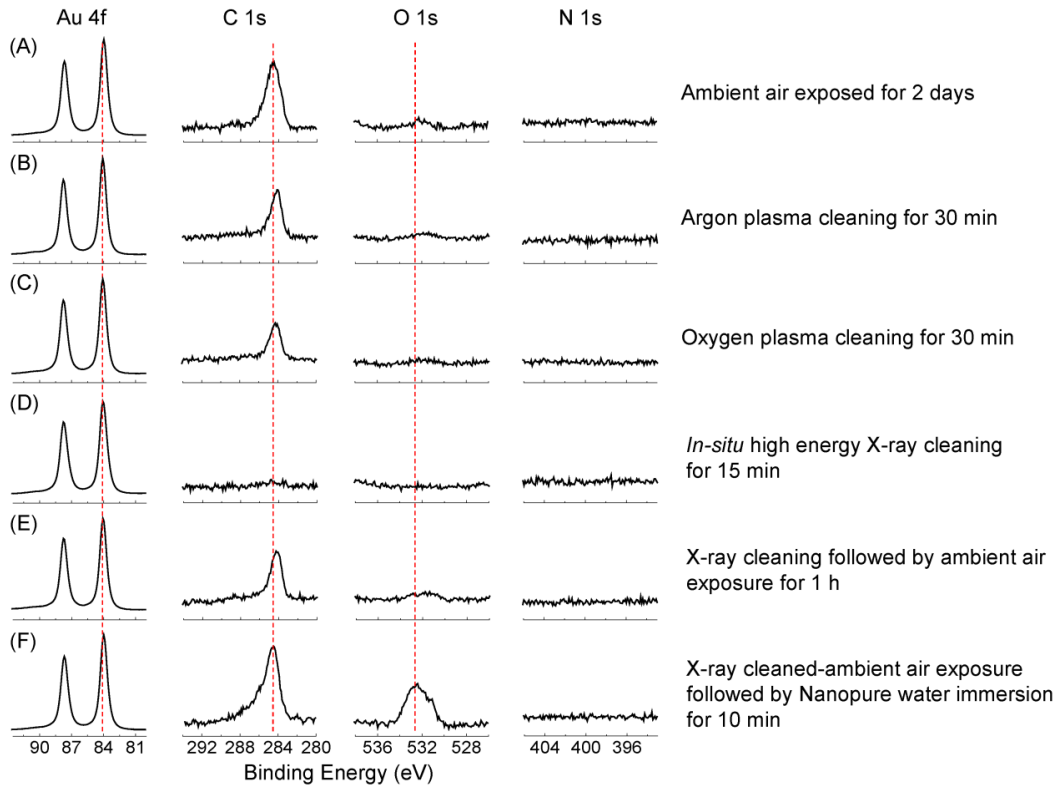

Figure 2.6 XPS spectra of planar gold film prepared by sputter-coating. (A) as-prepared gold film that has been exposed to the ambient air for 2 days. The gold films treated with (B) argon and (C) oxygen plasmas, for 30 min. (D) Gold film cleaned *in-situ* with high-energy X-ray radiation inside the XPS chamber for 15 min. (E) The same gold film used for (D) but after exposing it to ambient air for 1 h. (F) The same sample used for (E) but after immersing it in Nanopure water for 10 min.

Note: The XPS peaks for C1s, O1s, and N1s in all spectra are normalized so that the Au4f intensities are identical for the compared samples.

The observation of the carbon species present on the argon and oxygen plasma-cleaned sample has two possible explanations (Fig. 2.6B and 2.6C). Either the plasma cleaning is inadequate to remove the air-borne chemical adsorbates onto the planar gold film or the air-borne chemicals adsorption is so fast that the cleaned surface is re-contaminated during the sample transfer from the plasma cleaner to the XPS instrument that are located in the same room. Regardless of the causes, the data in Fig. 2.6 indicates that one must consider that air- and solvent-

borne impurity adsorption may be occurring to the nanoparticle surfaces. Adsorption of air- and solvent-borne chemicals should more readily occur onto AuNPs than onto planar gold film. AuNPs have larger surface-to-volume ratios and likely contain more reactive surface defects and vertices than planar gold films. Indeed, adsorption of carbon-containing air-borne impurities onto nanomaterial has been observed before [122-123]. The substantial increase in the oxygen XPS signal in the water-immersed X-ray-cleaned gold film (Figure 2.6F) observed in this work provides a direct evidence that solvent impurities can easily be adsorbed or deposited onto gold surface, either during the water immersion and/or the sample drying process. It also indicates the impurity adsorbates are relatively rich in oxygen.

2.4.3 SERS and XPS study of ligand-treated citrate-reduced AuNPs

The *in-situ* SERS measurement data indicate that citrate-residues on AuNPs can be displaced with all the investigated ligands (Figure. 2.7 and 2.8) including both HT and DDT, ligands that were also used by Shumaker-Parry *et al.* [96] The C-D stretching SERS feature in the ~2100 cm^{-1} region of the as-synthesized Cit(d_4)-AuNPs ((g) in Fig. 2.7H and (e) in Figure. 2.8F) disappeared in the SERS spectra of organothiol-, adenine-, halide-, and disulfide-treated Cit(d_4)-AuNPs. The SERS spectra of the ligand-treated AuNPs are totally dominated by the Raman feature of the added ligands, confirming both successful ligand binding and successful citrate-residue displacement. This is in sharp contrast to the conclusion drawn recently drawn by Shumaker-Parry *et al.* from their *ex-situ* XPS and ATR-FTIR studies that the citrate-residue on AuNPs is highly resistant to organothiol displacement. [96]

Adenine displaces both citrate and water impurities, while halide only displaces citrate, but not the water impurities (Figure 2.8). There is no detectable C-D stretching feature, the marker peak of deuterated citrate, or impurity sp^3 C-H stretching feature in the SERS spectra obtained

with adenine-treated AuNPs. However, the halide treatment completely removes the C-D stretching peak, but not the C-H stretching peak contributed by impurity adsorbates. The data shown in Figure 2.7 and 2.8 indicate that the citrate can be readily displaced, not only by sulfur compounds that bind to AuNP through formation of Au-S bonds, but also by ligands that can bind only nonspecifically to AuNPs.

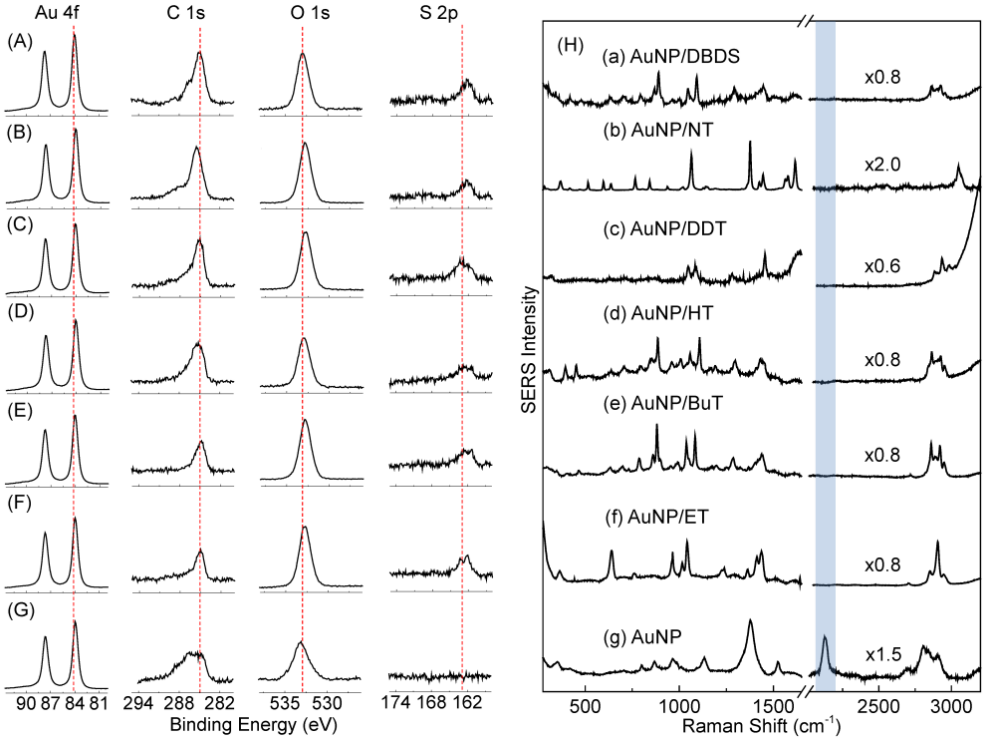

Figure 2.7 Comparison of XPS and SERS spectra of ligand-functionalized Cit(d_4)-AuNPs with unfunctionalized Cit(d_4)-AuNPs. The corresponding ligands in the XPS spectra from (A) to (F) are DBDS, NT, DDT, HT, BuT, and ET, respectively. The XPS spectra of (G) is for the unfunctionalized as-prepared Cit(d_4)-AuNPs. (H) SERS spectra of (a) DBDS-, (b) NT-, (c) DDT-, (d) HT-, (e) BuT-, and (f) ET-treated Cit(d_4)-AuNPs in solution. The SERS spectrum in (g) is for as-prepared Cit(d_4)-AuNPs.

Note: The region highlighted is for the C-D Raman stretching region which shows the complete disappearance of C-D feature after the ligand functionalization. The nominal concentrations of Cit(d_4)-AuNPs, DBDS, NT, DDT, HT, BuT, and ET are 7.0 nM, 50 µM, 25 µM, 50 µM, 50 µM, 50 µM, and 50 µM, respectively. The XPS peaks for C1s, O1s, N1s, and S2p in all XPS spectra are normalized so that the Au4f intensities are identical for the compared samples.

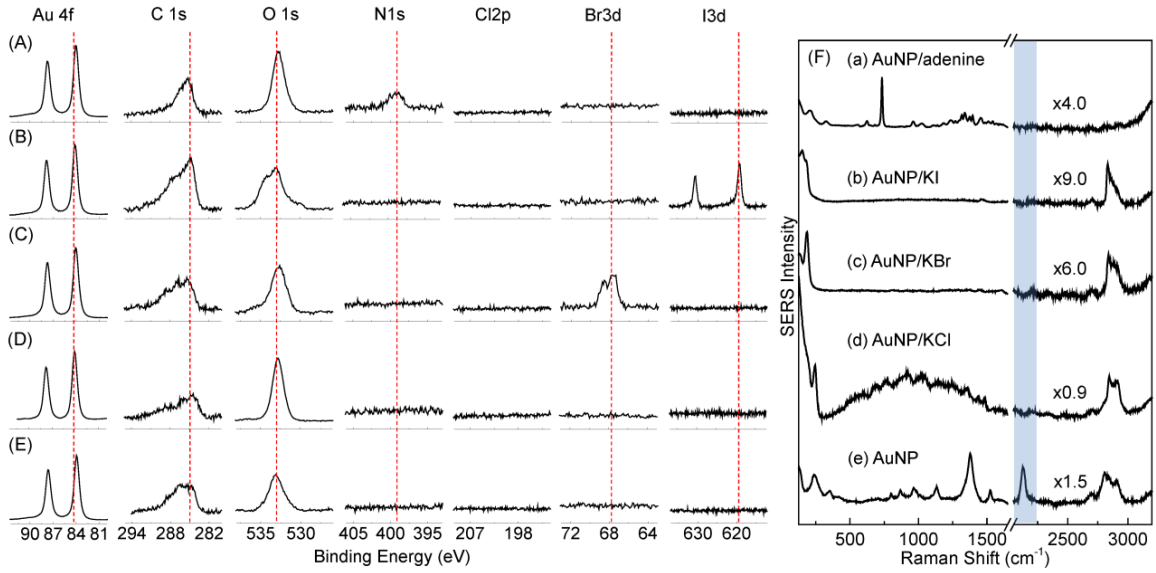

Figure 2.8 Comparison of XPS and SERS spectra of ligand-functionalized Cit(d_4)-AuNPs with as-prepared Cit(d_4)-AuNPs. The ligands used in (A) to (D) are adenine, KI, KBr, and KCl, respectively. The XPS spectra of (E) is for the as-prepared Cit(D_4)-AuNPs. (F) SERS spectra of (a) adenine-, (b) KI-, (c) KBr-, and (d) KCl-treated Cit(d_4)-AuNPs in solution. The SERS spectrum in (e) is for as-prepared Cit(d_4)-AuNPs.

Note: The region highlighted is for the C-D Raman stretching region which shows the complete disappearance of the C-D feature after ligand functionalization. The multiplier shown with each spectrum in the plot is the scaling factor for the spectral features in the ~2050-3100 cm^{-1} region in comparison to its spectral features below ~1600 cm^{-1}. The nominal concentrations of Cit(d_4)-AuNPs, adenine, KI, KBr, and KCl are 7.0 nM, 25 µM, 50 mM, 50 mM, and 50 mM, respectively. The XPS peaks for C1s, O1s, N1s, Cl2p, Br3d, and I3d in all XPS spectra are normalized so that the Au4f intensities are identical for the compared samples.

In sharp contrast to the rich diverse SERS spectral features observed among the ligand-treated samples, the *ex-situ* XPS data obtained with the solvent-dried AuNPs samples, regardless of their ligand treatments, are highly similar (Figure 2.7 and 2.8). There are similar carbon and oxygen XPS peaks in all the ligand-treated samples regardless of the ligand types used in the studies. Similar XPS data were reported before and the carbon and oxygen species were attributed to the citrate residues in the as-synthesized and ligand-treated AuNPs. [96] However, the SERS data

presented in our current work provides unequivocal evidence of the complete citrate displacement. The most likely reason for the carbon and oxygen species observed in the XPS spectra of the ligand-treated AuNPs is the air- and/or solution-borne contaminants deposited onto the solvent-dried XPS samples. This is supported by the observation that O1s and C1s XPS features obtained with the Cit(d_4)-AuNPs, with and without ligand treatment, are very similar among themselves. They are also very similar to the water-immersed planer gold film (Figure 2.6F) and the borohydride-reduced AuNPs (Figure 2.6D and 2.6E). This is true in spite of the fact that perfectly clean gold films are free of both carbon and oxygen, while the borohydride-reduced AuNPs have no carbon in any of its reactants.

Experimental evidence showing that the solvent-drying can load impurity adsorbates onto the ligand-functionalized XPS samples comes from the data obtained with MBI-treated Cit(d_4)-AuNPs in Figure 2.9. Figure 2.9A and 2.9B show XPS data obtained with the as-synthesized and MBI-functionalized Cit(d_4)-AuNPs. XPS data demonstrate that MBI-functionalized AuNPs contain relatively large amount of oxygen. The atomic ratio of oxygen, nitrogen, and sulfur with respect to gold on the dried XPS samples of MBI-functionalized AuNPs is 1.0:0.2:0.6. This is estimated from their respective XPS signals (Figure 2.9B), and XPS sensitivity factors. [124-125]

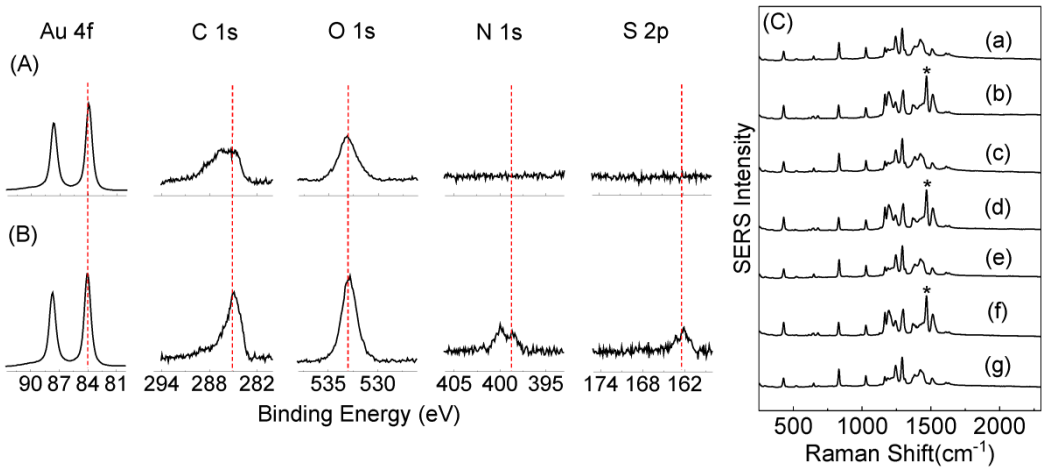

Figure 2.9 XPS spectra of (A) as-synthesized Cit(d_4)-AuNPs and (B) MBI-treated Cit(d_4)-AuNPs. (C) Comparison of MBI thiolate to thione conversion in wet and dried (AuNP/MBI) samples. SERS spectrum of (a) as-prepared MBI-containing Cit(d_4)-AuNPs in water. Spectra (b) to (g) in (C) are all acquired from the same sample used for spectrum (a) but the solvent was changed sequentially to (b, d, and f) 0.1 M HCl and (c, e, and g) 0.1 M NaOH.

Note: The peak with '*' is a marker for MBI thione. All spectra are normalized so that the peak intensities at 1028 cm^{-1} are the same. The nominal concentrations of Cit(d_4)-AuNPs and MBI are 7.0 nM and 25 μM, respectively. The XPS peaks for C1s, O1s, N1s, and S2p in all XPS spectra are normalized so that the Au4f intensities are identical for the compared samples.

MBI is an oxygen-free molecule. The oxygen detected by XPS for the MBI-containing AuNPs can be from three possible sources. The first is the citrate or water-impurity adsorption during the AuNP synthesis or during the MBI binding process in aqueous solution. However, this possibility is excluded on the basis of the *in-situ* SERS measurement. The SERS spectrum of the MBI-treated Cit(d_4)-AuNPs contains no detectable SERS of either the C-D stretching feature from citrate residue, or aliphatic C-H stretching feature from water-impurities (Figure 2.10). This indicates that there is no significant citrate or water-impurity adsorption onto the MBI-containing AuNPs. The second possible oxygen source is from MBI oxidation on AuNPs in solution. However, this possibility is excluded based on the observation that MBI maintains its ability for

thione-thiolate conversion on AuNP surfaces for at least 6 cycles (Fig. 2.9). Early research has shown that MBI is in its thiolate form on AuNPs in pH >2 solutions, but onverts into its thione form when the solution pH is <2. Presumably, the atom that is most susceptible to oxidative damage in MBI is sulfur. If significant oxidation damage occurred for MBI on AuNPs, changing solution pH would no longer convert MBI thiolate back to thione, and vice versa.

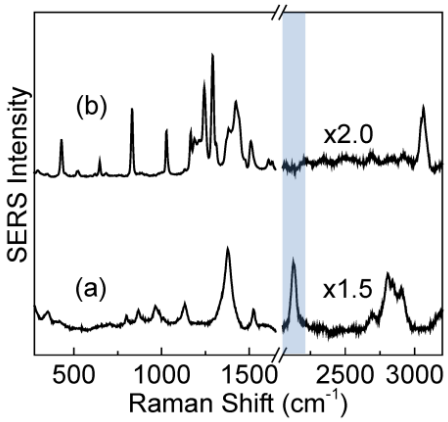

Figure 2.10 SERS spectra of (a) as-synthesized and (b) MBI-treated Cit(d_4)-AuNPs.

Note: The multiplier shown with each spectrum in the plot is the scaling factor for the spectral feature in the ~2050-3100 cm^{-1} region in comparison to its spectral features below ~1600 cm^{-1}. The region highlighted is for the C-D Raman stretching region which shows the complete disappearance of C-D feature after the ligand functionalization. The nominal concentrations of Cit(d_4)-AuNPs, and MBI are 7.0 nM and 25 μM, respectively.

The only other possible source for the oxygen XPS signal detected in MBI-containing AuNPs is from chemical deposits occurring from the solvent evaporation in the XPS sample preparation process. This is although MBI-containing AuNPs were washed extensively using Nanopure water. This conclusion is consistent with the observation that X-ray cleaned planar gold films, upon exposure of the gold surface to air and high-purity water, adsorbed surface contaminants (Figure 2.6E and 2.6F). These deposits can either be impurities originally in the

ligand-binding solution transferred to the XPS sampling substrate, or air-borne chemicals absorbed onto the AuNP during the sample drying process.

Mechanistically the simultaneous impurity adsorption during citrate-residue deposition onto the citrate-reduced AuNPs can proceed through multiple pathways. First, some of the impurity adsorbates might have intrinsically higher binding affinities than citrate to AuNPs. Second, the citrate residues on AuNPs are likely to be negatively charged. Recent studies show that electrolyte interaction with AuNPs is a highly complicated process in which the adsorption of charged species increases the binding affinity of its counter-ions but decreases the binding affinity of ions with the same charge. [109, 126] Cations and anions often form ion-pairs on the AuNP surfaces [126]. This ion pairing phenomenon offers an excellent explanation for why the same halides, but with different cations, have threshold concentrations for inducing AuNP aggregation that vary more than 1000 fold [126-127]. It also explains why the organodithiolate, but not the monothiolate, form S-S cross-linking on AuNP surfaces. [109] The fact that adenine displaces both citrate and the other impurities, but halide only displaces citrate and not impurity adsorbates from the citrate-reduced AuNPs, strongly suggests that there are cationic impurities adsorbed onto the citrate-reduced AuNPs. Earlier studies have shown that comparative adenine and halide binding affinities to AuNPs depend critically on the counter-ion that can be concurrently adsorbed onto the AuNPs.[109, 126] As an example, in the presence of organic cations, iodide dominates the surface of the AuNPs mixed with equal concentration of adenine and iodide, but adenine predominates on AuNPs mixed with an equal concentration of KI and adenine. [126]

2.4.4 Conclusions

In this study, we demonstrated that surface of citrate-reduced AuNPs contains both citrate-residues and impurity adsorbates from water, but not citrate-residues alone, as assumed by Shumaker-Parry et al [95-96]. The combined SERS and XPS measurements in this work indicate that the adsorbed impurities from water on AuNPs are rich in carbon, oxygen, and sp^3 C-H bonds. These species can be readily misinterpreted as citrate-residues. The finding that the citrate-residues on AuNPs can be readily displaced by a wide range of organothiols and organodisulfide is also in sharp contrast to the conclusion by Shumaker-Parry *et al.* that citrate-residue on AuNPs is highly resistant to organothiol displacement [96]. The facile displacement of citrate-residues explains why a wide range of ligands including organothiols [128-130], dyes [131], adenine , and halides [20] can be readily adsorbed and densely packed onto citrate-reduced AuNP surfaces. This work represents a significant step forward in the understanding of AuNP surface chemistry while countering recent papers that argue citrate is difficult to displace from AuNP surfaces [95-96]. The head-to-head comparison of the experimental results from the *in-situ* SERS and *ex-situ* XPS measurements enabled us to critically evaluate the reliability of XPS analysis for NP surface characterizations. Indeed, care must be exercised in the interpretation of the measurement results obtained with any *ex-situ* analytical method such as XPS and ATR-FTIR in which the NPs synthesized in solution are fully dried before spectral acquisitions. Adsorption of impurities present at very low solution concentrations and their deposition can also occur during both the NP synthesis and characterization processes. Ongoing efforts in this lab are on probing the compositions and properties of the ligand adsorbed onto citrate-reduced gold nanoparticle surfaces.

CHAPTER III

REACTIVE SILVER ADSORPTION ONTO GOLD

(Published in *J. Phys. Chem. C* **2017**, *121*, 22487-22495)

3.1 Abstract

Proposed mechanisms of monolayer silver formation on gold nanoparticle (AuNP) include AuNP-facilitated under-potential deposition, and anti-galvanic deposition in which the gold reduces Ag^+ into metallic Ag(0). Reported herein is the spontaneous reactive Ag^+ adsorption onto gold substrates that include both as-obtained and butanethiol-functionalized citrate- and $NaBH_4$-reduced gold nanoparticles (AuNPs), commercial high-purity gold foil, and gold film sputter-coated onto silicon. The silver adsorption invariably leads to proton releasing to the solution. The nominal saturation packing density of silver on AuNPs varies from 2.8±0.3 nmol/cm^2 for the AuNPs pre-aggregated with KNO_3 to 4.3±0.2 nmol/cm^2 for the AuNPs pre-functionalized with butanethiol (BuT). The apparent Langmuir binding constant of the Ag^+ with the pre-aggregated AuNPs and BuT-functionalized AuNPs are 4.0×10^3 M^{-1} and 2.1×10^5 M^{-1}, respectively. The silver adsorption has drastically effects on the structure, conformation, and stability of the organothiols on the AuNPs. It converts disordered BuT on AuNPs into highly ordered *trans* conformers but induces near complete desorption of sodium 2-mercaptoethane sulfonate and sodium 3-mercapto-1-propyl sulfonate from AuNPs. Mechanically, the Ag^+ adsorption on AuNPs most likely proceeds by reacting with molecules pre-adsorbed on the AuNP surfaces or chemical species in the solutions. This insight and methodology presented in this work is important for studying interfacial

interactions of metallic species with gold and for post-preparation modulation of the organothiol structure and conformation on AuNP surfaces.

3.2 Introduction

Gold has been attracted the interests from researchers for centuries. Owing to their unique chemical, electronic, and optical properties, a wide range of gold-based materials of different sizes and shapes have been fabricated for applications including electronics, biosensing, spectroscopy, and catalysis.[132-135] Understanding interfacial interactions of solid gold is fundamentally important for many of these applications. This is especially true for gold nanoparticle (AuNP)-based research due to its high surface-to-volume ratio. Indeed, surface functionalization is a popular strategy to enhance AuNP functionality, target-specificity, and biocompatibility.[17, 19, 28] While there are extensive works on the gold interactions with organic molecules and anionic species, organosulfur compounds[22, 26, 55, 136] and halides[20-21, 43, 137] in particular, the information on the metallic cation interaction with gold has been relatively scant.[23] Several recent studies show that Ag^+ can spontaneously deposit onto AuNPs,[53] and monolayer-protected gold cluster.[54] Redox reactions were believed involved in this silver deposition process where the Ag^+ is converted into metallic Ag^0 by either AuNP-facilitated under-potential deposition in which the silver ion can be reduced by a weak reducing agent such as ascorbic acid,[138-140] or by anti-galvanic (AG) deposition in which the more reactive silver is produced by Ag^+ oxidation of the less reactive gold.[141-144]

Reported herein are observations that silver binding to gold is a highly universal process and it binds to all gold substrates investigated in this work. This includes both as-obtained and butanethiol (BuT)-functionalized citrate- and $NaBH_4$-reduced AuNPs, high-purity commercial gold foil, and gold film sputter-coated onto the silicon substrate. Equally importantly, a series of

experimental evidences revealed that the adsorbed silver species most likely are silver salt or oxide in which silver remain as cationic, but not as atomic silver as reported in the earlier $Ag^{+/}$AuNP interactions.[141-142]

While BuT enables us to study the effect of study the effect of the Ag^+ binding on the structure and conformation of alkanethiol on the AuNPs, the ligands sodium 2-mercaptoethane sulfonate ($HS\text{-}(CH_2)_2SO_3Na$, MES) and sodium 3-mercapto-1-propyl sulfonate ($HS\text{-}(CH_2)_3SO_3Na$, MPS) provided conclusive evidence of the mobility of the Ag^+-treated organothiols. Earlier research has shown alkanethiols on planar gold surface are highly ordered in which the skeletal C-C and the C-S bonds are both their *trans* conformer to maximize the intermolecular van der Waals interactions.[145-147] They are however, totally disordered on AuNPs in which C-C and C-S bonds are both in a mixed *gauche* and *trans* conformers. This is due to the AuNP surface defects, curvatures, and vertices.[148] Interestingly, however, the alkanethiols on the aqueous silver nanoparticle (AgNPs) surface are highly ordered, i.e, their C-C and C-S bonds are both in predominantly *trans* conformers despite of the inevitable AgNP surface defects and curvatures.[128] It was speculated that Ag^+ binding to the AgNP proceeds through formation of Ag-alkanethiolate salt that is mobile on the nanoparticle surfaces.[128, 149] The Ag^+ conversion of the disordered BuT on AuNPs into highly order conformers described in this work provides a strong supporting evidence of this hypothesis.

This silver reaction with the ligand-functionalized AuNPs described in this work is different from the reported silver staining techniques used for enhancing the AuNP-based surface enhanced Raman spectroscopic (SERS) detection of protein,[150-153] DNA,[154-155] and heavy metal.[156] The latter uses hydroquinone as the reducing agent to convert Ag^+ ions to atomic silver.[152, 154, 157]

The possibility of the direct Ag^+ adsorption onto the ligand-functionalized AuNPs have not been considered. In contrast, the Ag^+ reaction in this work is carried out by simply mixing the $AgNO_3$ with the ligand-functionalized AuNPs with no reducing agents. For the sake of simplicity, the samples are abbreviated as (A/B)/C to represent a three-component mixture in which the first two components in parenthesis are mixed first before the addition of the third component.

3.3 Experimental section

3.3.1 Materials and equipment

All chemicals were purchased from Sigma-Aldrich and used as received. The purities of BuT, MES, and MPS are 99, 97, and 95%, respectively. The gold foil with the purity of 99.99% was purchased from Sigma-Aldrich. Citrate-reduced AgNPs with diameter of 50 nm were purchased from Nanocomposix Inc. Nanopure water (18 MΩ-cm) (Thermo Scientific) used throughout the experiments. UV-vis spectra were acquired with an Olis HP 8452 diode array spectrophotometer. PerkinElmer ELAN DRC II inductively coupled plasma-mass spectrometer (ICP-MS) was used for the sulfur and silver quantification. A LabRam HR800 confocal Raman microscope was used for Raman and SERS acquisitions with 633 nm laser excitation. Reflective Sample substrate (RSS) slides from Raminescent, LLC was used for all Raman and SERS acquisitions. The RSS slides are highly reflective substrates with negligible fluorescence and Raman background. The highly reflectivity can make the signal obtained with the RSS slides up to four times higher than that acquired with transparent quartz that are commonly used in the Raman spectral acquisitions (Figure 3.1).

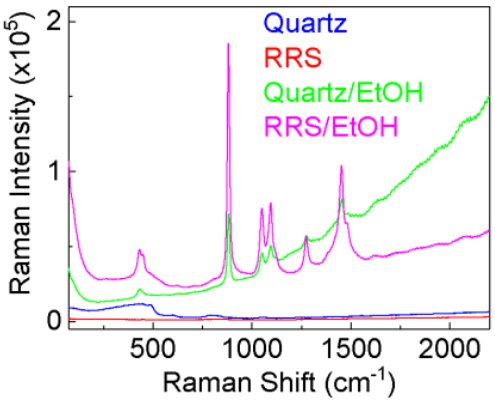

Figure 3.1 Raman spectra obtained on (blue) quartz slide, (red) RSS slide, (green) ethanol solution deposited on quartz slide, and (pink) ethanol solution deposited on RRS slide. The acquisition times for background and ethanol are 200 and 50 s, respectively.

3.3.2 AuNP synthesis

Citrate-reduced and $NaBH_4$-reduced AuNPs were synthesized using the same method described in the experimental section in chapter two.

3.3.3 Fabrication of sputter-coated gold films

The sputter-coated gold films were fabricated as described in the experimental section in chapter two.

3.3.4 Preparation of organothiol-functionalized AuNPs and AgNPs

An equal volume organothiol prepared originally in ethanol and diluted with 18 MΩ-cm Nanopure water was mixed with as-synthesized citrate-reduced AuNPs (or commercial AgNPs) and the mixture was vortex mixed. Unless stated otherwise, the organothiol-containing AuNPs and AgNPs were prepared by mixing the NPs with excess organothiols. All samples were incubated overnight to allow the AuNP (or AgNP) aggregates to settle to the bottom of the vials before solvent washing removal of the excess organothiols.

3.3.5 $AgNO_3$ treatment for the organothiol-functionalized AuNPs

A known concentration of $AgNO_3$ solution was added to the washed organothiol-functionalized AuNP aggregates and vortex mixed. The reaction mixture was left overnight at ambient conditions. The $AgNO_3$-treated organthiol-functionalized AuNPs were washed with Nanopure water to removal of the excess $AgNO_3$ before SERS acquisitions. For the time-dependent SERS measurements for the silver-treated BuT-functionalized AuNPs, an aliquot of ((AuNP/BuT)/$AgNO_3$) were taken out from the reaction mixture at pre-defined time intervals.

3.3.6 $AgNO_3$ reaction with BuT

Equal concentrations (10 mM) of $AgNO_3$ and BuT was vortex mixed, and the reaction mixture was left overnight at ambient condition to allow the Ag-butanethiolate salt to precipitate. The precipitate was washed to remove the reactant and then transferred to the RRS slide for Raman spectral acquisition.

3.3.7 Raman and SERS spectral acquisitions

Normal Raman spectra of as-received BuT and Ag-BuT salt were acquired with 13 mW laser power while for SERS spectra, the laser power before the microscope objective was 1.3 mW. All Raman and SERS spectra were acquired using Olympus 10× objective (NA=0.25) and the spectrograph grating was 300 grooves/mm. The acquisition times for normal Raman and SERS spectra were varied between 20-200 s. The Raman shift was calibrated with a neon lamp, and Raman shift accuracy was ~0.5 cm^{-1}.

3.3.8 ICP-MS quantification of the silver and organothiol adsorption on AuNPs

After the $AgNO_3$ addition, the (AuNP/organothiol)/$AgNO_3$ mixture was centrifuged at 9000 rpm for 1 h. Then the supernatant and the pellet were separated. The AuNP-containing pellet

was centrifuged-wash to remove the free organothiol and free Ag^+ ions. A known volume of freshly prepared aqua-regia solution (Warning: Aqua regia is very corrosive and must be handled with extreme caution) was added to the washed-pellet to digest the sample. The amounts of organothiols remained adsorbed onto AuNPs were quantified for the digested-washed-pellets by using ICP-MS instrument equipped with a dynamic reaction cell. To amount of released organothiol by the Ag^+-treated organothiol-containing AuNPs is also quantified by aqua regia solution digesting a known volume of the unwashed supernatant separated during the first centrifugation separation.

3.3.9 pH measurements of (AuNPs/BuT), (AuNPs/$AgNO_3$)/BuT, and $AgNO_3$/BuT

For (AuNPs/BuT), a volume of 50 mL of as-synthesized AuNPs were centrifuged and the final volume of solution that contains the aggregated AuNP precipitate was 2 mL. Then the solution was equally split into two vials. One for the AuNP-free top layer and the other for AuNP-containing bottom layers. pH measurements were conducted 1 hour after adding 1 mL 100 μM BuT in a 50% ethanol/water mixture solvent into the vials containing the top-layer and bottom layer solutions. For (AuNPs/$AgNO_3$)/BuT, 50 mL as-synthesized AuNPs were first aggregated with 50 mM $AgNO_3$ and washed extensively with nanopure H_2O. The final volume of solution that contains the aggregated AuNP precipitate was 2 mL. This solution was then equally split into two vials. One contains the AuNP-free top layer and the other is AuNP-containing bottom layers. pH measurements were conducted after addition of 1 mL 100 μM BuT into both the top-layer and bottom-layer vials. For $AgNO_3$/BuT, the top layer refers to the pH of the 100 μM as-prepared $AgNO_3$ solution, while the bottom layer refers to the pH of the solution prepared by mixing 2 mL 100 μM as-prepared $AgNO_3$ with equal volume of 100 μM BuT in the 50% ethanol/water mixture solvent.

3.3.10 X-ray Photoelectron Spectroscopy (XPS) Measurements

All gold substrates (BuT-functionalized and unfunctionalized) were extensively washed with Nanopure water before XPS analysis. Citrate- and borohydride-reduced AuNPs were transferred onto clean silicon substrates while evaporated gold films and high purity gold foils were directly used for XPS analysis.

All XPS measurements were performed using a Thermo Scientific K-Alpha XPS system equipped with a monochromatic X-ray source at 1486.6 eV corresponding to the Al Kα line. The spot size was 400 μm^2 and the takeoff angle of the collected photoelectrons were 90° relative to the sample surface. The pass energy of survey spectra was 200 eV and the high-resolution core level spectra and the Ag MNN Auger regions were obtained with pass energy of 40 eV. The average number of scans obtained for each sample was 20 with a step size of 0.1 eV. A Constant Analyzer Energy mode was used for all the XPS measurements and "Avantage v5.932" software was used in XPS data analysis.

3.4 Results and discussion

3.4.1 Ag^+ adsorption onto gold surfaces

The spontaneous silver adsorption onto gold surfaces is evident from the XPS data obtained with the gold substrates with and without the $AgNO_3$ treatment (Figure 3.2). Both the citrate- and $NaBH_4$-reduced AuNPs were aggregated with KNO_3 and washed extensively with Nanopure water before $AgNO_3$ treatment and the XPS analysis. The AuNP aggregation and water washing is needed for removal of excess Cl^-, citrate, or borax brought to the AuNP synthesis solutions. Evidently, none of the gold substrates contains detectable Ag^+ XPS features without Ag^+ treatment (Figures 1A, 1C, 1E, and 1G), but significant Ag signal appears in the XPS spectra of silver-treated

gold substrates (Figures 1B, 1D, 1F, and 1H). The observed silver XPS feature must be due to the silver adsorbed onto the gold surface, but not the residue $AgNO_3$ deposited onto the gold surface during the XPS sample preparation process. This is because all silver-treated samples were extensively washed.

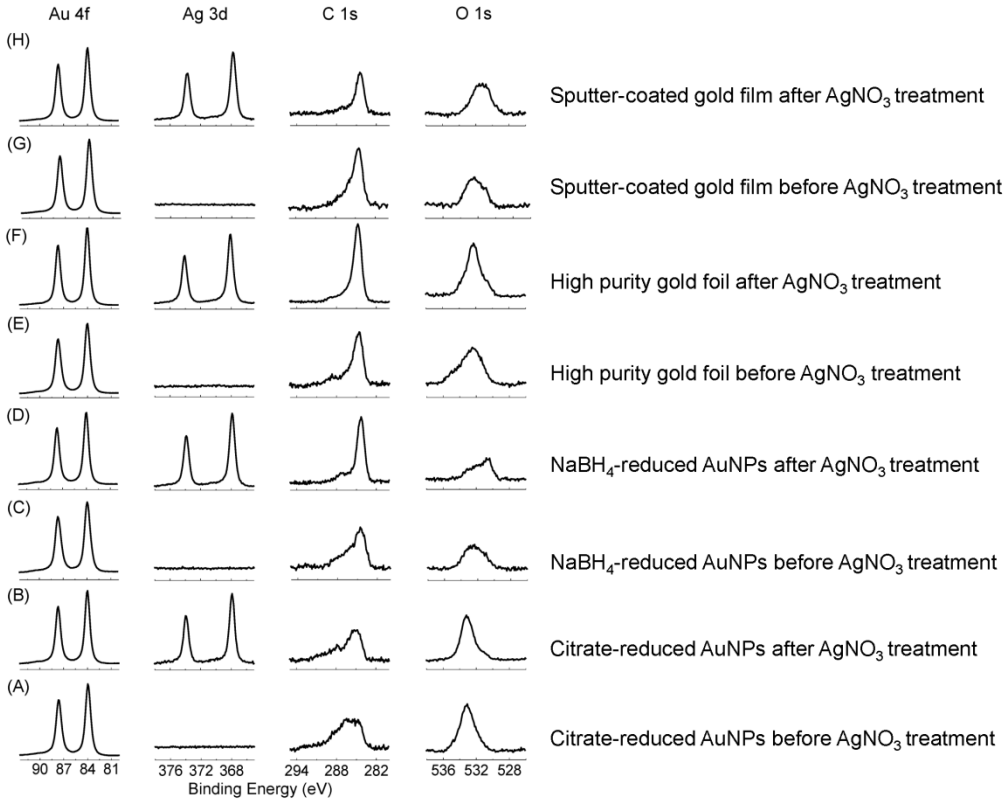

Figure 3.2 XPS spectra of the gold substrates (A, C, E, and G) before, and (B, D, F, and H) after $AgNO_3$ treatment. The gold substrates are citrate-reduced AuNPs (A and B), $NaBH_4$-reduced AuNPs (C and D), high purity gold foil (E and F), and sputter-coated gold film (G and H).

Note: The XPS peaks for Ag3d, C1s, and O1s in all spectra are normalized so that the Au4f intensities are identical in all samples.

Empirically, the Ag^+ adsorption onto the pre-aggregated citrate-reduced AuNP follows the Langmuir adsorption isotherm with a nominal binding constant of 4.3×10^3 M^{-1} and saturation

packing density of 2.8±0.3 nmol/cm^2 (Figure 3.3A). The Ag^+ saturation packing capacity is calculated by assuming the AuNPs are perfectly spherical with identical sizes.

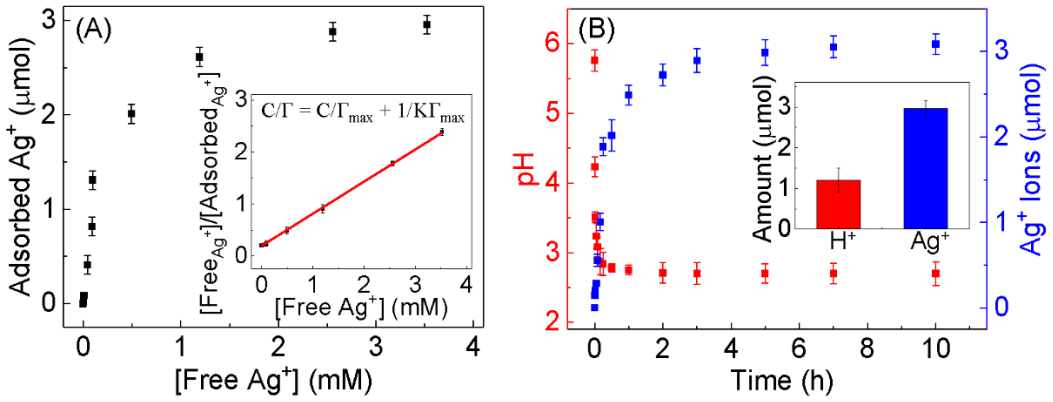

Figure 3.3 (A) Ag^+ adsorption isotherm onto citrate reduced AuNPs preaggregated with KNO_3 and washed with H_2O. Inset is the Langmuir fitting of the adsorption isotherm. (B) The time-course of the solution pH and the Ag^+ adsorption as the function of the time after the $AgNO_3$ addition onto the pre-aggregated AuNPs. The inset in (B) compares the total amount of silver adsorbed and proton released.

Note: The terms in the equation are, C: concentration of free Ag^+ ions at equilibrium, K: binding constant of Ag+ ions onto AuNPs, Γ: amount of adsorbed Ag^+, Γmax: maximum Ag^+ adsorption capacity.

Series of evidence indicates that the Ag^+ adsorption onto the gold surfaces follows the reactive pathway, but not direct adsorption as intact cation. First, there is significant pH drop accompanying with the Ag^+ adsorption onto gold surfaces (Figure 3.3B for the citrate-reduced AuNP-based adsorption and Figure 3.4 for the gold film). The pH value of the solution reduces from the initial ~5.8 to ~2.7. The amount of proton released to the solution strongly correlates to the amount of the Ag^+ adsorption. Second, control experiments conducted with BuT binding to the AuNPs pretreated with $AgNO_3$ shows that Ag^+ must have been converted into silver salt before the BuT adsorption. This is because BuT addition into the AuNPs pretreated with $AgNO_3$ has no

detectable effect on the solution pH, but a significant pH drop was observed when BuT is mixed with $AgNO_3$ (Figure 3.5). If Ag^+ is adsorbed as an intact ion, the BuT reaction with Ag^+ on AuNPs must generate proton as what has been observed.

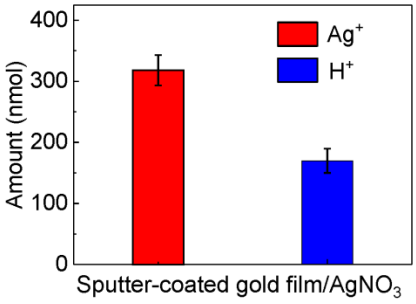

Figure 3.4 Bar plot of the amount of Ag^+ adsorbed onto sputter-coated gold film and the amount of proton released to the solution.

Note: 10 pieces of 0.5 cm × 0.5 cm silicon wafers that sputter-coated with gold were used to measure the pH of the solution after addition of $AgNO_3$. The nominal concentration of $AgNO_3$ is 10 mM.

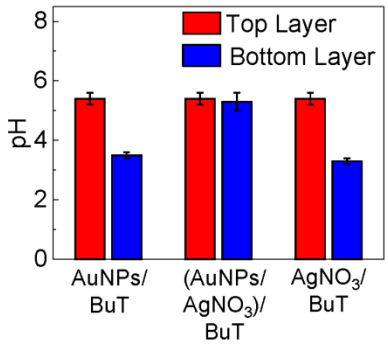

Figure 3.5 Bar plot showing the pH changes occurred in the solutions after the addition of BuT.

Besides the possible Ag^+ reaction with residue Cl^- ions brought into the AuNP solutions in the reaction $HAuCl_4$ that may remain adsorbed onto the extensively washed AuNPs, there most

likely other chemical reactions involved in the reactive Ag^+ binding to AuNPs and certainly for the Ag^+ binding to the gold foil and gold film. This is because first, there is no detectable Cl^- XPS feature in the washed AuNP aggregates (Figure 3.6), which is in sharp contrast to the intense Ag^+ XPS signal in the $AgNO_3$-treated samples. Second, the reaction of $Ag^+(aq) + Cl^-(aq) \rightarrow AgCl(s)$ involves no proton generation, and neither gold foil nor the gold film contains Cl^-.

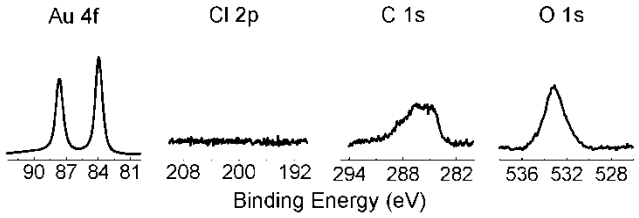

Figure 3.6 XPS spectra of citrate-reduced AuNPs obtained for Au4f, Cl2p, C1s, and O1s.

The possible proton generation reactions associated with Ag^+ binding includes silver oxide and silver hydroxide formation reactions depicted with Eq. 1 and Eq. 2, and the Ag^+ reaction with chemical residues adsorbed onto AuNP surfaces. Such chemical residues can be partially ionized citrate adsorbed onto the citrate-reduced AuNP surfaces, and proton-containing solvent impurities in the solutions.[158] Gold might have also acted as catalysis in some of those reactions. Unfortunately, it is currently impossible to pinpoint the reaction pathways because of the difficulties in identification of chemical species and the types of the reactions responsible for the reactive silver adsorptions.

$$2Ag^+ + H_2O \rightarrow Ag_2O + 2H^+ \quad (3.1)$$

$$Ag^+ + H_2O \rightarrow AgOH + H^+ \quad (3.2)$$

While the presence of the carbon and oxygen XPS features in citrate-reduced AuNPs may be due to the citrate-residues adsorbed onto the AuNP surface and impurity adsorption, the carbon XPS features in the as-received/as-prepared gold films and $NaBH_4$-reduced AuNPs must be from the contaminant surface adsorbates in the XPS samples. There are no carbon-containing reagents used in the gold film and $NaBH_4$-reduced AuNP substrate preparations. The appearance of the carbon species in the XPS sample obtained with the gold film is consistent with the early literature that the ambient chemicals can rapidly adsorbed onto the gold surfaces.[159-160]

3.4.2 Ag^+ adsorption onto the BuT-functionalized gold

Direct evidence showing the Ag^+ binding to the BuT-functionalized gold are shown with the XPS measurements (Figure 3.7). The as-prepared BuT-containing AuNPs contain strong C and S signal with no detectable silver XPS signal (Figure 3.7 A), but strong $Ag3d_{5/2}$ XPS peak (368 eV) appeared in the Ag^+-treated samples (Figure 3.7 B). It is noted that before $AgNO_3$ treatment and XPS measurements, all samples were washed extensively to ensure no excess BuT or $AgNO_3$ in the solution.

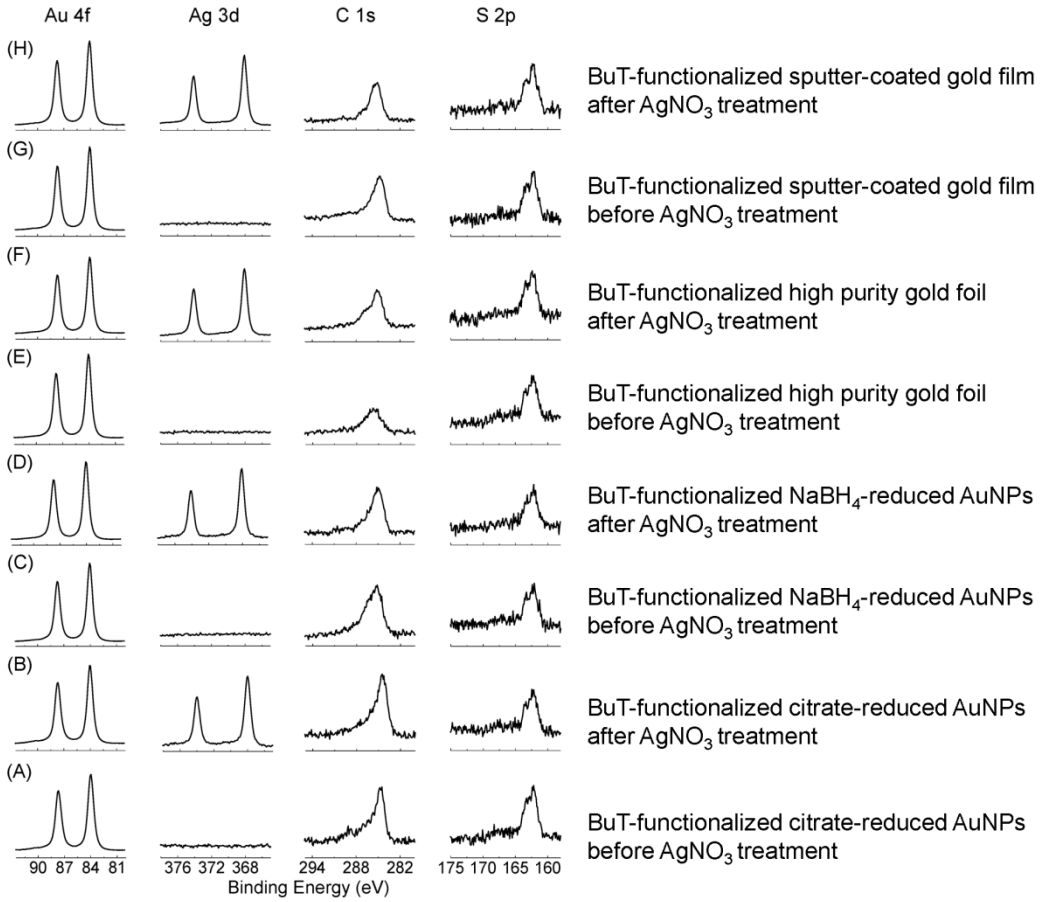

Figure 3.7 XPS spectra of BuT-functionalized gold substrates before and after $AgNO_3$ treatment. Spectra A, C, E, and G are before $AgNO_3$ treatment and spectra B, D, F, and H after treating the corresponding gold substrate with $AgNO_3$. The gold substrates are citrate-reduced AuNPs (A and B), $NaBH_4$-reduced AuNPs (C and D), high purity gold foil (E and F), and sputter-coated gold film (G and H).

Note: The XPS peaks for Ag3d, C1s, and S2p in all spectra are normalized so that the Au4f intensities are identical for the compared samples.

The silver adsorption induced a significant change in the structure and conformation of the BuT adsorbed onto AuNPs. The BuT SERS spectrum on the BuT-containing AuNPs is very different before and after the silver treatment (spectra (b) and (c) in Figure 3.8). While the SERS spectrum of BuT on the as-prepared AuNPs is same as that in literature,[128] it becomes very similar

to the SERS spectrum of the BuT-adsorbed onto the AgNP surfaces (Figures 3.8 d) and the normal Raman spectrum of Ag-BuT salt (Figure 3.8 e). As vibrational spectroscopic methods, Raman and SERS are known for their capability to provide fingerprint-like information of the probed molecules. The high similarity among the Raman spectra obtained with the Ag-treated BuT-containing AuNPs, the Ag-thiolate salts, and BuT-containing AgNPs indicates that the BuT all adopted the similar structure in the Ag-containing samples.

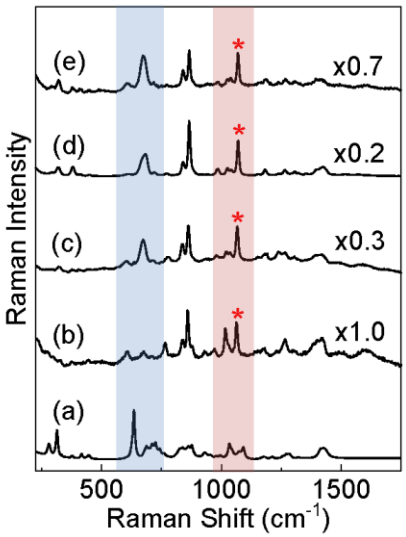

Figure 3.8 Comparison of normal Raman and SERS spectra of Ag^{+}-treated samples. (a) Normal Raman spectrum of neat BuT, SERS spectra of BuT-functionalized AuNPs (b) before and (c) after the Ag^{+} treatment, (d) SERS spectrum of BuT on AgNPs, and (e) normal Raman spectrum of silver-butanethiolate salt.

Note: The highlighted regions around 650 cm^{-1} and 1050 cm^{-1} are for the C-S and C-C stretching features, respectively. All SERS spectra are normalized to the peak denoted by "*". The multiplication factors are the normalization factors.

It is known that the alkanethiol adsorbed onto AgNPs and in Ag-thiolate salts are ordered.[128, 149] The SERS data in Figure 3.8 indicates that the BuT on the AuNP surfaces are also

highly ordered after the Ag^+-treatment. The marker C-S stretching peaks for the *trans* $\upsilon(C\text{-}S)_T$, and *gauche* $\upsilon(C\text{-}S)_G$ conformers are at ~680 cm^{-1} and ~610 cm^{-1}, respectively,[128, 161-162] while the marker C-C stretching peaks for *trans* $\upsilon(C\text{-}C)_T$, and *gauche* $\upsilon(C\text{-}C)_G$ are ~1070 cm^{-1} and ~1020 cm^{-1}, respectively. The C-S bond in the as-prepared BuT-containing AuNPs are in a mixed *trans* and *gauche* conformers (spectrum (b) in Figure 3.8), but converts to a *trans*-dominating conformer after the silver treatment (spectrum (c) in Figure 3.8). The intensity ratios of the $\upsilon(C\text{-}S)_T$ versus $\upsilon(C\text{-}S)_G$ and $\upsilon(C\text{-}C)_T$ versus $\upsilon(C\text{-}C)_G$ increases from ~1.1 ± 0.2 and ~1.2 ± 0.4 (spectrum (b) in Figure 3.8), in the SERS spectra obtained with the as-prepared BuT-containing AuNPs to 5.5 ± 0.5 and 5.2 ± 0.3, respectively, after the silver-treatment (spectrum (c) in Figure 3.8).

The Ag^+ induced structural and conformational change has several important implications. It first indicates that Ag^+ penetrated through the BuT overlayer self-assembled on the AuNP surface, converting the adsorbed BuT into Ag-thiolate salts. This is to our knowledge, the first experimental evidence showing that Ag^+ can replace Au in the Au-S bonding. Second, the successful detection of the Raman signal of Ag-thiolate on AuNPs indicates that the Ag-thiolate salts must remain in the close vicinity to AuNP surfaces so that it can experience SERS enhancement enabled by the AuNP surface plasmon. Collectively, this data indicates the Ag-butanethiolate must be mobile enough to be ordered, but remain confined on immediate AuNP surface to be SERS active.

The time-course of the Ag^+-induced BuT conformational change on AuNPs is significantly different from the Ag^+ adsorption and its accompanied proton releasing (Figure 3.9). While the Ag^+ adsorption and the proton releasing occurs within the first 30 mins following the $AgNO_3$ addition (Figure 3.9B), significant BuT ordering occurs only after the 30 mins of the silver

treatment (Figures 3.9A and 3.9C). This relative long time lapse between the silver adsorption and the BuT ordering strongly indicates that silver-butanethiolate ordering on the AuNPs is a highly cooperative process.

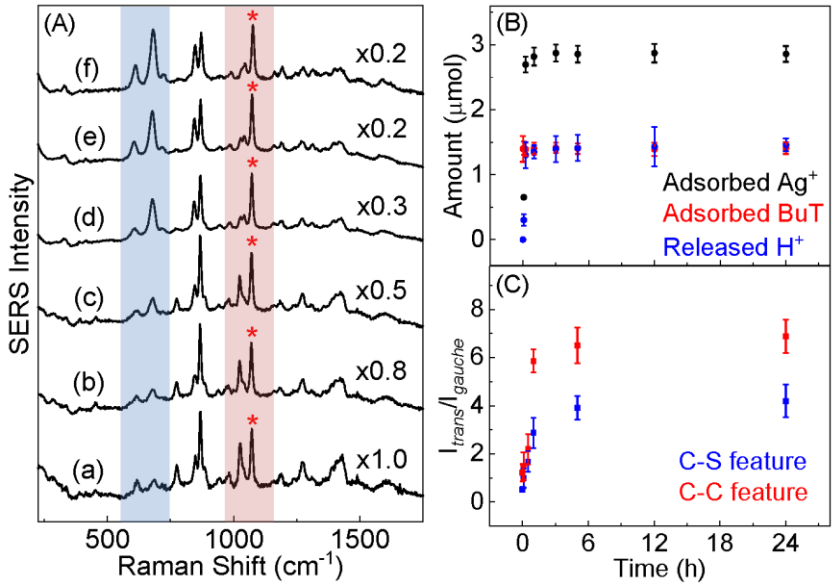

Figure 3.9 (A) SERS spectra of BuT adsorbed on AuNPs as the function of time after the Ag^+ addition. The time intervals are (a) 0 min, (b) 5 min, (c) 30 min, (d) 1 h, (e) 5 h, and (f) 24 h. (B) Comparison of the time-courses of Ag^+ adsorbed, BuT adsorbed, and proton released as the function of $AgNO_3$ addition to the BuT-containing AuNPs. (C) Intensity ratios of *trans* and *gauche* SERS features of C-S and C-C bonds as a function of time after Ag^+ addition.

Note: All SERS spectra are normalized to the peak denoted by "*". The multiplication factors are the normalization factors. The highlighted regions around 650 cm^{-1} and 1050 cm^{-1} are for the C-S and C-C stretching features, respectively. The nominal concentrations of AuNPs, $AgNO_3$, and BuT are 6.5 nM, 150 μM, and 100 μM, respectively.

Further supporting evidence that the Ag^+-induced BuT conformational change is a cooperative process comes from the observation that the degree of the Ag-butanethiolate ordering on the AuNPs depends critically on the amount of Ag-butanethiolate formed on the AuNP surface

(Figure 3.10). The amount of Ag-butanethiolate on AuNPs is adjusted by controlling the amount of BuT adsorbed onto AuNP prior to Ag^+ treatment (Figure 3.10A) and by varying the amount of Ag^+ added into the AuNPs pre-treated with excess BuT (Figure 3.10B). The saturation packing density of the BuT on the AuNPs synthesized in this work is 1.8±0.2 nmol/cm^2, similar to what have been reported before.[128] When 1 mL as-prepared AuNPs are treated with sub-monolayer amount of BuT (1 mL of 10 μM), no significant BuT conformational change is observed even when the amount of Ag^+ is more than sufficient to react with the surface adsorbed BuT (spectra (a) and (b) in Figure 6A). Conversely, no significant BuT conformational change is observed when the amount of Ag^+ added into the BuT-containing AuNP is adequate only to react with a fraction of surface-adsorbed BuT (spectra (a) and (b) in Figure 3.10B). In contrast, high degree of BuT ordering is observed only in the sample where AuNPs are fully packed with BuT and subsequently treated with sufficient amount of $AgNO_3$ (spectra (c) and (d) in Figure 3.10A, and spectrum in Figure 3.10B).

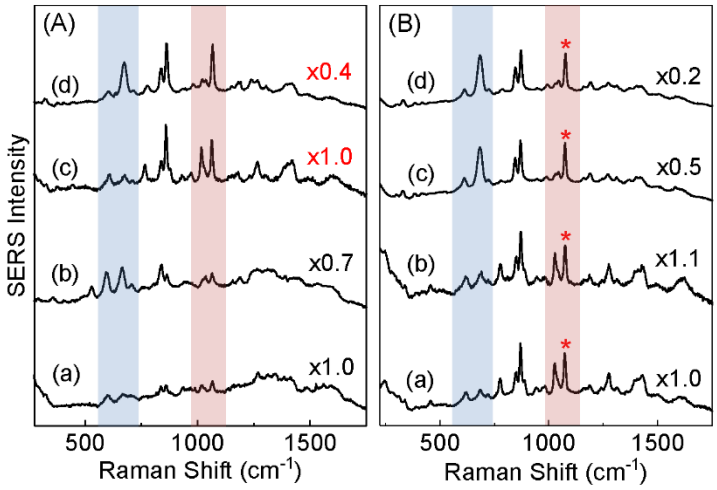

Figure 3.10 (A) Effect of the BuT packing density on Ag^+-treated BuT conformational change on AuNPs. SERS spectrum of AuNPs functionalized with 5 μM BuT (a) before and (b) after Ag^+ addition. SERS spectra (c) and (d) are SERS spectra of AuNPs functionalized with 100 μM BuT before and after the Ag^+ addition, respectively. The nominal concentration of $AgNO_3$ is 150 μM. (B) SERS spectra of AuNPs functionalized with 100 μM BuT and subsequently treated with $AgNO_3$ of different concentrations.

Note: The nominal concentrations of $AgNO_3$ are (a) 0, (b) 5, (c) 150, (d) 1000 μM. SERS spectra are normalized to the peak denoted by "*". The multiplication factors are the normalization factors. The highlighted regions around 650 cm^{-1} and 1050 cm^{-1} are for the C-S and C-C stretching features, respectively

Empirically, the reactive Ag^+ adsorption onto BuT-containing AuNPs also follows the Langmuir adsorption isotherm with a saturation packing density of 4.3±0.2 nmol/cm^2 and an apparent binding constant of 2.1×10^5 M^{-1} (Figure 3.11). Moreover, the $AgNO_3$ binding to the BuT-functionalized AuNPs also induces proton releasing, reducing the solution pH from 5.4±0.2 to 3.3±0.3. The ratio between the amount of BuT adsorbed, the Ag^+ adsorbed, and the proton released are approximately 1:2.4:1.2. The fact that amount of silver adsorption is significantly higher than adsorbed BuT have several important implications. First, besides the Ag^+ reacting with the surface-attached butanethiolate that likely proceeds with a stoichiometry of 1:1, there must be other

chemical processes responsible for reactive adsorption of the additional Ag^+. Second, the reaction products between the Ag^+ and the adventitious molecules most likely filled the void space between the immediate AuNP layer and the ordered Ag-butanethiolate salt. This is the Ag-butanethiolate molecules formed by Ag^+ reaction with the surface-attached BuT must be mobile and some of the Ag-butanethiolate molecules must be dislocated from the AuNP in order to overcome the constrain of the AuNP surface defects and curvatures to form an order all *trans* conformer. In other words, the reaction products between silver and the adventitious molecules level the ground for the Ag-butanethiolate salts to be ordered on AuNP surfaces. This hypothesis is consistent with the fact that saturation packing density of the Ag^+ on the BuT-containing AuNPs is significantly higher than the amount of adsorbed BuT.

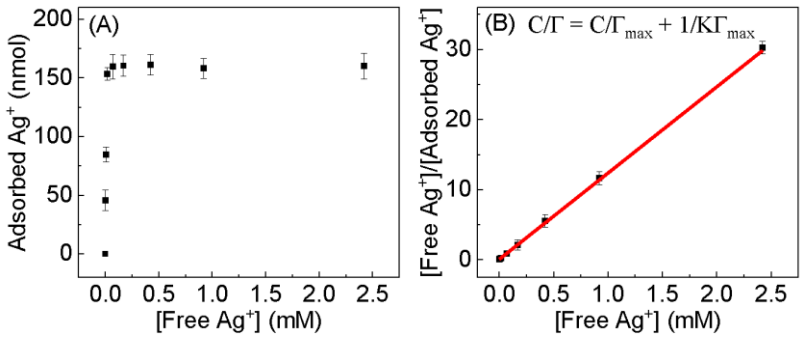

Figure 3.11 (A) Ag^+ adsorption isotherm of BuT-functionalized AuNPs. (B) Langmuir fitting of the adsorption isotherm.

Note: The terms in the equation are, C: concentration of free Ag^+ ions at equilibrium, K: binding constant of Ag^+ ions onto AuNPs, Γ: amount of adsorbed Ag^+, Γmax: maximum Ag^+ adsorption capacity. The BuT-containing AuNPs were prepared by mixing AuNPs and BuT with a nominal concentrations of 6.5 nM and 100 μM, respectively.

Further evidences showing the mobility of Ag-thiolate salt on AuNPs come from the Ag-treatment of the MES- and MPS-containing AuNPs (Figure 3.12). The Ag^+ treatment has no significant effect on dispersion of the BuT-containing AuNP aggregates or the amount of BuT on the AuNPs (Figure 3.12A). However, it induces the disaggregation and redispersion of the precipitated MES- ad MPS-containing AuNPs (Figures 3.12B and 3.12C), and near complete MES and MPS desorption from the AuNP surfaces (Figure 3.12D). MES and MPS desorption provide direct evidence that Ag-thiolate can be dislocated from the AuNP surfaces, a necessary condition for the Ag-thiolate to overcome the constrain of the AuNP surface curvature and defects to be ordered on the AuNP surfaces.

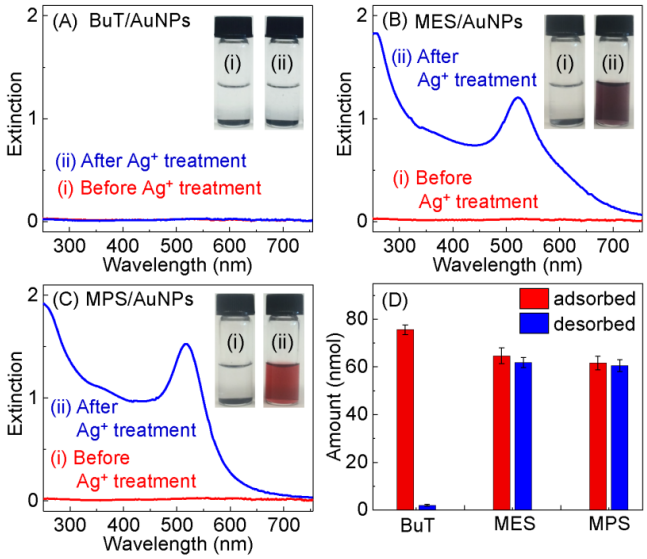

Figure 3.12 UV-vis spectra of (A) BuT-, (B) MES-, and (C) MPS-containing AuNPs (red) before and (blue) after the addition of $AgNO_3$. Insets are the optical images of ligand-containing AuNP aggregates (i) before and (ii) after addition of $AgNO_3$. (D) Comparison of the amount of adsorbed ligands onto AuNPs with the amount of desorbed ligands from AuNPs after the addition of $AgNO_3$.

Note: The nominal concentration of $AgNO_3$ is 1 mM.

Several reasons explain why Ag-butanthiolate, but not the Ag-MES or Ag-MPS salt remain on the AuNP surfaces. First, the strong intermolecular van der Waals forces among the alkyl chains enable the mobile Ag-butanethiolate salts to self-assemble into a supramolecular that will have much stronger van der Waals interaction with AuNP than the individual Ag^+-reacted MES and MPS molecules. The self-assembly among silver reacted MES and MPS molecules is difficult due to its bulky distal sulfonate groups. Second, the Ag-butanethiolate most likely has a lower solubility than the silver reaction products with MES and MPS. This should also facilitate the molecular assembly of the Ag-butanethiolate through the hydrophobic interactions and prevent the Ag-butanethiolate diffuse into the aqueous solvent. Nonetheless, the ordering of Ag-butanethiolate on AuNPs and the desorption of the Ag^+-treated MES and MPS indicate that Ag-thiolate are mobile on AuNPs.

Besides providing conclusive evidence of the universal silver adsorption onto gold surfaces, the XPS measurement also supports the conclusion that adsorbed silver remain as cationic silver indicated before, but not as atomic silver as suggested by the earlier studies.[141-142, 163-166] The average Auger parameter of $3d_{5/2}$, $M_4N_{45}N_{45}$ and $3d_{5/2}$, $M_5N_{45}N_{45}$ for adsorbed silver onto AuNPs are 724.56±1.03 and 719.20±0.35 (Table 3.1) respectively and it is within the range of earlier reported values for AgO.[167-169] In fact, Auger parameters reported for atomic silver $3d_{5/2}$, $M_4N_{45}N_{45}$ and $3d_{5/2}$, $M_5N_{45}N_{45}$ are 726.15±0.15 and 720.05±0.17 respectively.[167-169] Therefore, all this evidence support to the fact that the adsorbed silver exists as cationic silver on gold surfaces.

Table 3.1 XPS Ag 3d fitting parameters and Auger parameters for silver-containing samples

Sample	$3d_{5/2}$ Binding energy (eV)	Kinetic energy (eV)		Auger parameter (AP)	
		$M_4N_{45}N_{45}$	$M_5N_{45}N_{45}$	AP-3d5/2, $M_4N_{45}N_{45}$	AP-3d5/2, $M_5N_{45}N_{45}$
Ag	368.30[a]	358.20[a]	352.20[a]	726.50[a]	720.50[a]
AgO	367.50[b]	356.70[b]	-	724.40[a]	718.40[a]
Ag_2O	368.18	355.70	350.20	723.88	718.38
$AgNO_3$	368.38	355.50	350.00	723.88	718.38
AuNP/$AgNO_3$	368.88	354.60	349.90	723.48	718.78
(AuNP/BuT)/$AgNO_3$	368.13	357.50	351.50	725.63	719.63
(AuNP/$AgNO_3$)/BuT	368.68	354.80	350.40	723.48	719.08
$AgNO_3$/BuT	368.58	355.50	351.20	724.08	719.78

[a] from reference and [b] from reference.[170]

3.5 Conclusions

Using high purity gold foil, gold film sputter-coated onto silicon, and citrate- and borohydride-reduced AuNPs and several organothiols as the probing ligands, we demonstrated the spontaneous Ag^+ adsorption onto gold in aqueous solution are a highly general phenomenon in the types of the AuNPs and the AuNP surface modifications. Mechanistic study reveals that this silver reaction proceeds predominantly through reactive pathways some of which involves proton generations. The silver interactions with the organothiol-functionalized AuNPs has profound effects on the structure, conformation, and stability of the organothiols on AuNPs. It converts BuT from a disordered mix *trans* and *gauche* conformers into a highly ordered *trans* conformer, but induces near complete ligand desorption of MES- and MPS- from the AuNP surfaces. The Ag^+ induced BuT ordering is a highly cooperative process that occurs only when BuT is densely packed on AuNPs and completely reacted with Ag^+. This work provides the first direct evidence that Ag^+ can disrupt the Au-S binding and enhance the mobility of the organothiols on AuNPs. The insights and methodology provided in this work should be of general importance for studying metallic cation interactions with gold and for post-synthesis manipulating the organothiol structure and conformations on AuNPs.

CHAPTER IV

HYDROGEN SULFIDE INDUCES COMPLETE NONDESTRUCTIVE LIGAND DISPLACEMENT FROM AGGREGATED GOLD NANOPARTICLES

(Published in *J. Phys. Chem. C* **2018**, *122*, 2137-2144)

4.1 Abstract

Ligand displacement from gold is important for a series of gold nanoparticle (AuNP) applications. Complete nondestructive removal of organothiols from aggregated AuNPs is challenging due to the strong Au-S binding and the steric hindrance imposed by ligand overlayer on AuNPs and the narrow junctions between the neighboring AuNPs. Presented herein is finding that hydrogen sulfide (HS^-), an anonic thiol, induces complete and nondestructive removal of ligands from aggregated AuNPs. The model ligands include aliphatic and aromatic thiols (ethanethiol (ET), methylebenzenethiol (MBT)), organothiol (benzene dithiol (BDT)), thioamides (mercaptobenzenethiol (MBI) and thioguanine (TG)), and nonspecific ligand adenine. The threshold HS^- concentration to induce complete ligand displacement varies from 105 μM for MBI and TG, to 60 mM for BDT. No complete ligand displacement occurs when mercaptoethanol, the smallest water-soluble thiol is used as the incoming ligand. Mechanistically, HS^- binding leads to the formation of sulfur monolayer on AuNPs that is characterized with intense S-S bonds and S-Au bonds, but with no detectable S-H spectral features. The empirical HS^- saturation packing density and Langmuir binding constant on AuNPs are 960±60 pmol/cm^2 and 5.5±0.8 ×10^6 M^{-1}, respectively. The successful identification of an effective ligand capable of inducing complete and

nondestructive removal of ligands from AuNPs should pave way for using AuNP for capture-and-release enrichment of biomolecules that have high affinity to AuNP surfaces.

4.2 Introduction

Surface functionalization is important for gold nanoparticle (AuNP) applications in biosensing, surface enhanced Raman spectroscopy (SERS), and drug delivery.[55, 171-174] The most popular ligands for AuNP surface modifications are organothiols due to their ability to self-assemble onto gold through covalent Au-S bonds.[55, 175] However, removal of ligands adsorbed onto AuNPs is difficult. Existing wet-chemistry approaches for organothiol removal from AuNPs can be classified into two categories. The first is chemical oxidation method that uses H_2O_2 to oxidize the organothiol ligands.[20, 176-177] However, this approach is destructive. The removed organothiols are usually complex mixtures with little value for subsequent applications. The second method is through place exchange in which initial organothiol are replaced by an incoming organothiol.[178-181] While this method is nondestructive, its effectiveness for displacing ligands from aggregated AuNPs has, to our knowledge, not been quantitatively evaluated.

Indeed, place exchanging between two organothiols on AuNPs are both thermodynamically and kinetically challenging. The thermodynamic difficulty stems from the fact that the incoming and initial ligands are both organothiols that likely have similar binding affinities to AuNPs. The only way to enhance thermodynamic advantage of the incoming organothiols to displace the initial organothiols is to increase concentration of the incoming thiols. This is undesirable for ligand removal in aqueous solution because many organothiols are poorly soluble in water, and they often have the irritating rotten-egg odor. The kinetic challenge is due to the fact that the incoming ligand must overcome the first-comer advantage, i.e, steric hindrance

imposed by the initial ligands that limit the access of the incoming ligands to the AuNP surfaces.[182] Organothiol displacement on AuNPs proceeds predominantly through associative exchange, but not the dissociative pathway.[182] The incoming ligand must penetrate through the overlayer of the initial ligand on AuNPs in order to initiate the place exchange process.[182] Such first-comer advantage explains why the competitive mercaptobenzimidazole (MBI) and adenine binding to pegylated AuNPs depends strongly on the sequence how MBI and adenines are mixed with pegylated AuNPs.[182]

Displacing ligands on aggregated AuNPs are even more challenging. The junction between neighboring AuNPs can be exceedingly small due to the strong interparticle Van der Waals interactions. The size of the incoming ligands must be small enough in order to penetrate into these junctions and initiate the ligand displacements. Otherwise initial ligand will remain on the AuNP junctions even the incoming ligand has higher binding affinity to AuNPs. As an example, when using tripeptide glutathione as the incoming ligand, less than 70% of adenine can be displacement from aggregated AuNP. This is in spite of the fact the AuNP binding affinity of adenine is significantly smaller than that of gulathione.

We have recently demonstrated that the $NaBH_4$ is highly effective for inducing ligand desorption from AuNPs including aggregated AuNPs. Computational simulation revealed that hydride derived from $NaBH_4$ has significantly higher binding affinity to AuNPs than organothiols. Presumably, the small size of hydride ions has also played a critical role for the efficient $NaBH_4$ removal of the AuNP surface adsorbates. Unfortunately, however, this method has two key drawbacks. First, hydride has a relatively short lifetime in water. One must remove the displaced organothiols from the ligand displacement solution before they are re-adsorbed onto AuNPs upon

the hydride depletion. Second, hydride is a strong reducing agent which can induce structural modifications of organothiols. One such example is the MBI desulfurization on AuNPs.

The objective of this research is to identify an incoming ligand that can effectively, completely, and nondestructively displace organothiols from aggregated AuNPs. Apparently, the incoming ligand should have at least comparable AuNP binding affinity as organothiols and it must be small enough for penetrate through the ligand overlayer and the AuNP junctions to trigger the displacement. Guided by those considerations, we evaluated herein effectiveness of mercaptoethanol (ME, Figure 4.1), the smallest water-soluble organothiol, and NaHS is the smallest anionic thiol for the ligand displacement from the aggregated AuNPs.

The choice of NaHS is inspired by extensive literature on the H_2S and Na_2S binding to planar and nanostructured gold surfaces.[42, 183-185] H_2S vapor induces the organothiol desorption and reorientation on the planar gold.[186] Aqueous Na_2S form polysulfide and Au-S bonds on the AuNP surfaces.[184, 187] However, thermodynamic and kinetic parameters of AuNP binding of these sulfide species are not available. Quantitative information on the degree of the ligand displacement by these sulfide species is unavailable. Moreover, the polysulfur structure and conformation formed by the sulfide adsorption on the AuNP is unclear either. Is the S-S linking formed among the monolayer sulfur species on AuNPs or between different layers of sulfur species accumulated onto AuNP surfaces?

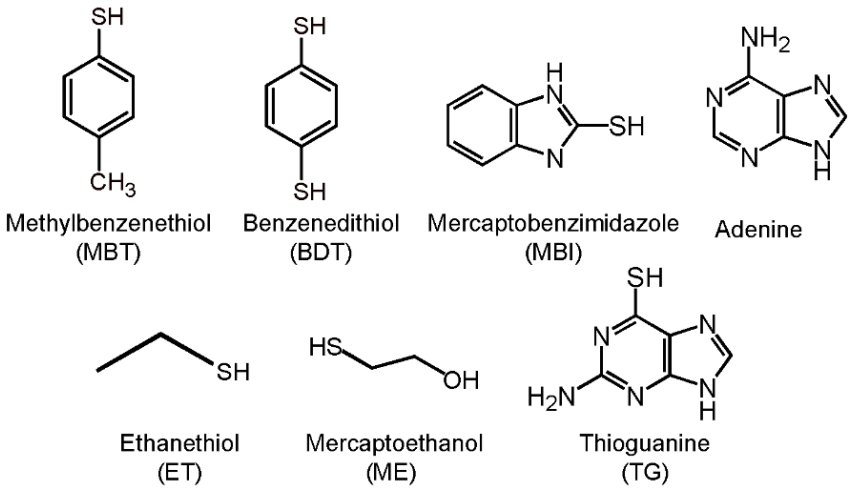

Figure 4.1 Molecular structures of the model ligands.

We choose NaHS instead of H_2S and Na_2S is for the ease of sample handling. NaHS doesn't have the nauseous order of H_2S, nor is it as corrosive as Na_2S. However, the conclusion drawn from the NaHS binding are most likely applicable to that by Na_2S. When dissolved in water the major sulfur species is HS^- in both NaHS and Na_2S, This is because the two pKa(s) of H_2S are pKa values (pKa_1=7.1, and pKa_2= 19.0), respectively.[188] Experimental confirmation of the SH^- presence in both NaHS and Na_2S solutions will be shown later.

The model ligands (Figure 4.1) used in this work include monothiols (ethanethiol (ET) and methylbenzenethiol (MBT)), dithiol (benzenedithiol (BDT)), and thioamides (MBI and TG) that have thione and thiol tautomeric forms, and non-specific ligand (adenine). This set of ligands differs in their thiol content (0, 1, and 2 thiol groups), enabling us to evaluate the general applicability of the experimental observations. They have been used previously in the $NaBH_4$- and KI-induced ligand displacement studies.[20, 189] This allows the compare and contrast ligand displacement by HS^- with that by the $NaBH_4$ and KI. This work is organized by first presenting

the quantitative NaHS binding to AuNPs, followed by the ligand displacement studies. For the sake of simplicity, we will use A/B to represent the mixture solutions of A and B, and an addition of solution C to the A/B mixture will be denote as (A/B)/C.

4.3 Experimental section

4.3.1 Materials and equipment

All chemicals were purchased from Sigma-Aldrich and used as received. The SERS spectra were acquired using the LabRam HR800 confocal Raman microscope system with a 633 nm HeNe Raman excitation laser. The normal and SERS spectra were acquired with the background-free reflective sample substrates (RSS) obtained with Raminescent LLC,[190] The Raman shift was calibrated with a neon lamp. UV-vis spectra were acquired with an Olis HP 8452 diode array spectrophotometer. PerkinElmer ELAN DRC II inductively coupled plasma-mass spectrometer (ICP-MS) equipped with dynamic reaction cell was used for the quantification of the sulfur onto AuNPs. The atomic absorption spectroscopic (AAS) determination of the NaHS concentration in its bulk solution was performed with a Shimadzu AA-7000 atomic adsorption spectrophotometer.

4.3.2 Quantification of the NaHS concentration

Sodium hydrogen sulfide hydrate (Cat. No. 161527) is hydroscopic. The sodium hydrogen sulfide concentration in its stock solution was experimentally quantified before use by taking advantage of the stoichiometric between NaHS and $Pb(NO_3)_2$ that forms insoluble PbS in water. Briefly, a 10 mL stock solution with a nominal NaHS concentration of 4.0 mM estimated by assuming no water in the solid sodium hydrogen sulfide are mixed with equal volume of a standardized 4.0 mM $Pb(NO_3)_2$ in a centrifugation tube. This reaction solution was briefly vortex

mixed and left sitting at the ambient temperature overnight to allow the PbS precipitate settle down to the centrifugation tube. The amount of the unreacted excess Pb^{2+} is then experimentally quantified using atomic absorption spectroscopic method. The calibration curves used for Pb^{2+} quantification is obtained with the commercial 1000 mg/L Pb^{2+} standard for AAS. The actual NaHS concentration in its stock solution is ~2.6 mM, indicating that there is ~35% water in the sodium hydrogen sulfide hydrate used for the solution preparation. The NaHS concentration discussed hereafter are all based determined NaHS concentration.

4.3.3 AuNP synthesis

Citrate-reduced AuNPs were synthesized using the same method described in the experimental section in chapter two.

4.3.4 ICP-MS quantification of sulfur species adsorbed onto AuNPs

As-synthesized AuNPs (2 mL) were mixed with 2 mL of aqueous NaHS of different concentrations. The AuNP/NaHS mixtures were centrifuged at 9000 rpm for 1 h. The AuNP-free centrifugation supernatants and the AuNP precipitates were separated. The amount of the sulfur adsorbed was independently quantified using two approaches. The first was determining the amount of excess sulfur that was present in the centrifugation supernatant. The second quantified the amount of the sulfur adsorbed onto the AuNP precipitates. After solvent washing to remove the possible free sulfur species from the centrifuged AuNPs, a known volume of freshly prepared aqua regia solution (warning: aqua regia is corrosive and should be handled with extreme caution!) was added to digest the AuNPs. The amounts of sulfur species adsorbed onto AuNPs were then quantified with ICP-MS measurements. The ICP-MS calibration curve was obtained with a series of standardized NaHS solutions treated with aqua regia. The possibility that the solvent washing

removed of the adsorbed sulfur was excluded because the adsorbed sulfur quantified by digesting the solvent-washed NaHS-treated AuNP precipitates was statistically the same (within the detection error) as that by quantification of the sulfur species in the supernatant in the (AuNP/NaHS) samples.

4.3.5 Preparation of the ligand containing AuNP aggregates

As-synthesized AuNPs (2 mL) was mixed with equal volume of aqueous ligand solutions with a concentration of 50 μM for MBI, TG, and adenine and 100 μM for MBT, BDT, and ET. The amount of the ligands used are at least 2 times higher than their expected full monolayer packing capacity on AuNPs estimated on the reported packing density for MBI, and ET.[191] The ligand binding solution was vortex mixed for ~20 s and left overnight under the ambient conditions. The ligand adsorption all induced spontaneous AuNP aggregation and precipitation.

4.3.6 UV-vis and SERS detection of ligand desorption from AuNPs

The UV-vis quantification of ligand desorption was conducted only for MBI, TG, and adenine, the three UV-vis active ligands, while the SERS detection of the ligand desorption was performed for all ligands as they are SERS active. Before adding NaHS and ME as the displacing reagent, the ligand-containing AuNP aggregates were washed thoroughly with 18 MΩ-cm Nanopure water until no ligand was detectable in UV-vis spectra obtained with the supernatant of washed AuNP aggregates. The ligand displacement was conducted by added predefined concentrations of NaHS or ME into the washed ligand-containing AuNP aggregates. .

For SERS detection of ligand desorption, the washed ligand containing AuNP aggregates were mixed with NaHS or ME with pre-defined concentrations. The ligand displacement solution was then incubated overnight under ambient conditions before their SERS acquisition. The SERS

spectral integration time was varied from 10 to 200 s with 1-50 accumulations. SERS spectra were acquired using a ×10 objective and the laser power was 1.3 mW before objective.

4.3.7 Normal Raman and SERS spectra of NaHS and Na_2S

Raman spectrum of NaHS and Na_2S was acquired with their respective 2 M aqueous solution. Their SERS samples were prepared by overnight mixing 1 mL as-synthesized AuNPs with an equal volume of 0.1 M NaHS or Na_2S. The SERS spectra were acquired with the precipitated AuNP aggregates that were formed spontaneously after the NaHS addition.

4.4 Results and discussion

4.4.1 NaHS adsorption onto as-synthesized AuNPs

The threshold NaHS concentration for inducing AuNP aggregation and complete precipitation is 30 mM (Figure 4.2A). This is drastically higher than that of hydrophobic alkanethiols and ion-pairing formation electrolytes that induced AuNP at concentrations as low as 5 μM,[192-193] but comparable with common electrolyte that includes aggregation at 20 mM. This result indicates that the NaHS-induced AuNP aggregation is caused by the high concentration of free NaHS in solution, but not due to adsorbed polysulfur species on the gold surface. Otherwise, the threshold NaHS concentration must be below or close to 100 μM. This is because NaHS reaches approximately saturation adsorption on AuNPs in this concentration range as it will be shown later in this work.

The HS^- adsorption induces red-shift of the AuNP localized surface plasmonic resonance (LSPR) wavelength (Figure 4.2(D)), which is consistent with the AuNP LSPR variation induced by glutathione, thiolated polyethylene glycol, and protein.[182] However, instead of increasing the AuNP LSPR peak intensity as observed with those ligands, the NaHS adsorption reduces the AuNP

LSPR peak. Detailed reason for difference is currently unclear. However, the fact that NaHS induces significant AuNP LSPR change provides a simple way for one to probe the time- and concentration-dependent HS^- binding to AuNPs (Figure 4.2(B)-4.2(D)). The Figure 4.2(B) indicates that NaHS binding to AuNP is an extremely rapid process. The AuNP LSPR peak drops instantly (within the ~2 min of the deadline of our time-resolved UV-vis measurement) after the addition of NaHS, and then remain constant afterwards ((b) in Figure 4.2(B)). Indeed, the time-dependent spectra of the AuNP/NaHS sample overlapped near perfectly regardless the spectrum was taken 2 min or 24 h after the sample preparation. This data strongly suggests that the HS– binding occurred predominantly within the first few minutes of the sample mixing.

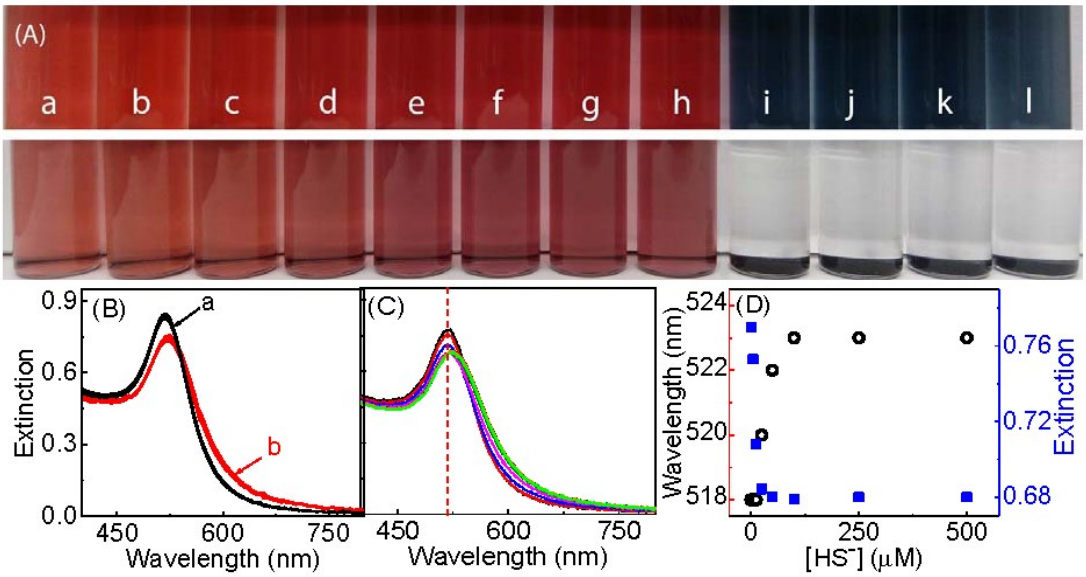

Figure 4.2 (A) Photographs of the as-synthesized AuNPs mixed with different concentrations of NaHS for (top) 5 min and (middle) 24 h. (B) Time-dependent UV–vis spectra of (a) AuNP/H_2O and (b) AuNP/NaHS taken at 2 min, 30 min, 1 h, 1.5 h, 2 h, 2.5 h, 3 h, 4 h, 5 h, 24 h, 48 h, and 170 h after the sample preparation. (C) NaHS concentration-dependent UV–vis spectra of the AuNP/NaHS mixtures. (D) AuNP LSPR peak wavelength (black) and intensity (blue) as a function of the NaHS concentration.

Note: The nominal NaHS concentrations of (a)-(l) in A are 0 μM, 3 μM, 7.5 μM, 15 μM, 30 μM, 60 μM, 300 μM, 15 mM, 30 mM, 60 mM 150 mM, and 300 mM respectively. The nominal AuNP concentration is 3.2 nM in all samples. The time-dependent spectra acquired are all nearly perfectly overlapped in both (a) AuNP/H2O and (b) AuNP/NaHS. The nominal AuNP and NaHS concentrations for sample (b) are 3.2 nM and 60 μM, respectively.

4.4.2 Empirical Langmuir binding constant and affinity

ICP-MS quantification of the sulfur adsorption onto AuNPs revealed that the NaHS binding to AuNPs empirically follows a Langmuir adsorption isotherm with a nominal binding constant of 5.5(±0.8) $\times 10^6$ M^{-1} and saturation packing density of 960±60 pmol/cm^2 (Figure 4.3). This is estimated by assuming the as-synthesized AuNPs are perfectly spherical and identical in sizes. Even with a large excess of NaHS, the amount of the sulfur adsorption remains constant

during the entire 7 days of sample incubation (Figure 4.4). This indicates that only monolayer sulfur species are adsorbed on AuNPs. Otherwise, the amount of sulfur adsorbed should monotonically increase with time. It is critical to note that even though HS^- is the predominate species in the as-prepared NaHS and Na_2S solution as predicted by their H_2S pK_a values, there are also small fractions of H_2S and S^{2-} in the solution. The experimental data in Figure 4.3for simplicity, referred to as the HS^- adsorption isotherm, but the actual sulfur species (H_2S, HS^-, and S^{2-}) responsible for the adsorbed sulfur is unclear. Time-dependent NaHS adsorption conducted with AuNPs mixed with large excess NaHS revealed that only a monolayer amount of the sulfur was adsorbed onto AuNPs during the entire 7 days experiment period in the AuNP/NaHS mixtures Figure 4.4. Consistent with time-dependent UV–vis spectra obtained with AuNP/mixture shown in Figure 4.2, this time-dependent NaHS adsorption data also indicate the sulfur adsorption is rapid process. This is because the amount of the sulfur adsorbed in day 1 is statistically identical to that in day 7 Figure 4.4. The fact that sulfur adopted only a monolayer adsorption indicates that all sulfur atoms, regardless if it is in monomeric or polymeric form, all directly lie on the AuNP surfaces. In other words, the S–S cross-linked sulfur oligomers or polymers are parallel to surface plane of the gold surface plane, but not pointing away from the AuNP surface like polymer brush. Otherwise, one would expect the saturation density of sulfur species will be significantly higher than the monolayer packing observed. Also, the amount of sulfur adsorbed would increase with increasing sample incubation for a long period of time during the 7 days sample incubation, but this was not seen.

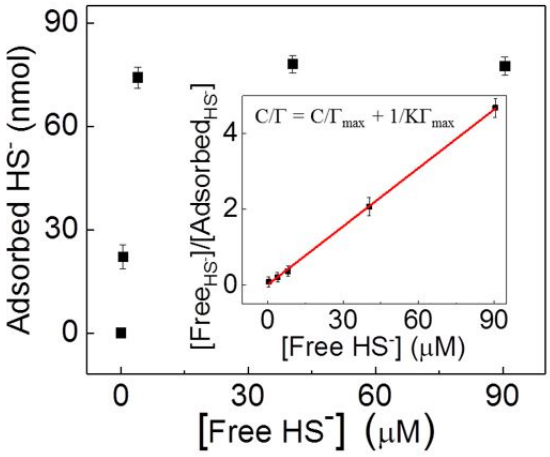

Figure 4.3 HS^- adsorption isotherm onto as-synthesized AuNPs. The inset gives is the Langmuir fitting of the adsorption isotherm.

Note: The terms in the equation are: C = concentration of free HS^- at equilibrium; K = binding constant of HS^- onto AuNPs; Γ = concentration of adsorbed HS^- ions onto AuNPs; Γ_{max} = concentration of adsorbed HS− ions at the maximum adsorption. The nominal AuNP concentration is 6.5 nM in all NaHS binding samples.

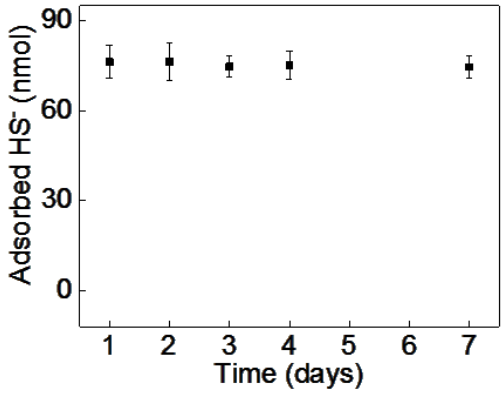

Figure 4.4 The adsorbed sulfur species as the function of the time.

Note: A volume of 2 mL of NaHS is added into an equal volume of the as-prepared AuNPs. The nominal AuNP and HS^- concentrations in the ligand binding solution are 6.5 nM and 300 μM, respectively.

4.4.3 Sulfur species of Na_2S and NaHS in solutions and adsorbed onto AuNPs

As predicted by the H_2S pK_a values, the main sulfur species in both Na_2S and NaHS solutions should be HS^- (Figure 4.5). Therefore, observations derived from NaHS should be directly applicable to that Na_2S, and vice versa. This conclusion is supported by the normal Raman and SERS spectra taken with Na_2S and NaHS solutions (Figure 4.5). There are similarly intense S-H Raman stretching peak at ~2600 cm^{-1} in the equally concentrated NaHS and Na_2S solution (Figure 4.5b), suggesting the HS^- concentration in the two solutions are similar. Furthermore, the total absence of S-H feature in their SERS spectra (Figure 4.5a) indicates that there is no significant SH^- species on the AuNP surface. Instead, there is strong S-Au (~250-260 cm^{-1})[194-196] and a strong S-S stretching (~450-460 cm^{-1})[194-198] feature appeared in both the normal Raman and SERS spectrum obtained with elemental sulfur powder have an intense peak in the 460 cm^{-1} region (Figure 4.5). Elemental sulfur is known for its S–S cross-linking bonds.[199] Since the sulfur powder used in our study is an analytical standard with a high purity (Sigma-Aldrich, Cat No. 7704-34-9), this prominent 460 cm^{-1} peak must be from the S–S stretching.

The SERS data in Figure 4.5 supports the conclusion by Salvarezza et al that sulfur adlayer comprises of monomeric and polymeric sulfur mixture,[187] but these data are at odds with the SERS spectra shown by Chen et al who observed only the presence of Au-S stretching feature with no S-S signal.[42] While the presence of the Au-S bond might be explained by the directly S^{2-} adsorption onto AuNP, or by the further HS^- ionization on the AuNP surfaces, the observation of polysulfur species implies that there must be a charge neutralization reactions occurring when S^{2-} or SH^- is adsorbed onto the AuNP surfaces. This charge neutralization reaction is likely driven by the electrostatic repulsion by the S^{2-} and HS^- ion accumulated onto the AuNP surfaces. This

mechanism has been proposed to explain the S-S crossing-linking among alkanedithiolate is packed onto AuNP surfaces.

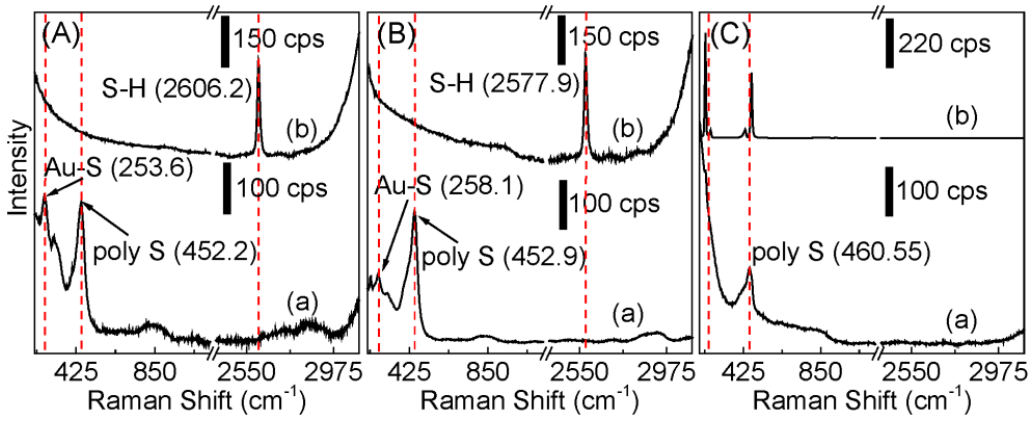

Figure 4.5 (a) SERS and (b) normal Raman spectra of (A) Na_2S, (B) NaHS, and (C) elemental sulfur.

Note: The nominal concentration of AuNPs, Na_2S, and NaHS in the SERS samples are 6.5 nM, 2 M, and 2 M, respectively. For the SERS spectrum of elemental sulfur, a saturated solution of elemental sulfur in ethanol was mixed with AuNPs. The normal Raman spectra of Na_2S and NaHS were acquired with this 2 M aqueous solution, but that of elemental sulfur was with the solid.

4.4.4 NaHS- and ME-induced displacement of TG, MBI, and adenine from AuNPs

MBI, TG, and adenine adsorption induces spontaneous AuNP aggregations, and complete AuNP precipitation after overnight sample incubation. The amount of the ligand adsorbed onto the AuNPs were determined by UV-vis quantification of the ligand remaining free in the supernatant in the AuNP/ligand adsorption solutions (Figure 4.6). The NaHS- and ME-induced ligand desorption was studied with both UV-vis quantification of the ligand released to the centrifugation supernatant in the ligand displacement solution, while SERS monitors the ligand remain adsorbed

onto the AuNP surfaces. Since neither NaHS or ME is UV-vis active, the UV-vis measurement provides a convenience way for quantifying these ligand displacements.

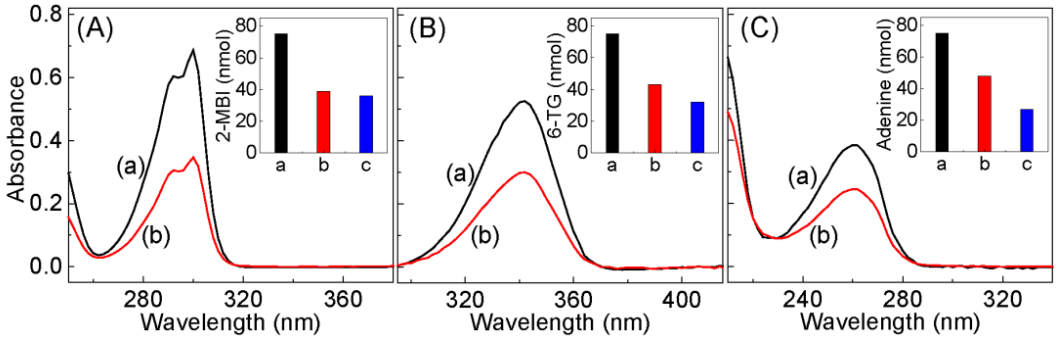

Figure 4.6 UV-vis quantification of the (A) MBI, (B) TG, and (C) adenine adsorbed onto AuNPs.

Note: (a) is UV-vis spectrum of the ligand control, (b) is obtained with the supernatant of the overnight incubated ligand/AuNP mixture which prepared by mixing 1.5 mL of as-synthesized AuNPs with equal volume of 50 μM of ligand. Inset shows the amount of ligand (a) added to AuNPs, (b) free in solution after adsorbing onto AuNPs, and (c) adsorbed onto the AuNPs. The nominal concentration of as-synthesized AuNPs is ~ 6.5 nM.

Before addition of NaHS or ME, the SERS spectra of the AuNP/ligand samples (Spectra (a) in Figure 4.7) are the same as that reported in the literature for the individual ligands.[200-201] In the (AuNP/ligand)/NaHS and (AuNP/ligand)/ME samples where NaHS and ME are the incoming ligands, the relative SERS intensity between the initial and incoming ligand decreases with increasing concentrations of the incoming ligand (2nd and 4th columns, Figure 4.7) . This result indicates that ligand released to the supernatant of the ligand displacement solution is caused by NaHS or ME displacing of the initial ligand.

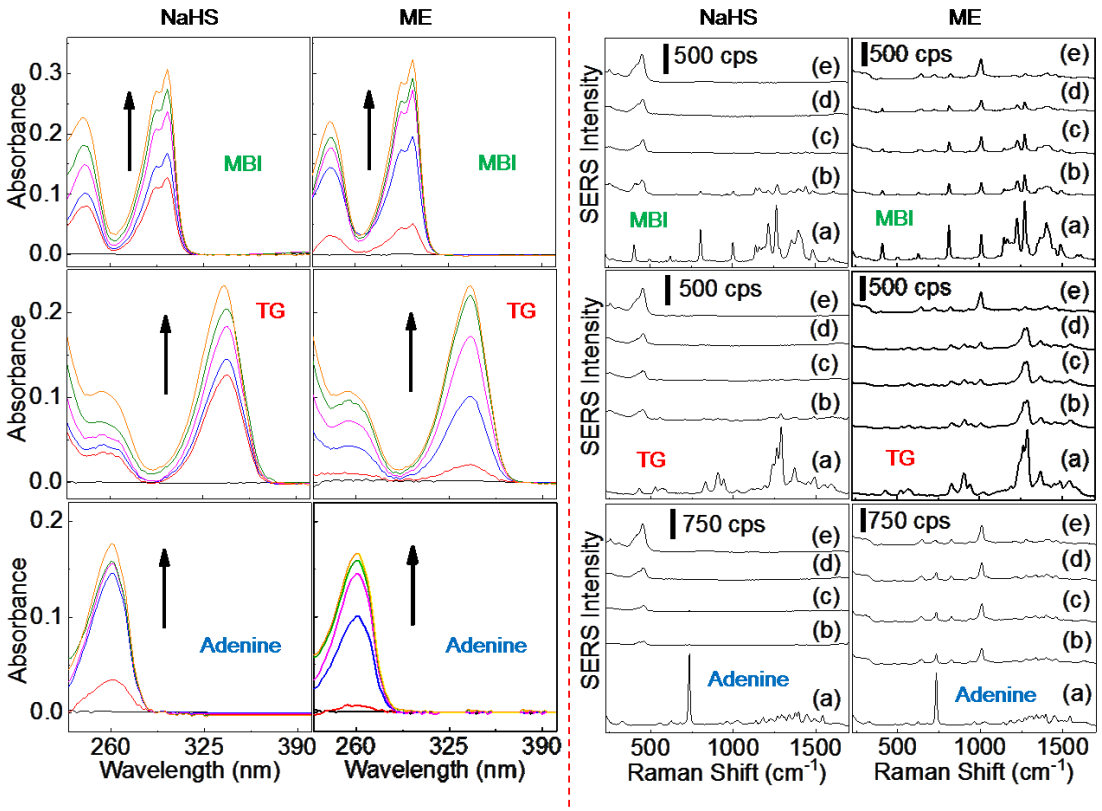

Figure 4.7 (top) MBI, (middle) TG, and (bottom) adenine displacement from AuNPs by NaHS and ME as the incoming ligands. (first and second columns) UV−vis quantification of the ligands displaced after the overnight incubation by NaHS and ME of different concentrations. (third and fourth columns) SERS spectra obtained after overnight incubation of the ligand containing AuNPs aggregates with NaHS or ME of different concentrations.

Note: The NaHS concentrations in ligand displacement samples (a) to (d) are 0, 30, 60, and 105 μM, respectively. The ME concentrations in those samples are 0, 50, 100, and 175 μM, respectively. The excess ligand in these samples was removed before the NaHS and ME addition. SERS spectra (e) were obtained with the NaHS or ME controls that were prepared by mixing equal volume of as-prepared AuNPs with 200 μM NaHS or ME.

NaHS induced a complete desorption of TG, MBI, and adenine from aggregated AuNPs when the NaHS nominal concentration is 105 μM. This conclusion is drawn from both the UV-vis and SERS spectra with the ligand displacement samples ((AuNP/ligand)/NaHS) (Figure 4.7, 1st and 3rd columns). Time-dependent SERS spectra obtained with the ligand displacement solution

reveals that ligand SERS signal disappeared completely within the first 20 min of the addition of the 105 μM HS^- (Figure 4.8).

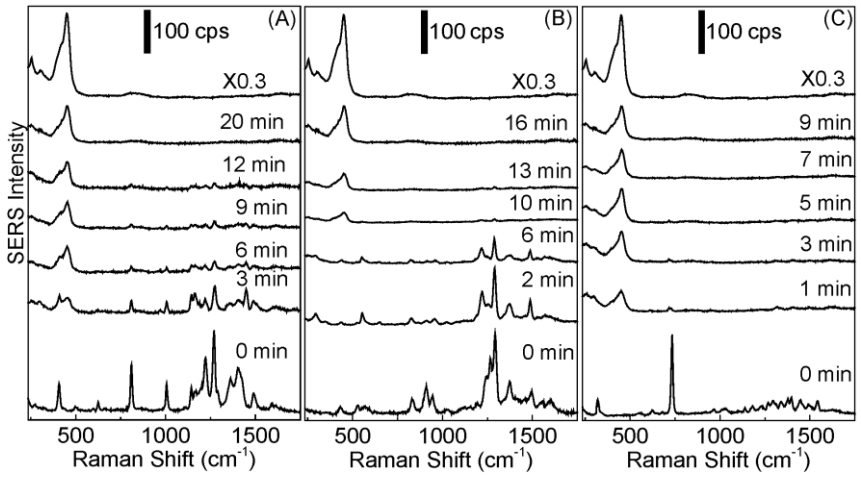

Figure 4.8 Time-dependent SERS study of NaHS-induced ligand displacement for (A) MBI, (B) TG, and (C) adenine.

Note: The SERS spectra at the bottom and top were acquired with the ligand and NaHS control, respectively. The ligand-functionalized AuNPs prepared by mixing 1 mL of as-synthesized AuNPs with equal volume of 50 μM ligand, followed by overnight incubation. The aggregated ligand-containing AuNP precipiates were extensively washed with Nanopure water before their SERS acquisition for the ligand control and the addition of NaHS for the time-dependent ligand displacement study. The nominal NaHS and AuNP concentrations in the (AuNP/NaHS) sample are 50 mM and 6.5 nM, respectively. Time-dependent SERS spectra were obtained after adding 175 μM of NaHS into the ligand-functionalized AuNPs. The time elapsed between the NaHS addition and individual SERS spectral acquisition was specified in the figure.

While UV-vis spectra obtained with the supernatant of (AuNP/MBI)/ME, (AuNP/TG)/ME, and (AuNP/adenine)/ME indicates a complete ligand displacement, but there are still detectable SERS features of the initial ligands in all (AuNP/ligand)/ME samples (Figure 4.7, 4th column). This result indicates that there is a small fraction of surface bound MBI, TG, and adenine have

remained on the AuNP surfaces and were not displaced by ME. Since the UV-vis indicate a complete ligand displacement, the fraction of the ligands remains on the AuNP must be very small.

Comparison of the SERS and UV-vis data obtained with the (AuNP/ligand)/ME samples highlights the complementary nature of these two measurement techniques. UV-vis measurement is reliable for deduce the amount of the displaced ligands but it is ineffective to detect the minuscule amount of ligands in the junctions in the aggregated AuNPs. In contrast, SERS signal is dominated by the ligands located in the NP junction, the region most resistant to the ligand displacement but with disproportionally high SERS activities.[173, 202-205] As a result, SERS is an excellent technique for critically evaluation of the "completeness" of ligand desorption. Indeed, the adenine, MBI, and TG SERS feature in the (AuNP/ligand)/ME samples are due most likely to a trace of the ligand remaining adsorbed in the junction area of the aggregated AuNPs. This is because the UV-vis shows essentially all those ligands are displaced by ME (3rd column, Figure 4.7). Nonetheless, the SERS measurement clearly demonstrates that that only NaHS, but not ME, can completely remove ligands from the AuNP surfaces. This includes adenine that can bind only nonspecifically to AuNPs.

UV-vis spectra of the ligands displaced by NaHS and ME are identical to UV-vis spectra acquired with the as-prepared ligand solution, indicating the both these ligand displacement reactions is nondestructive to the initial ligands. This is in sharp contrast to the ligand displacement observed with KI and $NaBH_4$ in which UV-vis spectra of the displaced MBI and TG is drastically modified due to their desulfurization induced by $NaBH_4$, and the I_2 oxidation in the KI-induced ligand displacement.

The fact that ME inducing almost complete adenine displacement is in sharp contrast to the relatively poor adenine displacement by glutanthione, a tripeptide as the incoming ligands. [182]

Both ME and glutathione are aliphatic thiols. Thereby they should have a similar binding affinity to AuNPs. However, only less than 70% of adenine can be displaced from the aggregated AuNPs by glutathione regardless of the concentration of the latter.[182] Since glutathione, ME, and HS– have progressively smaller molecular dimensions, while their effectiveness for ligand displacement increases, this indicates smaller incoming ligands are more effective at inducing complete ligand displacement. Indeed, HS– is to our knowledge, the only incoming ligand can induce complete and nondestructive ligand desorption from aggregated AuNPs.

4.4.5 NaHS-induced displacement of ET, MBT, and BDT from AuNPs.

NaHS is also capable of displacing alkanethiols, aromatic monothiols, and aromatic dithiols (Figure 6). This conclusion is derived based on the SERS spectra obtained for overnight incubated (AuNP/ET)/NaHS, (AuNP/ MBT)/NaHS, and (AuNP/BDT)/ NaHS samples (Figure 4.9). Because of the poor UV-vis activity of this subset model organothiols, only SERS measurements are used for detecting the ET, MBT, and BDT displacement. The threshold NaHS concentration for complete removal of ET, MBT, and BDT is somewhere below 60 μM, 6 mM, and 60 mM, respectively. This conclusion is drawn from the SERS spectra acquired with (AuNP/ligand)/NaHS samples. The SERS spectra of the (AuNP/ligand) samples treated with NaHS at these concentrations are totally dominated by the sulfur species originating from HS– binding to AuNPs. There were no detectable SERS features from the initial organothiols in those spectra.

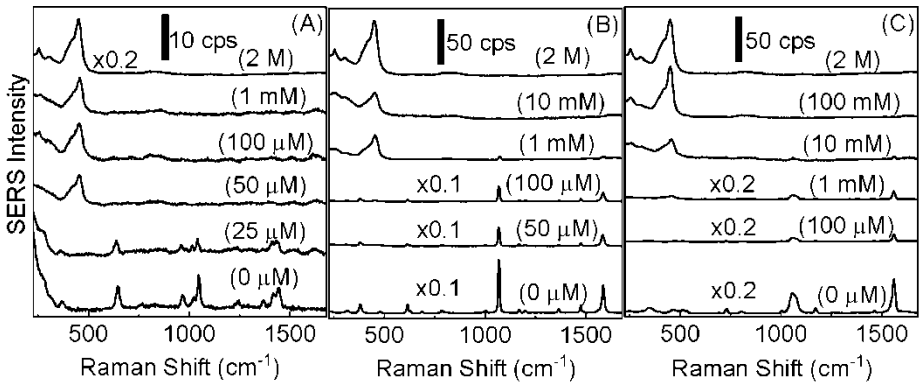

Figure 4.9 (A) ET, (B) MBT, and (C) BDT displacement from AuNP by NaHS.

Note: The bottom spectrum is obtained with the ligand/AuNP control with no NaHS addition, and the top spectrum is for NaHS control (AuNP/NaHS). NaHS concentrations used are shown in the SERS spectra obtained with the ligand displacement samples (a–d).

Notably, the degree of the organothiol resistance to the HS^--induced displacement correlates strongly to the organothiol acidities, i.e, the thiol pK_a values. BDT and MBT, the two aromatic thiols are the most resistant to the ligand displacement, followed by aliphatic thiol ET, and then the thioamide MBI and TG. This is inversely proportional to the thiol pK_a values. Aromatic thiols have the lowest pK_a and it usually in the range from 6.0 and 7.0 ,[206-207]. While, aliphatic thiol pK_as occur from 8.0 to 10.0, [206, 208-210]. The thiol tautomer of MBI ionizes at pKa ~10.3.[200] Assuming that all thiolates have the same reaction free energy for binding to AuNPs, the smaller the pK_a value is (i.e., the stronger its acidity), the more thermodynamically favorable the organothiol's binding to AuNP surfaces becomes. This enhances the organothiol resistance to the ligand displacement.

4.5 Conclusions

Using a combination of UV–vis, surface-enhanced Raman spectroscopy, and ICP-MS, we have conducted a quantitative study of the HS^- adsorption and HS^--induced ligand displacement on AuNPs. HS^- is adsorbed as a monolayer on AuNP that contains both S–Au bonds and S–S bonds, but with no detectable S–H features. The observed disulfide linkages within the monolayer adsorbed sulfur species provides direct evidence that the disulfide bond can remain intact on AuNP surface. Mechanistically, the disulfide bond formation on AuNPs is likely driven by the electrostatic repulsions among the adsorbed sulfide (S^{2-}) or hydrogen sulfide (HS^-) ions. The fact that only HS^- but not ME or glutathione can induce complete ligand displacement from the aggregated AuNPs highlights the significant size effect of the incoming ligands. The successful identification of NaHS as an effective ligand for complete nondestructive ligand displacement from AuNP should open the door for developing AuNP-based capture-and-release biomolecule enrichment methods.

REFERENCES

1. Ahl, S.; Cameron, P. J.; Liu, J.; Knoll, W.; Erlebacher, J.; Yu, F., A Comparative Plasmonic Study of Nanoporous and Evaporated Gold Films. *Plasmonics* **2008**, *3*, 13-20.

2. Nogues, C.; Wanunu, M., A Rapid Approach to Reproducible, Atomically Flat Gold Films on Mica. *Surf. Sci.* **2004**, *573*, L383-L389.

3. Torop, J.; Sugino, T.; Asaka, K.; Jänes, A.; Lust, E.; Aabloo, A., Nanoporous Carbide-Derived Carbon Based Actuators Modified with Gold Foil: Prospect for Fast Response and Low Voltage Applications. *Sens. Act. B: Chem.* **2012**, *161*, 629-634.

4. Anker, J. N.; Hall, W. P.; Lyandres, O.; Shah, N. C.; Zhao, J.; Van Duyne, R. P., Biosensing with Plasmonic Nanosensors. *Nat.Mater.* **2008**, *7*, 442-453.

5. El-Sayed, I. H.; Huang, X.; El-Sayed, M. A., Selective Laser Photo-Thermal Therapy of Epithelial Carcinoma Using Anti-Egfr Antibody Conjugated Gold Nanoparticles. *Cancer.Lett.***2006**, *239*, 129-135.

6. Ghosh, P. S.; Kim, C.-K.; Han, G.; Forbes, N. S.; Rotello, V. M., Efficient Gene Delivery Vectors by Tuning the Surface Charge Density of Amino Acid-Functionalized Gold Nanoparticles. *ACS Nano* **2008**, *2*, 2213-2218.

7. Brown, S. D.; Nativo, P.; Smith, J.-A.; Stirling, D.; Edwards, P. R.; Venugopal, B.; Flint, D. J.; Plumb, J. A.; Graham, D.; Wheate, N. J., Gold Nanoparticles for the Improved Anticancer Drug Delivery of the Active Component of Oxaliplatin. *J. Am. Chem. Soc.* **2010**, *132*, 4678-4684.

8. Ansar, S. M.; Haputhanthri, R.; Edmonds, B.; Liu, D.; Yu, L.; Sygula, A.; Zhang, D., Determination of the Binding Affinity, Packing, and Conformation of Thiolate and Thione Ligands on Gold Nanoparticles. *J. Phys. Chem. C* **2011**, *115*, 653-660.

9. Athukorale, S.; De Silva, M.; LaCour, A.; Perera, G. S.; Pittman, C. U.; Zhang, D., Nahs Induces Complete Nondestructive Ligand Displacement from Aggregated Gold Nanoparticles. *J. Phys. Chem. C* **2018**, *122*, 2137-2144.

10. Zhou, X.; Xu, W.; Liu, G.; Panda, D.; Chen, P., Size-Dependent Catalytic Activity and Dynamics of Gold Nanoparticles at the Single-Molecule Level. *J. Am. Chem. Soc.* **2010**, *132*, 138-146.

11. Homberger, M.; Simon, U., On the Application Potential of Gold Nanoparticles in Nanoelectronics and Biomedicine. *Phil. Trans. R. Soc. A* **2010**, *368*, 1405.

12. Eustis, S.; El-Sayed, M. A., Why Gold Nanoparticles Are More Precious Than Pretty Gold: Noble Metal Surface Plasmon Resonance and Its Enhancement of the Radiative and Nonradiative Properties of Nanocrystals of Different Shapes. *Chem. Soc. Rev.* **2006**, *35*, 209-217.

13. Turkevich, J.; Stevenson, P. C.; Hillier, J., A Study of the Nucleation and Growth Processes in the Synthesis of Colloidal Gold. *Discuss. Faraday Soc.***1951**, *11*, 55-75.

14. Verwey, E. J. W., Theory of the Stability of Lyophobic Colloids.*J. Phys. Chem. C* **1947**, *51*, 631-636.

15. Frens, G., Controlled Nucleation for the Regulation of the Particle Size in Monodisperse Gold Suspensions. *Nat. Phys. Sci.* **1973**, *241*, 20-22.

16. Brust, M.; Walker, M.; Bethell, D.; Schiffrin, D. J.; Whyman, R., Synthesis of Thiol-Derivatised Gold Nanoparticles in a Two-Phase Liquid–Liquid System. *J. Am. Chem. Soc., Chem. Commun.***1994**, 801-802.

17. Eustis, S.; El-Sayed, M. A., Why Gold Nanoparticles Are More Precious Than Pretty Gold: Noble Metal Surface Plasmon Resonance and Its Enhancement of the Radiative and Nonradiative Properties of Nanocrystals of Different Shapes. *Chem. Soc. Rev.* **2006**, *35*, 209-217.

18. Daniel, M.-C.; Astruc, D., Gold Nanoparticles: Assembly, Supramolecular Chemistry, Quantum-Size-Related Properties, and Applications toward Biology, Catalysis, and Nanotechnology. *Chem. Rev.* **2004**, *104*, 293-346.

19. Dykman, L.; Khlebtsov, N., Gold Nanoparticles in Biomedical Applications: Recent Advances and Perspectives. *Chem. Soc. Rev.* **2012**, *41*, 2256-2282.

20. Perera, G. S.; LaCour, A.; Zhou, Y.; Henderson, K. L.; Zou, S.; Perez, F.; Emerson, J. P.; Zhang, D., Iodide-Induced Organothiol Desorption and Photochemical Reaction, Gold Nanoparticle (Aunp) Fusion, and Sers Signal Reduction in Organothiol-Containing Aunp Aggregates. *J. Phys. Chem. C* **2015**, *119*, 4261-4267.

21. Millstone, J. E.; Wei, W.; Jones, M. R.; Yoo, H.; Mirkin, C. A., Iodide Ions Control Seed-Mediated Growth of Anisotropic Gold Nanoparticles. *Nano Lett.* **2008**, *8*, 2526-2529.

22. Häkkinen, H., The Gold-Sulfur Interface at the Nanoscale. *Nature Chem.* **2012**, *4*, 443-455.

23. Wang, D.; Tejerina, B.; Lagzi, I.; Kowalczyk, B.; Grzybowski, B. A., Bridging Interactions and Selective Nanoparticle Aggregation Mediated by Monovalent Cations. *ACS Nano* **2010**, *5*, 530-536.

24. Weisbecker, C. S.; Merritt, M. V.; Whitesides, G. M., Molecular Self-Assembly of Aliphatic Thiols on Gold Colloids. *Langmuir* **1996**, *12*, 3763-3772.

25. Love, J. C.; Estroff, L. A.; Kriebel, J. K.; Nuzzo, R. G.; Whitesides, G. M., Self-Assembled Monolayers of Thiolates on Metals as a Form of Nanotechnology. *Chem. Rev.* **2005**, *105*, 1103-1170.

26. Pensa, E.; Cortés, E.; Corthey, G.; Carro, P.; Vericat, C.; Fonticelli, M. H.; Benítez, G.; Rubert, A. A.; Salvarezza, R. C., The Chemistry of the Sulfur–Gold Interface: In Search of a Unified Model. *Acc. Chem. Res.* **2012**, *45*, 1183-1192.

27. Love, J. C.; Estroff, L. A.; Kriebel, J. K.; Nuzzo, R. G.; Whitesides, G. M., Self-Assembled Monolayers of Thiolates on Metals as a Form of Nanotechnology. *Chem. Rev.* **2005**, *105*, 1103-1170.

28. Saha, K.; Agasti, S. S.; Kim, C.; Li, X.; Rotello, V. M., Gold Nanoparticles in Chemical and Biological Sensing. *Chem. Rev.* **2012**, *112*, 2739-2779.

29. Erwin, W. R.; Zarick, H. F.; Talbert, E. M.; Bardhan, R., Light Trapping in Mesoporous Solar Cells with Plasmonic Nanostructures. *Energy Environ. Sci.* **2016**, *9*, 1577-1601.

30. Vangala, K.; Ameer, F.; Salomon, G.; Le, V.; Lewis, E.; Yu, L.; Liu, D.; Zhang, D., Studying Protein and Gold Nanoparticle Interaction Using Organothiols as Molecular Probes. *J. Phys. Chem. C* **2012**, *116*, 3645-3652.

31. Kundu, J.; Neumann, O.; Janesko, B. G.; Zhang, D.; Lal, S.; Barhoumi, A.; Scuseria, G. E.; Halas, N. J., Adenine− and Adenosine Monophosphate (Amp)−Gold Binding Interactions Studied by Surface-Enhanced Raman and Infrared Spectroscopies. *J. Phys. Chem. C* **2009**, *113*, 14390-14397.

32. Lin, S.-Y.; Tsai, Y.-T.; Chen, C.-C.; Lin, C.-M.; Chen, C.-h., Two-Step Functionalization of Neutral and Positively Charged Thiols onto Citrate-Stabilized Au Nanoparticles. *J. Phys. Chem. B* **2004**, *108*, 2134-2139.

33. Wang, G.; Sun, W., Optical Limiting of Gold Nanoparticle Aggregates Induced by Electrolytes. *J. Phys. Chem. B* **2006**, *110*, 20901-20905.

34. Millstone, J. E.; Wei, W.; Jones, M. R.; Yoo, H.; Mirkin, C. A., Iodide Ions Control Seed-Mediated Growth of Anisotropic Gold Nanoparticles. *Nano Lett.* **2008**, *8*, 2526-2529.

35. Rai, A.; Singh, A.; Ahmad, A.; Sastry, M., Role of Halide Ions and Temperature on the Morphology of Biologically Synthesized Gold Nanotriangles. *Langmuir* **2006**, *22*, 736-741.

36. DuChene, J. S.; Niu, W.; Abendroth, J. M.; Sun, Q.; Zhao, W.; Huo, F.; Wei, W. D., Halide Anions as Shape-Directing Agents for Obtaining High-Quality Anisotropic Gold Nanostructures. *Chem. Mater.* **2013**, *25*, 1392-1399.

37. Liu, Y.; Liu, L.; Guo, R., Br−-Induced Facile Fabrication of Spongelike Gold/Amino Acid Nanocomposites and Their Applications in Surface-Enhanced Raman Scattering. *Langmuir* **2010**, *26*, 13479-13485.

38. Daniel, W. L.; Han, M. S.; Lee, J.-S.; Mirkin, C. A., Colorimetric Nitrite and Nitrate Detection with Gold Nanoparticle Probes and Kinetic End Points. *J. Am. Chem. Soc.* **2009**, *131*, 6362-6363.

39. Zhang, Z.; Wu, Y., Nabh4-Induced Assembly of Immobilized Au Nanoparticles into Chainlike Structures on a Chemically Modified Glass Surface. *Langmuir* **2011**, *27*, 9834-9842.

40. Ansar, S. M.; Ameer, F. S.; Hu, W.; Zou, S.; Pittman, C. U.; Zhang, D., Removal of Molecular Adsorbates on Gold Nanoparticles Using Sodium Borohydride in Water. *Nano Lett.***2013**, *13*, 1226-1229.

41. Ansar, S. M.; Perera, G. S.; Ameer, F. S.; Zou, S.; Pittman, C. U.; Zhang, D., Desulfurization of Mercaptobenzimidazole and Thioguanine on Gold Nanoparticles Using Sodium Borohydride in Water at Room Temperature. *The J. Phys. Chem. C* **2013**, *117*, 13722-13729.

42. Zhang, Z.; Chen, Z.; Wang, S.; Qu, C.; Chen, L., On-Site Visual Detection of Hydrogen Sulfide in Air Based on Enhancing the Stability of Gold Nanoparticles. *ACS Appl. Mater. Interfaces* **2014**, *6*, 6300-6307.

43. Ha, T. H.; Koo, H.-J.; Chung, B. H., Shape-Controlled Syntheses of Gold Nanoprisms and Nanorods Influenced by Specific Adsorption of Halide Ions. *J. Phys. Chem. C* **2007**, *111*, 1123-1130.

44. Pezzato, C.; Maiti, S.; Chen, J.-Y.; Cazzolaro, A.; Gobbo, C.; Prins, L., Monolayer Protected Gold Nanoparticles with Metal-Ion Binding Sites: Functional Systems for Chemosensing Applications. *Chem. Commun.* **2015**, *51*, 9922-9931.

45. Poornima, V.; Alexandar, V.; Iswariya, S.; Perumal, P. T.; Uma, T. S., Gold Nanoparticle-Based Nanosystems for the Colorimetric Detection of Hg2+ Ion Contamination in the Environment. *RSC Adv.* **2016**, *6*, 46711-46722.

46. Lin, Y.-W.; Huang, C.-C.; Chang, H.-T., Gold Nanoparticle Probes for the Detection of Mercury, Lead and Copper Ions. *Analyst* **2011**, *136*, 863-871.

47. Kim, Y.; Johnson, R. C.; Hupp, J. T., Gold Nanoparticle-Based Sensing of "Spectroscopically Silent" Heavy Metal Ions. *Nano Lett.* **2001**, *1*, 165-167.

48. Leng, Y.; Li, Y.; Gong, A.; Shen, Z.; Chen, L.; Wu, A., Colorimetric Response of Dithizone Product and Hexadecyl Trimethyl Ammonium Bromide Modified Gold Nanoparticle Dispersion to 10 Types of Heavy Metal Ions: Understanding the Involved Molecules from Experiment to Simulation. *Langmuir* **2013**, *29*, 7591-7599.

49. Chen, G.-H.; Chen, W.-Y.; Yen, Y.-C.; Wang, C.-W.; Chang, H.-T.; Chen, C.-F., Detection of Mercury(Ii) Ions Using Colorimetric Gold Nanoparticles on Paper-Based Analytical Devices. *Anal. Chem.* **2014**, *86*, 6843-6849.

50. Hung, Y.-L.; Hsiung, T.-M.; Chen, Y.-Y.; Huang, Y.-F.; Huang, C.-C., Colorimetric Detection of Heavy Metal Ions Using Label-Free Gold Nanoparticles and Alkanethiols. *J. Phys. Chem. C* **2010**, *114*, 16329-16334.

51. Wu, S.-P.; Chen, Y.-P.; Sung, Y.-M., Colorimetric Detection of Fe 3+ Ions Using Pyrophosphate Functionalized Gold Nanoparticles. *Analyst* **2011**, *136*, 1887-1891.

52. Zhang, X.; Kong, X.; Fan, W.; Du, X., Iminodiacetic Acid-Functionalized Gold Nanoparticles for Optical Sensing of Myoglobin Via Cu2+ Coordination. *Langmuir* **2011**, *27*, 6504-6510.

53. Freeman, R. G.; Hommer, M. B.; Grabar, K. C.; Jackson, M. A.; Natan, M. J., Ag-Clad Au Nanoparticles: Novel Aggregation, Optical, and Surface-Enhanced Raman Scattering Properties. *J. Phys. Chem. C* **1996**, *100*, 718-724.

54. Choi, J.-P.; Fields-Zinna, C. A.; Stiles, R. L.; Balasubramanian, R.; Douglas, A. D.; Crowe, M. C.; Murray, R. W., Reactivity of [Au25(Sch2ch2ph)18]1− Nanoparticles with Metal Ions. *J. Phys. Chem. C* **2010**, *114*, 15890-15896.

55. Love, J. C.; Estroff, L. A.; Kriebel, J. K.; Nuzzo, R. G.; Whitesides, G. M., Self-Assembled Monolayers of Thiolates on Metals as a Form of Nanotechnology. *Chem. Rev.* **2005**, *105*, 1103-1170.

56. Kelly, K. L.; Coronado, E.; Zhao, L. L.; Schatz, G. C., The Optical Properties of Metal Nanoparticles: The Influence of Size, Shape, and Dielectric Environment. *J. Phys. Chem. B* **2003**, *107*, 668-677.

57. Miller, M. M.; Lazarides, A. A., Sensitivity of Metal Nanoparticle Surface Plasmon Resonance to the Dielectric Environment. *J. Phys. Chem.B* **2005**, *109*, 21556-21565.

58. Willets, K. A.; Duyne, R. P. V., Localized Surface Plasmon Resonance Spectroscopy and Sensing. *Annu. Rev. Phys. Chem.* **2007**, *58*, 267-297.

59. Saha, K.; Agasti, S. S.; Kim, C.; Li, X.; Rotello, V. M., Gold Nanoparticles in Chemical and Biological Sensing. *Chem. Rev.***2012**, *112*, 2739-2779.

60. Siriwardana, K.; Vithanage, B. C. N.; Zou, S.; Zhang, D., Quantification of the Depolarization and Anisotropy of Fluorophore Stokes-Shifted Fluorescence, on-Resonance Fluorescence, and Rayleigh Scattering. *Anal.Chem.* **2017**, *89*, 6686-6694.

61. Athukorale, S.; Leng, X.; Xu, J. X.; Perera, Y. R.; Fitzkee, N. C.; Zhang, D., Surface Plasmon Resonance, Formation Mechanism, and Surface Enhanced Raman Spectroscopy of Ag+-Stained Gold Nanoparticles. F*ront. Chem.* **2019**, *7*.

62. Cheng, W.; Dong, S.; Wang, E., Iodine-Induced Gold-Nanoparticle Fusion/Fragmentation/Aggregation and Iodine-Linked Nanostructured Assemblies on a Glass Substrate. *Angew. Chem.Int.Ed.* **2003**, *42*, 449-452.

63. Zhang, Z.; Li, H.; Zhang, F.; Wu, Y.; Guo, Z.; Zhou, L.; Li, J., Investigation of Halide-Induced Aggregation of Au Nanoparticles into Spongelike Gold. *Langmuir* **2014**, *30*, 2648-2659.

64. Zheng, T.; Bott, S.; Huo, Q., Techniques for Accurate Sizing of Gold Nanoparticles Using Dynamic Light Scattering with Particular Application to Chemical and Biological Sensing Based on Aggregate Formation. *ACS Appl. Mater. Interfaces* **2016**, *8*, 21585-21594.

65. Doane, T. L.; Chuang, C.-H.; Hill, R. J.; Burda, C., Nanoparticle Z -Potentials. *Acc. Chem. Res.* **2012**, *45*, 317-326.

66. Badia, A.; Cuccia, L.; Demers, L.; Morin, F.; Lennox, R. B., Structure and Dynamics in Alkanethiolate Monolayers Self-Assembled on Gold Nanoparticles: A Dsc, Ft-Ir, and Deuterium Nmr Study. *J. Am. Chem. Soc.***1997**, *119*, 2682-2692.

67. Aryal, S.; B.K.C, R.; Dharmaraj, N.; Bhattarai, N.; Kim, C. H.; Kim, H. Y., Spectroscopic Identification of Sau Interaction in Cysteine Capped Gold Nanoparticles. *Spectrochim .Acta .A Mol .Biomol. Spectrosc .***2006**, *63*, 160-163.

68. Hasan, M.; Bethell, D.; Brust, M., The Fate of Sulfur-Bound Hydrogen on Formation of Self-Assembled Thiol Monolayers on Gold: 1h Nmr Spectroscopic Evidence from Solutions of Gold Clusters. *J. Am. Chem. Soc.***2002**, *124*, 1132-1133.

69. Smith, A. M.; Marbella, L. E.; Johnston, K. A.; Hartmann, M. J.; Crawford, S. E.; Kozycz, L. M.; Seferos, D. S.; Millstone, J. E., Quantitative Analysis of Thiolated Ligand Exchange on Gold Nanoparticles Monitored by 1h Nmr Spectroscopy. *Anal. Chem.***2015**, *87*, 2771-2778.

70. Wang, M.; Zhang, Z.; He, J., A Sers Study on the Assembly Behavior of Gold Nanoparticles at the Oil/Water Interface. *Langmuir* **2015**, *31*, 12911-12919.

71. Tong, L.; Zhu, T.; Liu, Z., Approaching the Electromagnetic Mechanism of Surface-Enhanced Raman Scattering: From Self-Assembled Arrays to Individual Gold Nanoparticles. *Chem. Soc. Rev* **2011**, *40*, 1296-1304.

72. Nie, S.; Emory, S. R., Probing Single Molecules and Single Nanoparticles by Surface-Enhanced Raman Scattering. *Science* **1997**, *275*, 1102-1106.

73. Kleinman, S. L.; Ringe, E.; Valley, N.; Wustholz, K. L.; Phillips, E.; Scheidt, K. A.; Schatz, G. C.; Van Duyne, R. P., Single-Molecule Surface-Enhanced Raman Spectroscopy of Crystal Violet Isotopologues: Theory and Experiment. *J. Am. Chem. Soc.***2011**, *133*, 4115-4122.

74. Kneipp, K.; Kneipp, H.; Itzkan, I.; Dasari, R. R.; Feld, M. S., Surface-Enhanced Raman Scattering: A New Tool for Biomedical Spectroscopy. *Curr. Sci.* **1999**, *77*, 915-924.

75. Pilot, R.; Signorini, R.; Durante, C.; Orian, L.; Bhamidipati, M.; Fabris, L., A Review on Surface-Enhanced Raman Scattering. *Biosensors (Basel)* **2019**, *9*, 57.

76. Campion, A.; Kambhampati, P., Surface-Enhanced Raman Scattering. *Chem. Soc. Revs* **1998**, *27*, 241-250.

77. Greczynski, G.; Hultman, L., X-Ray Photoelectron Spectroscopy: Towards Reliable Binding Energy Referencing. *Prog. Mater. Sci.* **2020**, *107*, 100591.

78. Fadley, C. S., X-Ray Photoelectron Spectroscopy: Progress and Perspectives. *J. Electron Spectrosc.* **2010**, *178-179*, 2-32.

79. Konno, H., Chapter 8 - X-Ray Photoelectron Spectroscopy. In *Mater. Sci. Eng. C* Inagaki, M.; Kang, F., Eds. Butterworth-Heinemann: 2016; pp 153-171.

80. Crooks, R. M.; Zhao, M.; Sun, L.; Chechik, V.; Yeung, L. K., Dendrimer-Encapsulated Metal Nanoparticles: Synthesis, Characterization, and Applications to Catalysis. *Acc. Chem. Res.* **2001**, *34*, 181-190.

81. Laurent, S.; Forge, D.; Port, M.; Roch, A.; Robic, C.; Vander Elst, L.; Muller, R. N., Magnetic Iron Oxide Nanoparticles: Synthesis, Stabilization, Vectorization, Physicochemical Characterizations, and Biological Applications. *Chem. Rev.* **2008**, *108*, 2064-2110.

82. Gong, Z., et al., Structural Variation in Surface-Supported Synthesis by Adjusting the Stoichiometric Ratio of the Reactants. *ACS Nano* **2016**, *10*, 4228-4235.

83. Nakaya, M.; Shikishima, M.; Shibuta, M.; Hirata, N.; Eguchi, T.; Nakajima, A., Molecular-Scale and Wide-Energy-Range Tunneling Spectroscopy on Self-Assembled Monolayers of Alkanethiol Molecules. *ACS Nano* **2012**, *6*, 8728-8734.

84. Batra, A.; Kladnik, G.; Gorjizadeh, N.; Meisner, J.; Steigerwald, M.; Nuckolls, C.; Quek, S. Y.; Cvetko, D.; Morgante, A.; Venkataraman, L., Trimethyltin-Mediated Covalent Gold–Carbon Bond Formation. *J. Am. Chem. Soc.* **2014**, *136*, 12556-12559.

85. DeVries, G. A.; Talley, F. R.; Carney, R. P.; Stellacci, F., Thermodynamic Study of the Reactivity of the Two Topological Point Defects Present in Mixed Self-Assembled Monolayers on Gold Nanoparticles. *Adv. Mater.* **2008**, *20*, 4243-4247.

86. Sasaki, K.; Naohara, H.; Choi, Y.; Cai, Y.; Chen, W.-F.; Liu, P.; Adzic, R. R., Highly Stable Pt Monolayer on Pdau Nanoparticle Electrocatalysts for the Oxygen Reduction Reaction. *Nature Commun.* **2012**, *3*, 1115.

87. Guirado-López, R.; Montejano-Carrizales, J., Orbital Magnetism and Magnetic Anisotropy Energy of Co Nanoparticles: Role of Polytetrahedral Packing, Polycrystallinity, and Internal Defects. *Phys. Rev. B* **2007**, *75*, 184435.

88. Villarreal, E.; Li, G. G.; Zhang, Q.; Fu, X.; Wang, H., Nanoscale Surface Curvature Effects on Ligand–Nanoparticle Interactions: A Plasmon-Enhanced Spectroscopic Study of Thiolated Ligand Adsorption, Desorption, and Exchange on Gold Nanoparticles. *Nano Lett.* **2017**, *17*, 4443-4452.

89. Frens, G., Controlled Nucleation for the Regulation of the Particle Size in Monodisperse Gold Suspensions. *Nature* **1973**, *241*, 20-22.

90. Sun, Y.; Xia, Y., Shape-Controlled Synthesis of Gold and Silver Nanoparticles. *Science* **2002**, *298*, 2176-2179.

91. Sau, T. K.; Murphy, C. J., Room Temperature, High-Yield Synthesis of Multiple Shapes of Gold Nanoparticles in Aqueous Solution. *J. Am. Chem. Soc.* **2004**, *126*, 8648-8649.

92. Wang, Y.-C.; Engelhard, M. H.; Baer, D. R.; Castner, D. G., Quantifying the Impact of Nanoparticle Coatings and Nonuniformities on Xps Analysis: Gold/Silver Core–Shell Nanoparticles. *Anal. Chem.* **2016**, *88*, 3917-3925.

93. Brown, M. A.; Beloqui Redondo, A.; Sterrer, M.; Winter, B.; Pacchioni, G.; Abbas, Z.; van Bokhoven, J. A., Measure of Surface Potential at the Aqueous–Oxide Nanoparticle Interface by Xps from a Liquid Microjet. *Nano Lett.* **2013**, *13*, 5403-5407.

94. Jürgensen, A.; Heutz, N.; Raschke, H.; Merz, K.; Hergenröder, R., Behavior of Supported Palladium Oxide Nanoparticles under Reaction Conditions, Studied with near Ambient Pressure Xps. *Anal. Chem.* **2015**, *87*, 7848-7856.

95. Park, J.-W.; Shumaker-Parry, J. S., Structural Study of Citrate Layers on Gold Nanoparticles: Role of Intermolecular Interactions in Stabilizing Nanoparticles. *J. Am. Chem. Soc.* **2014**, *136*, 1907-1921.

96. Park, J.-W.; Shumaker-Parry, J. S., Strong Resistance of Citrate Anions on Metal Nanoparticles to Desorption under Thiol Functionalization. *ACS Nano* **2015**, *9*, 1665-1682.

97. Weisbecker, C. S.; Merritt, M. V.; Whitesides, G. M., Molecular Self-Assembly of Aliphatic Thiols on Gold Colloids. *Langmuir* **1996**, *12*, 3763-3772.

98. Zhang, S.; Leem, G.; Srisombat, L.-o.; Lee, T. R., Rationally Designed Ligands That Inhibit the Aggregation of Large Gold Nanoparticles in Solution. *J. Am. Chem. Soc.* **2008**, *130*, 113-120.

99. Wang, M.; Zhang, Z.; He, J., A Sers Study on the Assembly Behavior of Gold Nanoparticles at the Oil/Water Interface. *Langmuir* **2015**, *31*, 12911-12919.

100. DeVetter, B. M.; Mukherjee, P.; Murphy, C. J.; Bhargava, R., Measuring Binding Kinetics of Aromatic Thiolated Molecules with Nanoparticles Via Surface-Enhanced Raman Spectroscopy. *Nanoscale* **2015**, *7*, 8766-8775.

101. Alkilany, A. M.; Abulateefeh, S. R.; Mills, K. K.; Bani Yaseen, A. I.; Hamaly, M. A.; Alkhatib, H. S.; Aiedeh, K. M.; Stone, J. W., Colloidal Stability of Citrate and Mercaptoacetic Acid Capped Gold Nanoparticles Upon Lyophilization: Effect of Capping Ligand Attachment and Type of Cryoprotectants. *Langmuir* **2014**, *30*, 13799-13808.

102. Dinkel, R.; Braunschweig, B.; Peukert, W., Fast and Slow Ligand Exchange at the Surface of Colloidal Gold Nanoparticles. *J. Phys. Chem. C* **2016**, *120*, 1673-1682.

103. Ravi, V.; Binz, J. M.; Rioux, R. M., Thermodynamic Profiles at the Solvated Inorganic–Organic Interface: The Case of Gold–Thiolate Monolayers. *Nano Lett.* **2013**, *13*, 4442-4448.

104. Ojea-Jiménez, I.; Puntes, V., Instability of Cationic Gold Nanoparticle Bioconjugates: The Role of Citrate Ions. *J. Am. Chem. Soc.* **2009**, *131*, 13320-13327.

105. López-Lorente, Á. I.; Soriano, M. L.; Valcárcel, M., Analysis of Citrate-Capped Gold and Silver Nanoparticles by Thiol Ligand Exchange Capillary Electrophoresis. *Microchim. Acta* **2014**, *181*, 1789-1796.

106. Chegel, V.; Rachkov, O.; Lopatynskyi, A.; Ishihara, S.; Yanchuk, I.; Nemoto, Y.; Hill, J. P.; Ariga, K., Gold Nanoparticles Aggregation: Drastic Effect of Cooperative Functionalities in a Single Molecular Conjugate. *J. Phys. Chem. C* **2012**, *116*, 2683-2690.

107. Newman, J. D. S.; MacCrehan, W. A., The Effect of Aniline Concentration in the Ligand Exchange Reaction with Citrate-Stabilized Gold Nanoparticles. *Langmuir* **2009**, *25*, 8993-8998.

108. Lin, S.-Y.; Tsai, Y.-T.; Chen, C.-C.; Lin, C.-M.; Chen, C.-h., Two-Step Functionalization of Neutral and Positively Charged Thiols onto Citrate-Stabilized Au Nanoparticles. *J. Phys. Chem. B* **2004**, *108*, 2134-2139.

109. Perera, G. S.; Gadogbe, M.; Alahakoon, S. H.; Zhou, Y.; Zou, S.; Perez, F.; Zhang, D., Ion Pairing as the Main Pathway for Reducing Electrostatic Repulsion among Organothiolate Self-Assembled on Gold Nanoparticles in Water. *J. Phys. Chem. C* **2016**, *120*, 19878-19884.

110. Talley, C. E.; Jackson, J. B.; Oubre, C.; Grady, N. K.; Hollars, C. W.; Lane, S. M.; Huser, T. R.; Nordlander, P.; Halas, N. J., Surface-Enhanced Raman Scattering from Individual Au Nanoparticles and Nanoparticle Dimer Substrates. *Nano Lett.* **2005**, *5*, 1569-1574.

111. Barhoumi, A.; Zhang, D.; Tam, F.; Halas, N. J., Surface-Enhanced Raman Spectroscopy of DNA. *J. Am. Chem. Soc.* **2008**, *130*, 5523-5529.

112. Barhoumi, A.; Zhang, D.; Halas, N. J., Correlation of Molecular Orientation and Packing Density in a Dsdna Self-Assembled Monolayer Observable with Surface-Enhanced Raman Spectroscopy. *J. Am. Chem. Soc.* **2008**, *130*, 14040-14041.

113. Wustholz, K. L.; Henry, A.-I.; McMahon, J. M.; Freeman, R. G.; Valley, N.; Piotti, M. E.; Natan, M. J.; Schatz, G. C.; Duyne, R. P. V., Structure−Activity Relationships in Gold Nanoparticle Dimers and Trimers for Surface-Enhanced Raman Spectroscopy. *J. Am. Chem. Soc.* **2010**, *132*, 10903-10910.

114. Kneipp, K.; Kneipp, H.; Kneipp, J., Surface-Enhanced Raman Scattering in Local Optical Fields of Silver and Gold Nanoaggregatesfrom Single-Molecule Raman Spectroscopy to Ultrasensitive Probing in Live Cells. *Acc. Chem. Res.* **2006**, *39*, 443-450.

115. Siriwardana, K.; LaCour, A.; Zhang, D., Critical Sequence Dependence in Multicomponent Ligand Binding to Gold Nanoparticles. *J. Phys. Chem. C* **2016**, *120*, 6900-6905.

116. Siriwardana, K.; Gadogbe, M.; Ansar, S. M.; Vasquez, E. S.; Collier, W. E.; Zou, S.; Walters, K. B.; Zhang, D., Ligand Adsorption and Exchange on Pegylated Gold Nanoparticles. *J. Phys. Chem. C* **2014**, *118*, 11111-11119.

117. Hore, M. J. A.; Ye, X.; Ford, J.; Gao, Y.; Fei, J.; Wu, Q.; Rowan, S. J.; Composto, R. J.; Murray, C. B.; Hammouda, B., Probing the Structure, Composition, and Spatial Distribution of Ligands on Gold Nanorods. *Nano Lett.* **2015**, *15*, 5730-5738.

118. Zhao, W.; Chiuman, W.; Lam, J. C. F.; McManus, S. A.; Chen, W.; Cui, Y.; Pelton, R.; Brook, M. A.; Li, Y., DNA Aptamer Folding on Gold Nanoparticles: From Colloid Chemistry to Biosensors. *J. Am. Chem. Soc.* **2008**, *130*, 3610-3618.

119. Hurst, S. J.; Lytton-Jean, A. K. R.; Mirkin, C. A., Maximizing DNA Loading on a Range of Gold Nanoparticle Sizes. *Anal. Chem.* **2006**, *78*, 8313-8318.

120. Jana, N. R.; Gearheart, L.; Murphy, C. J., Evidence for Seed-Mediated Nucleation in the Chemical Reduction of Gold Salts to Gold Nanoparticles. *Chem. Mater.* **2001**, *13*, 2313-2322.

121. Ansar, S. M.; Li, X.; Zou, S.; Zhang, D., Quantitative Comparison of Raman Activities, Sers Activities, and Sers Enhancement Factors of Organothiols: Implication to Chemical Enhancement. *J. Phys. Chem. Lett.* **2012**, *3*, 560-565.

122. Li, Z.; Kozbial, A.; Nioradze, N.; Parobek, D.; Shenoy, G. J.; Salim, M.; Amemiya, S.; Li, L.; Liu, H., Water Protects Graphitic Surface from Airborne Hydrocarbon Contamination. *ACS Nano* **2015**, *10*, 349-359.

123. Li, Z., et al., Effect of Airborne Contaminants on the Wettability of Supported Graphene and Graphite. *Nature Mater.* **2013**, *12*, 925-931.

124. Wagner, C. D., Sensitivity Factors for Xps Analysis of Surface Atoms. *J. Electron Spec. Rel. Phen.* **1983**, *32*, 99-102.

125. Wagner, C.; Davis, L.; Zeller, M.; Taylor, J.; Raymond, R.; Gale, L., Empirical Atomic Sensitivity Factors for Quantitative Analysis by Electron Spectroscopy for Chemical Analysis. *Surf. Interface Anal.* **1981**, *3*, 211-225.

126. Perera, G. S.; Nettles, C. B.; Zhou, Y.; Zou, S.; Hollis, T. K.; Zhang, D., Direct Observation of Ion Pairing at the Liquid/Solid Interfaces by Surface Enhanced Raman Spectroscopy. *Langmuir* **2015**, *31*, 8998-9005.

127. Perera, G. S.; Yang, G.; Nettles, C. B.; Perez, F.; Hollis, T. K.; Zhang, D., Counterion Effects on Electrolyte Interactions with Gold Nanoparticles. *J. Phys. Chem. C* **2016**, *120*, 23604-23612.

128. Ansar, S. M.; Gadogbe, M.; Siriwardana, K.; Howe, J. Y.; Dogel, S.; Hosseinkhannazer, H.; Collier, W. E.; Rodriguez, J.; Zou, S.; Zhang, D., Dispersion Stability, Ligand Structure and Conformation, and Sers Activities of 1-Alkanethiol Functionalized Gold and Silver Nanoparticles. *J. Phys. Chem. C* **2014**, *118*, 24925-24934.

129. Ansar, S. M.; Perera, G. S.; Gomez, P.; Salomon, G.; Vasquez, E. S.; Chu, I. W.; Zou, S.; Pittman, C. U.; Walters, K. B.; Zhang, D., Mechanistic Study of Continuous Reactive Aromatic Organothiol Adsorption onto Silver Nanoparticles. *J. Phys. Chem. C* **2013**, *117*, 27146-27154.

130. Vangala, K.; Siriwardana, K.; Vasquez, E. S.; Xin, Y.; Pittman, C. U.; Walters, K. B.; Zhang, D., Simultaneous and Sequential Protein and Organothiol Interactions with Gold Nanoparticles. *J. Phys. Chem. C* **2013**, *117*, 1366-1374.

131. Ameer, F. S.; Pittman Jr, C. U.; Zhang, D., Quantification of Resonance Raman Enhancement Factors for Rhodamine 6g (R6g) in Water and on Gold and Silver Nanoparticles: Implications for Single-Molecule R6g Sers. *J. Phys. Chem. C* **2013**, *117*, 27096-27104.

132. Ke, S.-H.; Yang, W.; Baranger, H. U., Quantum-Interference-Controlled Molecular Electronics. *Nano Lett.* **2008**, *8*, 3257-3261.

133. Dondapati, S. K.; Sau, T. K.; Hrelescu, C.; Klar, T. A.; Stefani, F. D.; Feldmann, J., Label-Free Biosensing Based on Single Gold Nanostars as Plasmonic Transducers. *ACS Nano* **2010**, *4*, 6318-6322.

134. Wustholz, K. L.; Henry, A.-I.; McMahon, J. M.; Freeman, R. G.; Valley, N.; Piotti, M. E.; Natan, M. J.; Schatz, G. C.; Duyne, R. P. V., Structure− Activity Relationships in Gold Nanoparticle Dimers and Trimers for Surface-Enhanced Raman Spectroscopy. *J. Am. Chem. Soc.* **2010**, *132*, 10903-10910.

135. Zielasek, V.; Jürgens, B.; Schulz, C.; Biener, J.; Biener, M. M.; Hamza, A. V.; Bäumer, M., Gold Catalysts: Nanoporous Gold Foams. *Angew. Chem. Int. Ed.* **2006**, *45*, 8241-8244.

136. Ansar, S. M.; Perera, G. S.; Jiang, D.; Holler, R. A.; Zhang, D., Organothiols Self-Assembled onto Gold: Evidence for Deprotonation of the Sulfur-Bound Hydrogen and Charge Transfer from Thiolate. *J. Phys. Chem. C* **2013**, *117*, 8793-8798.

137. DuChene, J. S.; Niu, W.; Abendroth, J. M.; Sun, Q.; Zhao, W.; Huo, F.; Wei, W. D., Halide Anions as Shape-Directing Agents for Obtaining High-Quality Anisotropic Gold Nanostructures. *Chem. Mater.* **2012**, *25*, 1392-1399.

138. Personick, M. L.; Langille, M. R.; Zhang, J.; Mirkin, C. A., Shape Control of Gold Nanoparticles by Silver Underpotential Deposition. *Nano Lett.* **2011**, *11*, 3394-3398.

139. Liu; Guyot-Sionnest, P., Mechanism of Silver(I)-Assisted Growth of Gold Nanorods and Bipyramids. *J. Phys. Chem. B* **2005**, *109*, 22192-22200.

140. Murphy, C. J.; Thompson, L. B.; Chernak, D. J.; Yang, J. A.; Sivapalan, S. T.; Boulos, S. P.; Huang, J.; Alkilany, A. M.; Sisco, P. N., Gold Nanorod Crystal Growth: From Seed-Mediated Synthesis to Nanoscale Sculpting. *Curr. Opin. Colloid .Interface Sci.* **2011**, *16*, 128-134.

141. Wu, Z., Anti-Galvanic Reduction of Thiolate-Protected Gold and Silver Nanoparticles. *Angew. Chem. Int. Ed.* **2012**, *51*, 2934-2938.

142. Kang, H.; Kim, B.-G.; Na, H. B.; Hwang, S., Anti-Galvanic Reduction of Silver Ion on Gold and Its Role in Anisotropic Growth of Gold Nanomaterials. *J. Phys. Chem. C* **2015**, *119*, 25974-25982.

143. Liu, X.; Astruc, D., From Galvanic to Anti-Galvanic Synthesis of Bimetallic Nanoparticles and Applications in Catalysis, Sensing, and Materials Science. *Adv. Mater.* **2017**, *29*, 1605305

144. Sun, J.; Wu, H.; Jin, Y., Synthesis of Thiolated Ag/Au Bimetallic Nanoclusters Exhibiting an Anti-Galvanic Reduction Mechanism and Composition-Dependent Fluorescence. *Nanoscale* **2014**, *6*, 5449-5457.

145. Vericat, C.; Vela, M. E.; Benitez, G.; Carro, P.; Salvarezza, R. C., Self-Assembled Monolayers of Thiols and Dithiols on Gold: New Challenges for a Well-Known System. *Chem. Soc. Rev.* **2010**, *39*, 1805-1834.

146. Grönbeck, H.; Curioni, A.; Andreoni, W., Thiols and Disulfides on the Au (111) Surface: The Head Group− Gold Interaction. *J. Am. Chem. Soc.* **2000**, *122*, 3839-3842.

147. Laibinis, P. E.; Whitesides, G. M.; Allara, D. L.; Tao, Y. T.; Parikh, A. N.; Nuzzo, R. G., Comparison of the Structures and Wetting Properties of Self-Assembled Monolayers of N-Alkanethiols on the Coinage Metal Surfaces, Copper, Silver, and Gold. *J. Am. Chem. Soc.* **1991**, *113*, 7152-7167.

148. Volkert, A. A.; Subramaniam, V.; Haes, A. J., Implications of Citrate Concentration During the Seeded Growth Synthesis of Gold Nanoparticles. *Chem. Commun.* **2011**, *47*, 478-480.

149. Siriwardana, K.; Suwandaratne, N.; Perera, G. S.; Collier, W. E.; Perez, F.; Zhang, D., Contradictory Dual Effects: Organothiols Can Induce Both Silver Nanoparticle Disintegration and Formation under Ambient Conditions. *J. Phys. Chem. C* **2015**, *119*, 20975-20984.

150. Xu, S.; Ji, X.; Xu, W.; Li, X.; Wang, L.; Bai, Y.; Zhao, B.; Ozaki, Y., Immunoassay Using Probe-Labelling Immunogold Nanoparticles with Silver Staining Enhancement Via Surface-Enhanced Raman Scattering. *Analyst* **2004**, *129*, 63-68.

151. Cao, Y. C.; Jin, R.; Nam, J.-M.; Thaxton, C. S.; Mirkin, C. A., Raman Dye-Labeled Nanoparticle Probes for Proteins. *J. Am. Chem. Soc.* **2003**, *125*, 14676-14677.

152. Qin, X.; Liu, L.; Xu, A.; Wang, L.; Tan, Y.; Chen, C.; Xie, Q., Ultrasensitive Immunoassay of Proteins Based on Gold Label/Silver Staining, Galvanic Replacement Reaction Enlargement, and in Situ Microliter-Droplet Anodic Stripping Voltammetry. *J. Phys. Chem. C* **2016**, *120*, 2855-2865.

153. Min, I.-H.; Choi, L.; Ahn, K.-S.; Kim, B. K.; Lee, B. Y.; Kim, K. S.; Choi, H. N.; Lee, W.-Y., Electrochemical Determination of Carbohydrate-Binding Proteins Using Carbohydrate-Stabilized Gold Nanoparticles and Silver Enhancement. *Biosens. Bioelec.* **2010**, *26*, 1326-1331.

154. Lin, L.; Liu, Y.; Tang, L.; Li, J., Electrochemical DNA Sensor by the Assembly of Graphene and DNA-Conjugated Gold Nanoparticles with Silver Enhancement Strategy. *Analyst* **2011**, *136*, 4732-4737.

155. Cao, Y. C.; Jin, R.; Mirkin, C. A., Nanoparticles with Raman Spectroscopic Fingerprints for DNA and Rna Detection. *Science* **2002**, *297*, 1536-1540.

156. Chung, E.; Gao, R.; Ko, J.; Choi, N.; Lim, D. W.; Lee, E. K.; Chang, S.-I.; Choo, J., Trace Analysis of Mercury(Ii) Ions Using Aptamer-Modified Au/Ag Core-Shell Nanoparticles and Sers Spectroscopy in a Microdroplet Channel. *Lab Chip* **2013**, *13*, 260-266.

157. Su, X.; Li, S. F. Y.; O'Shea, S. J., Au Nanoparticle- and Silver-Enhancement Reaction-Amplified Microgravimetric Biosensor. *Chem. Commun.* **2001**, 755-756.

158. Perera, G. S.; Athukorale, S. A.; Perez, F.; Pittman, C. U.; Zhang, D., Facile Displacement of Citrate Residues from Gold Nanoparticle Surfaces. *Journal of Colloid and Interface Science* **2018**, *511*, 335-343.

159. King, D. E., Oxidation of Gold by Ultraviolet Light and Ozone at 25 C. *J. Vac. Sci.Tech. A* **1995**, *13*, 1247-1253.

160. Al-Ajlony, A.-M. B.; Kanjilal, A.; Harilal, S. S.; Hassanein, A., Carbon Contamination and Oxidation of Au Surfaces under Extreme Ultraviolet Radiation: An X-Ray Photoelectron Spectroscopy Study. *J. Vac. Sci. Tech. B* **2012**, *30*, 041603.

161. Bantz, K. C.; Nelson, H. D.; Haynes, C. L., Plasmon-Enabled Study of Self-Assembled Alkanethiol Ordering on Roughened Ag Substrates. *J. Phys. Chem. C* **2012**, *116*, 3585-3593.

162. Rycenga, M.; McLellan, J. M.; Xia, Y., A Sers Study of the Molecular Structure of Alkanethiol Monolayers on Ag Nanocubes in the Presence of Aqueous Glucose. *Chem. Phys. Lett.* **2009**, *463*, 166-171.

163. Pérez-Juste, J.; Pastoriza-Santos, I.; Liz-Marzán, L. M.; Mulvaney, P., Gold Nanorods: Synthesis, Characterization and Applications. *Coord. Chem. Rev.* **2005**, *249*, 1870-1901.

164. Sau, T. K.; Murphy, C. J., Seeded High Yield Synthesis of Short Au Nanorods in Aqueous Solution. *Langmuir* **2004**, *20*, 6414-6420.

165. Hubert, F.; Testard, F.; Spalla, O., Cetyltrimethylammonium Bromide Silver Bromide Complex as the Capping Agent of Gold Nanorods. *Langmuir* **2008**, *24*, 9219-9222.

166. Jana, N. R.; Gearheart, L.; Murphy, C. J., Seed-Mediated Growth Approach for Shape-Controlled Synthesis of Spheroidal and Rod-Like Gold Nanoparticles Using a Surfactant Template. *Adv. Mater.* **2001**, *13*, 1389.

167. Gaarenstroom, S. W.; Winograd, N., Initial and Final State Effects in the Esca Spectra of Cadmium and Silver Oxides. *J. Chem. Phys.* **1977**, *67*, 3500-3506.

168. Kaushik, V. K., Xps Core Level Spectra and Auger Parameters for Some Silver Compounds. *J. Electron Spectrosc. Relat. Phenom.* **1991**, *56*, 273-277.

169. Ferraria, A. M.; Carapeto, A. P.; Botelho do Rego, A. M., X-Ray Photoelectron Spectroscopy: Silver Salts Revisited. *Vacuum* **2012**, *86*, 1988-1991.

170. Kaushik, V. K., Xps Core Level Spectra and Auger Parameters for Some Silver Compounds. *J. Electron Spectrosc. Relat. Phenom.***1991**, *56*, 273-277.

171. Alex, S.; Tiwari, A., Functionalized Gold Nanoparticles: Synthesis, Properties and Applications—a Review. *J. Nanosci. Nanotech.* **2015**, *15*, 1869-1894.

172. Zhou, W.; Gao, X.; Liu, D.; Chen, X., Gold Nanoparticles for in Vitro Diagnostics. *Chem. Rev.* **2015**, *115*, 10575-10636.

173. Lombardi, J. R.; Birke, R. L., A Unified View of Surface-Enhanced Raman Scattering. *Acc. Chem. Res.* **2009**, *42*, 734-742.

174. Daniel, M.-C.; Astruc, D., Gold Nanoparticles: Assembly, Supramolecular Chemistry, Quantum-Size-Related Properties, and Applications toward Biology, Catalysis, and Nanotechnology. *Chem. Rev.* **2004**, *104*, 293-346.

175. Pensa, E.; Cortés, E.; Corthey, G.; Carro, P.; Vericat, C.; Fonticelli, M. H.; Benítez, G.; Rubert, A. A.; Salvarezza, R. C., The Chemistry of the Sulfur–Gold Interface: In Search of a Unified Model. *Acc. Chem. Res.* **2012**, *45*, 1183-1192.

176. Johnson, B. N.; Mutharasan, R., Regeneration of Gold Surfaces Covered by Adsorbed Thiols and Proteins Using Liquid-Phase Hydrogen Peroxide-Mediated Uv-Photooxidation. *J. Phys. Chem. C* **2013**, *117*, 1335-1341.

177. Kim, D. J.; Pitchimani, R.; Snow, D. E.; Hope-Weeks, L. J., A Simple Method for the Removal of Thiols on Gold Surfaces Using an Nh4oh–H2o2–H2o Solution. *Scanning* **2008**, *30*, 118-122.

178. Kassam, A.; Bremner, G.; Clark, B.; Ulibarri, G.; Lennox, R. B., Place Exchange Reactions of Alkyl Thiols on Gold Nanoparticles. *J. Am. Chem. Soc.* **2006**, *128*, 3476-3477.

179. Montalti, M.; Prodi, L.; Zaccheroni, N.; Baxter, R.; Teobaldi, G.; Zerbetto, F., Kinetics of Place-Exchange Reactions of Thiols on Gold Nanoparticles. *Langmuir* **2003**, *19*, 5172-5174.

180. Hostetler, M. J.; Templeton, A. C.; Murray, R. W., Dynamics of Place-Exchange Reactions on Monolayer-Protected Gold Cluster Molecules. *Langmuir* **1999**, *15*, 3782-3789.

181. Ionita, P.; Caragheorgheopol, A.; Gilbert, B. C.; Chechik, V., Epr Study of a Place-Exchange Reaction on Au Nanoparticles: Two Branches of a Disulfide Molecule Do Not Adsorb Adjacent to Each Other. *J. Am. Chem. Soc.* **2002**, *124*, 9048-9049.

182. Siriwardana, K.; La Cour, A.; Zhang, D., Critical Sequence Dependence in Multicomponent Ligand Binding to Gold Nanoparticles. *J. Phys. Chem. C* **2016**, *120*, 6900-6905.

183. Tang, Q.-L.; Duan, X.-X.; Zhang, T.-T.; Fan, X.; Zhang, X., Comparative Theoretical Study of the Chemistry of Hydrogen Sulfide on Cu(100) and Au(100): Implications for Sulfur Tolerance of Water Gas Shift Nanocatalysts. *The J. Phys. Chem. C* **2016**, *120*, 25351-25360.

184. Kuang, X.; Wang, X.; Liu, G., A Density Functional Theory Study on the H2s Molecule Adsorption onto Small Gold Clusters. *Applied Surface Science* **2011**, *257*, 6546-6553.

185. Hamilton, I. C.; Woods, R., An Investigation of the Deposition and Reactions of Sulphur on Gold Electrodes. *Journal of Applied Electrochemistry* **1983**, *13*, 783-794.

186. Tao, Y.-T.; Pandian, K.; Lee, W.-C., Hydrogen Sulfide-Induced Desorption/Reorganization of Self-Assembled Monolayers of Alkanethiol and Its Derivatives. *J. Am. Chem. Soc.***2000**, *122*, 7072-7079.

187. Lustemberg, P. G.; Vericat, C.; Benitez, G. A.; Vela, M. E.; Tognalli, N.; Fainstein, A.; Martiarena, M. L.; Salvarezza, R. C., Spontaneously Formed Sulfur Adlayers on Gold in Electrolyte Solutions: Adsorbed Sulfur or Gold Sulfide? *The J. Phys. Chem. C* **2008**, *112*, 11394-11402.

188. Hughes, M. N.; Centelles, M. N.; Moore, K. P., Making and Working with Hydrogen Sulfide: The Chemistry and Generation of Hydrogen Sulfide in Vitro and Its Measurement in Vivo: A Review. *Free Rad. Bio. Med.* **2009**, *47*, 1346-1353.

189. Ansar, S. M.; Ameer, F. S.; Hu, W.; Zou, S.; Pittman, C. U.; Zhang, D., Removal of Molecular Adsorbates on Gold Nanoparticles Using Sodium Borohydride in Water. *Nano Lett.* **2013**, *13*, 1226-1229.

190. Athukorale, S.; Perera, G. S.; Gadogbe, M.; Perez, F.; Zhang, D., Reactive Ag+ Adsorption onto Gold. *The J. Phys. Chem. C* **2017**.

191. Gadogbe, M.; Zhou, Y.; Alahakoon, S. H.; Perera, G. S.; Zou, S.; Pittman, C. U.; Zhang, D., Structures and Conformations of Alkanedithiols on Gold and Silver Nanoparticles in Water. *J. Phys. Chem. C* **2015**, *119*, 18414-18421.

192. Perera, G. S.; Yang, G.; Nettles, C. B.; Perez, F.; Hollis, T. K.; Zhang, D., Counterion Effects on Electrolyte Interactions with Gold Nanoparticles. *The J. Phys. Chem. C* **2016**, *120*, 23604-23612

193. Perera, G. S.; Nettles, C. B., 2nd; Hollis, T. K.; Zhang, D.; Zhou, Y.; Zou, S., Direct Observation of Ion Pairing at the Liquid/Solid Interfaces by Surface Enhanced Raman Spectroscopy. *Langmuir* **2015**, *31*, 8998-9005.

194. Mirza, J.; Smith, S. R.; Baron, J. Y.; Choi, Y.; Lipkowski, J., A Sers Characterization of the Stability of Polythionates at the Gold–Electrolyte Interface. *Surf. Sci.* **2015**, *631*, 196-206.

195. Gadgil, B.; Damlin, P.; Viinikanoja, A.; Heinonen, M.; Kvarnstrom, C., One-Pot Synthesis of an Au/Au2s Viologen Hybrid Nanocomposite for Efficient Catalytic Applications. *J. Mater. Chem. A* **2015**, *3*, 9731-9737.

196. Parker, G. K.; Watling, K. M.; Hope, G. A.; Woods, R., A Sers Spectroelectrochemical Investigation of the Interaction of Sulfide Species with Gold Surfaces. *Coll. Surf. A: Physicochem. Eng. Asp.* **2008**, *318*, 151-159.

197. Dubois, P.; Lelieur, J. P.; Lepoutre, G., Identification and Characterization of Ammonium Polysulfides in Solution in Liquid Ammonia. *Inorg. Chem.* **1988**, *27*, 1883-1890.

198. Kalampounias, A. G.; Andrikopoulos, K. S.; Yannopoulos, S. N., Probing the Sulfur Polymerization Transition in Situ with Raman Spectroscopy. *J. Chem. Phys.* **2003**, *118*, 8460-8467.

199. Trofimov, B. A.; Sinegovskaya, L. M.; Gusarova, N. K., Vibrations of the S–S Bond in Elemental Sulfur and Organic Polysulfides: A Structural Guide. *J. Sulphur Chem.* **2009**, *30*, 518-554.

200. Ansar, S. M.; Li, X.; Zou, S.; Zhang, D., Quantitative Comparison of Raman Activities, Sers Activities, and Sers Enhancement Factors of Organothiols: Implication to Chemical Enhancement. *J. Phys. Chem. Lett.* **2012**, *3*, 560-565.

201. Pagliai, M.; Caporali, S.; Muniz-Miranda, M.; Pratesi, G.; Schettino, V., Sers, Xps, and Dft Study of Adenine Adsorption on Silver and Gold Surfaces. *J. Phys. Chem. Lett.* **2012**, *3*, 242-245.

202. Willets, K. A., Super-Resolution Imaging of Sers Hot Spots. *Chem. Soc. Rev.* **2014**, *43*, 3854-3864.

203. Qin, L.; Zou, S.; Xue, C.; Atkinson, A.; Schatz, G. C.; Mirkin, C. A., Designing, Fabricating, and Imaging Raman Hot Spots. *Proc. Natl. Acad. Sci. U.S.A.* **2006**, *103*, 13300-13303.

204. Campion, A.; Kambhampati, P., Surface-Enhanced Raman Scattering. *Chem. Soc. Rev.* **1998**, *27*, 241-250.

205. Camden, J. P.; Dieringer, J. A.; Wang, Y.; Masiello, D. J.; Marks, L. D.; Schatz, G. C.; Van Duyne, R. P., Probing the Structure of Single-Molecule Surface-Enhanced Raman Scattering Hot Spots. *J. Am. Chem. Soc.* **2008**, *130*, 12616-12617.

206. Suwandaratne, N.; Hu, J.; Siriwardana, K.; Gadogbe, M.; Zhang, D., Evaluation of Thiol Raman Activities and Pka Values Using Internally Referenced Raman-Based Ph Titration. *Anal. Chem. (Washington, DC, U. S.)* **2016**, *88*, 3624-3631.

207. Armstrong, D. A.; Sun, Q.; Tripathi, G. N. R.; Schuler, R. H.; McKinnon, D., Spectra, Ionization Constants, and Rates of Oxidation of 1,4-Dimercaptobenzene and Properties of the P-Mercaptophenylthiyl and P-Benzodithiyl Anion Radicals. *J. Phys. Chem. C* **1993**, *97*, 5611-5617.

208. Krekel, F.; Samland, A. K.; Macheroux, P.; Amrhein, N.; Evans, J. N. S., Determination of the Pka Value of C115 in Mura (Udp-N-Acetylglucosamine Enolpyruvyltransferase) from Enterobacter Cloacae. *Biochemistry* **2000**, *39*, 12671-12677.

209. Connett, P. H.; Wetterhahn, K. E., Reaction of Chromium(Vi) with Thiols: Ph Dependence of Chromium(Vi) Thio Ester Formation. *J. Am. Chem. Soc.***1986**, *108*, 1842-1847.
210. Jencks, W. P.; Salvesen, K., Equilibrium Deuterium Isotope Effects on the Ionization of Thiol Acids. *J. Am. Chem. Soc.***1971**, *93*, 4433-4436.

APPENDIX A

COPYRIGHT PERMISION

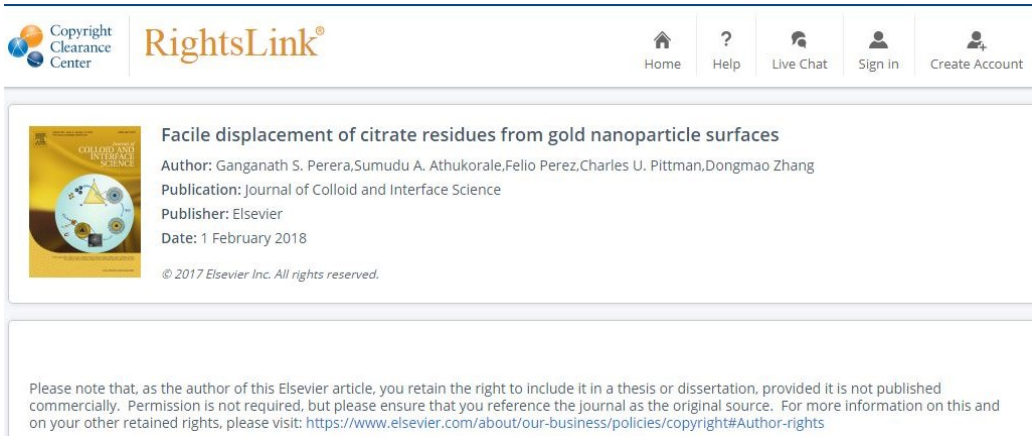

Figure A.1 Copyright permission form for Chapter II

Notes: The content covered in Chapter II contains material previously published by the Elsevier in the Journal of Colloid and Interface Science. Content is referenced as Perera, G. S.; Athukorale, S. A.; Perez, F.; Pittman, C. U.; Zhang, D., Facile Displacement of Citrate Residues from Gold Nanoparticle Surfaces. *J. Colloid Interface Sci.* **2018**, *511*, 335-343.

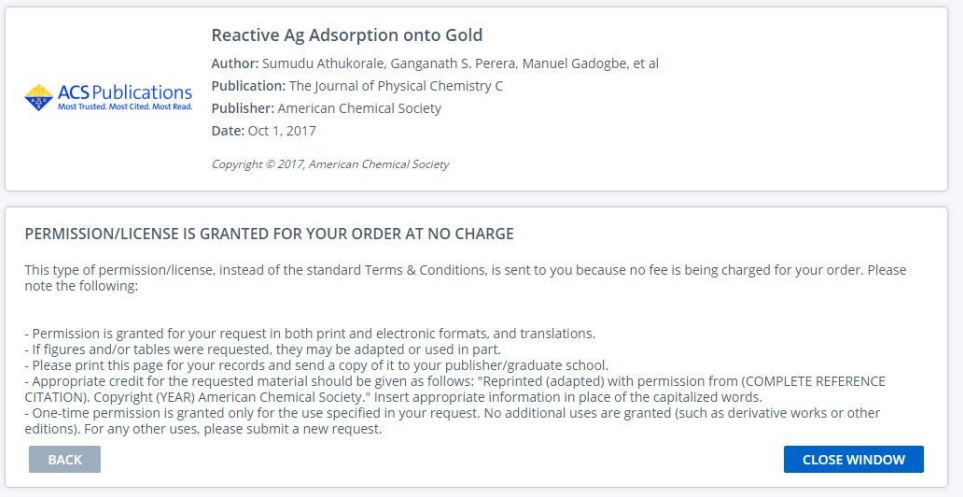

Figure A.2 Copyright permission form for Chapter III

Notes: The content covered in Chapter III contains material previously published by the American Chemical Society in The Journal of Physical Chemistry C. Content is referenced as Athukorale, S.; Perera, G. S.; Gadogbe, M.; Perez, F.; Zhang, D., Reactive Ag+ Adsorption onto Gold. *J. Phys. Chem. C* **2017**, *121*, 22487-22495.

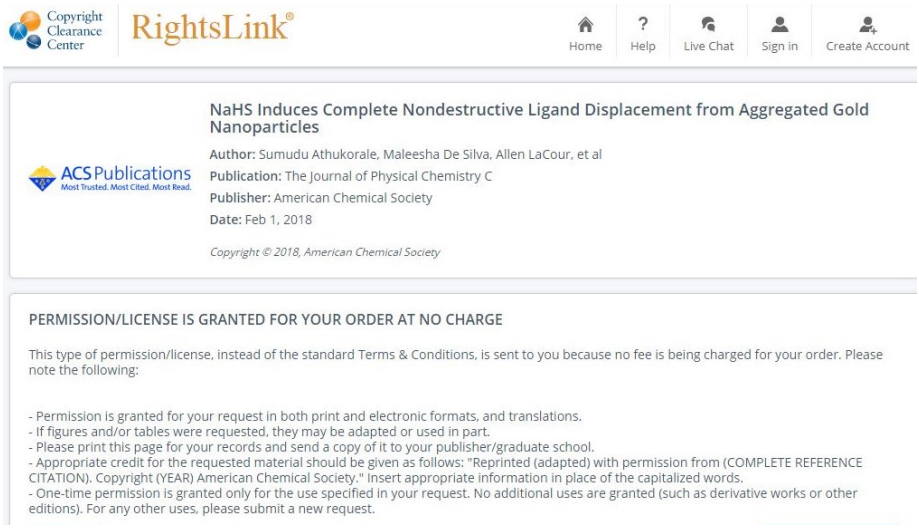

Figure A.3 Copyright permission form for Chapter IV

Notes: The content covered in Chapter IV contains material previously published by the American Chemical Society in The Journal of Physical Chemistry C. Content is referenced as Athukorale, S.; De Silva, M.; LaCour, A.; Perera, G. S.; Pittman, C. U.; Zhang, D., Nahs Induces Complete Nondestructive Ligand Displacement from Aggregated Gold Nanoparticles. *J. Phys. Chem. C* **2018**, *122*, 2137-2144.

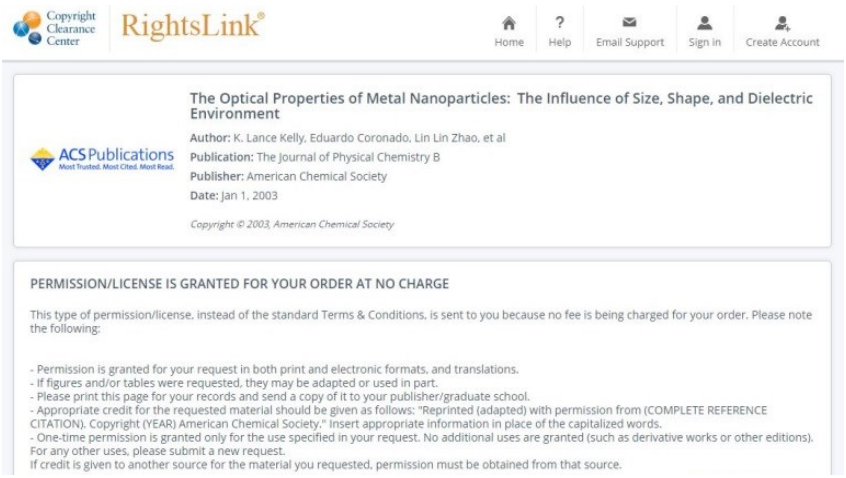

Figure A.4 Copyright permission form for Figure 1.1

Note: The Figure 1.1 is previously published by the American Chemical Society in The Journal of Physical Chemistry B. Article is referenced as Kelly, K. L.; Coronado, E.; Zhao, L. L.; Schatz, G. C. The Optical Properties of Metal Nanoparticles: The Influence of Size, Shape, and Dielectric Environment. *J. Phys. Chem. B* **2003***, 107,* 3, 668-677